Reining In the Butterfly Effect: Construction of Robust Global Mantle Flow Trajectories, Their Assessment through Dynamic Topography Histories via Object-based Image Processing Methods Derived from Meteorology and a Case Study of Southern African Topographic Uplift

Dissertation von Ayodeji Abdul-Razaq Taiwo

München 2023

Reining In the Butterfly Effect: Construction of Robust Global Mantle Flow Trajectories, Their Assessment through Dynamic Topography Histories via Object-based Image Processing Methods Derived from Meteorology and a Case Study of Southern African Topographic Uplift

Dissertation
zur Erlangung des Doktorgrades
an der Fakultät für Geowissenschaften
der Ludwig-Maximilians-Universität München

vorgelegt/eingereicht von
Ayodeji Abdul-Razaq Taiwo

aus
Lagos, Nigeria

2023

Erstgutachter/in:	Prof. Dr. Hans-Peter Bunge
Zweitgutachter/in:	Prof. Dr. George Craig
Tag der mündlichen Prüfung:	01. Feb. 2023

Contents

List of Figures

List of Tables

Zusammenfassung

In the past, fluid dynamicists obtained analytical solutions for simplified versions of the equations governing mantle flow. However, in recent times, numerical solutions of these equations as well as their graphical representation have been enabled by computational and visualization advances. These developments have led to the construction of high resolution, time-dependent models capable of simulating realistic mantle convection scenarios and creating time trajectories of mantle flow. Two main modelling approaches have been so far employed: mantle circulation models (MCMs) which simulate mantle flow forward in time starting from a randomly chosen past state of the mantle, and the adjoint method which reconstructs past mantle flow starting from an estimate of the mantle present-day state as derived from seismic tomography. In both cases, the starting (initial) conditions are not well known. On the other hand, the mantle is in a category of systems that exhibit chaotic behaviour. The implication of this behaviour is that uncertainties in the initial condition of a time-dependent mantle model grow and propagate through the entire model thus leading to the construction of incorrect mantle flow trajectories. This is referred to as the *butterfly effect*. However, geodynamicists have learned that if knowledge of the surface velocity field is available and if this information is assimilated into a mantle model, it is possible to overcome the butterfly effect and construct robust trajectories. A key geologic observation against which such trajectories can be tested is the Earth's dynamic topography that is increasingly well-mapped by geologists. There is, however, a dearth of high-quality metrics that allow one to compare dynamic topography effectively. Meteorologists have extensively studied forecast verification methods including the Taylor diagram, power ratio, scale-separation techniques and object-based verification and it is possible to adapt these metrics to dynamic topography.

In this work, I verify, using synthetic forward models of mantle flow, that velocity assimilation leads to the construction of robust, accurate mantle flow trajectories. I then compute dynamic topography responses from the constructed trajectories and I adapt a number of meteorological forecast verification tools to assess dynamic topography. Importantly, I develop and object-based, image processing metric with which dynamic topography maps can be evaluated. Finally, I apply these metrics to results from a set of state-of-the-art, recently published adjoint simulations of mantle flow. In a twin experiment setup, I use these metrics to explore model performance for a case study focused on the dynamic topography high located in southern Africa. The results of the study show that these metrics

provide a powerful way of analysing dynamic topography behaviour of global geodynamic models.

Chapter 1

Introduction

In life, one moves on from the past. In the geosciences, one has only the past to look at.
— Ayodeji Taiwo

The Earth is comprised of distinct layers, that have been formed from planetary accretion and differentiation. The outermost layer, known as the crust, has formed over millions of years (Myrs) through continuous melting and reworking of the underlying mantle. This crustal layer is rich in silica and has an average thickness of 38 km beneath continents and 7–8 km beneath oceans. The Earth's mantle, located at a depth of $\approx$ 30 - 3000 km below the surface, is composed mostly of magnesium silicates and is stronger than steel. Beneath the mantle, and extending down to the Earth's center, lies the core — the innermost layer of Earth. It is assumed to be composed primarily of iron and nickel (Jeanloz, 1990). The core is further sub-divided into a liquid outer and solid inner core. The outer core is in convective motion and is responsible for generating the Earth's magnetic field. The boundary between the outer core and mantle is known as the core-mantle boundary (CMB) (see Fowler, 2004, for a detailed description of the various layers of the inner Earth). Via a variety of geophysical observations such as the advance and retreat of glaciers (Haskell 1935; Mitrovica 1996; Cathles 1975; Kaufmann and Lambeck 2002), satellite observations of secular changes in the gravity field coupled with measurements of sea level changes (Paulson et al., 2007), the effective viscosity of the mantle has been inferred to be in the range of $10^{20} - 10^{23}$ Pa s. Such a high value may lead one to assume that the mantle is solid; this is true on short time scales, where the mantle transmits seismic shear waves. But over geologic time scales of Myrs, the mantle acts as a fluid and convects in a creeping motion in response to internal density variations. The mantle's convective motion is the cause for the large-scale horizontal movement of tectonic plates (Davies and Richards, 1992). Importantly, the stresses associated with mantle convection induce vertical motions (Pekeris, 1935) in addition to driving the horizontal component of plate movement. These vertical motions manifest themselves as a so-called dynamic topography (Hager et al., 1985) which is the vertical deflection of the Earth surface away from its isostatically compensated state. Dynamic topography differs from isostatic topography which owes majorly to

crustal density variations (see Braun, 2010, for a recent review on dynamic topography). Mantle convection takes its energy from internal, radioactive sources, secular cooling and heat supplied through the CMB from the core beneath. Heat from the core enters the mantle by thermal diffusion, so that the lowermost mantle is characterized by a thermal boundary layer. The latter can undergo gravitational (Rayleigh-Taylor) instabilities, when hot buoyant material rises from the CMB through the mantle as a so-called mantle plume (Morgan, 1971), characterized by a mushroom-shaped head. As hot plume material moves upward, the convective process is reinforced by the sinking (subduction) of cold material from the top of the mantle, comprised of oceanic plates. Rising and sinking motions together induce large convective cells in the Earth's interior, which have been imaged by seismic tomography (e.g., Ritsema et al. (2011); Simmons et al. (2007)) akin to medical tomography, but from the passage of seismic waves. Despite advances in the imaging of the Earth's interior, important uncertainties related to the compositional nature of mantle plumes and the rheology (deformation and flow under stress) of the deep Earth still exist. As such, quantitative, computational modelling of mantle flow is essential. Mantle convection lends itself to a quantitative description through the physics of hydrodynamics. In essence, one solves conservation equations for mass, momentum and energy respectively. In the simplest case, the so-called Boussinesq approximation is applied; thus, the mantle is assumed to be an incompressible Newtonian fluid, implying that all density terms except those in the buoyancy field are ignored and thus the conservation of mass breaks down to a conservation of volume. Since the mantle is of a high viscosity, the acceleration terms in the conservation of momentum can be neglected and the conservation of momentum simplifies to an instantaneous balance of buoyancy and viscous stresses.

$$\nabla \cdot (v) = 0 \tag{1.1}$$

$$\eta(\nabla^2 v) - \nabla P + \rho g = 0 \tag{1.2}$$

$$\partial_t T + v \cdot \nabla T - \kappa \nabla^2 T + H = 0 \tag{1.3}$$

subject to a set of appropriate boundary conditions. In the above equations κ, ρ, η, v, P, T, g, t and H denote the local, thermal diffusivity, density, viscosity, velocity, pressure, temperature, gravitational acceleration, time and internal heat sources, respectively.

Several non-dimensional numbers describe mantle flow. Among them are the Rayleigh number, Prandtl number and Reynolds number. The Rayleigh number measures the ratio of the heat carried by the convecting mantle to that carried by conduction and is on the order of 10^8. The high Rayleigh number implies that the mantle is in a state of vigorous convection. The Prandtl number is a measure of the relative importance of viscous forces in diffusing momentum of the mantle compared with heat and is on the order of 10^{24}. Due to the high value of the mantle's Prandtl number, the mantle is typically taken to have infinite Prandtl number. The Reynolds number is a ratio of inertial to viscous forces and is on the order of 10^{-20} for the mantle. The very low Reynolds number of the mantle explains why inertia effects are negligible in mantle convection, unlike in the atmosphere.

This absence of inertia also gives the mantle its characteristic creeping flow.

Over the past two decades, there has been much progress in understanding mantle convection through high resolution, computationally intensive, scenario simulations (e.g Kronbichler et al. 2012; Burstedde et al. 2013; Heister et al. 2017; Bauer et al. 2020). Mantle convection modeling is a computationally intensive application, requiring large numerical grids and many time steps to represent the system with spatial and temporal resolutions fine enough to allow for the use of Earth-like physical parameters. Currently a number of 3D spherical mantle convection software are in use, two of which are the CitcomS (Zhong et al., 2000) and the TERRA (Bunge et al., 1997) codes. The latter is maintained by the geodynamics group at LMU Muenchen. The Terra code uses nodal first order finite elements, employs an icosahedral mesh for geometry representation, is MPI (Message Passing Interface) parallel and applies an advanced multigrid algorithm with line smoothers to achieve good algorithmic scalability and a high hardware efficiency. It is thus now feasible to create realistic models of mantle convection.

An initial condition for modelling mantle flow comes from present-day state estimates pertaining to the mantle volume as derived from a combination of global 3-D seismic tomography (e.g., Ritsema et al. 2011; Simmons et al. 2007) with mantle mineralogy models (Piazzoni et al. 2007; Stixrude and Lithgow-Bertelloni 2011; Chust et al. 2017). There are, however, uncertainties in the interpretation of tomographically imaged mantle structure. On the one hand, arguments have been made for both purely thermal and thermochemical interpretations of mantle seismic structure (Trampert et al. 2004; McNamara and Zhong 2005; Simmons et al. 2009; Schuberth et al. 2009a,b; Davies et al. 2012) with each approach producing different convective flow scenarios. On the other hand, the seismic inversion process is subject to its own uncertainties. Specifically, limited data coverage in seismic studies implies that the tomographic inverse problem is ill-posed. Thus, regularization methods typically have to be applied. These methods, however, impact the shape and amplitude of imaged seismic anomalies (Trampert and Spetzler, 2006), which hinders their interpretation. The current limits of seismic tomography thus imply that dynamically significant structures are either smeared or completely absent (Schuberth et al. 2009a; Ritsema et al. 2011). These effects generate errors in the initial condition field of mantle models.

The chaotic nature of mantle convection (Stewart and Turcotte, 1989) at its high Rayleigh/infinite Prandtl number implies that the mantle is sensitive to these initial condition errors. This behaviour is termed the *butterfly effect* — two mantle models that are otherwise identical except for a slight altering in their initial conditions will diverge in their trajectories over time and become uncorrelated (Bello et al., 2014). Given the butterfly effect, one may be tempted to conclude that it is impossible to construct robust, reliable trajectories of mantle flow. However, geodynamicists have shown (Vynnytska and Bunge 2015; Colli et al. 2015; Bocher et al. 2016, 2018) that by assimilating state estimates of the surface velocity field produced by a mantle convection system, the butterfly effect can be mitigated.

By exploiting this development, it is possible to create trajectories of mantle flow that link a given mantle state at one time to its state at a different time. Through such time trajectories, mantle convection models can be effectively tested against observations gleaned from the geologic record. In theory, one could construct a mantle flow trajectory by taking the mantle state at present-day and modelling it forward in time. However, given that mantle flow evolves on a timescale of Myrs, as mentioned earlier, it is unreasonable to do so, if one wanted to test these models against the geologic record. To overcome this hindrance, two key modelling techniques have been developed. The first, referred to as mantle circulation models (MCMs), starts off with a randomly chosen past state of the mantle (e.g. at the Mesozoic (252 - 60 Million years ago (Ma)) or Cenozoic (60 Ma)) and models mantle flow forward in time while assimilating plate motions and subduction histories over the entire time (Ricard et al. 1993; Bunge et al. 1998; McNamara and Zhong 2005; Bower et al. 2013; Flament et al. 2014). The second, known as the adjoint method (Bunge et al. 2003; Ismail-Zadeh et al. 2004; Horbach et al. 2014; Ghelichkhan and Bunge 2016; Price and Davies 2017), is another data assimilation procedure in which a present-day estimate of the mantle is obtained from seismic tomography (Simmons et al. 2007; Ritsema et al. 2011; French and Romanowicz 2014) and past mantle flow is reconstructed via optimization of a misfit function, in a process referred to as retrodiction (Colli et al. 2018; Ghelichkhan et al. 2021).

As noted earlier, mantle convection produces significant vertical deflections of the Earth's surface, away from its isostatically compensated state (Pekeris, 1935). These deflections, termed dynamic topography (Hager et al., 1985), have been extensively studied by geoscientists. Information on the scale, amplitude and temporal evolution of dynamic topography have been inferred through calculations of oceanic residual bathymetry (Hoggard et al. 2017; Holdt et al. 2022), studies of river profiles (Roberts and White, 2010), sediment compaction (Japsen, 2018) and provenance (Meinhold 2010; Şengör 2001), landform analysis (Guillocheau et al., 2018) based on planation surfaces (King, 1955), estimates of palaeoaltimetry (Kohn and Dettman, 2018), constraints from thermochronological data (Ehlers and Farley, 2003) or quantifications of sediment budgets at the scale of continental margins (Guillocheau et al. 2012; Said et al. 2015a,b). Additional inferences have been drawn from geological hiatus maps (Friedrich et al. 2018; Vibe et al. 2018; Carena et al. 2019; Hayek et al. 2020, 2021), palaeobiological and palaeoenvironmental data (Fernandes and Roberts, 2020), past sea-level markers (DiCaprio et al. 2009; Matthews et al. 2011; Stephenson et al. 2019) and sequence stratigraphy (Czarnota et al. 2013; Richards et al. 2016; Hartley et al. 2011). These observations provide a glimpse into the surface expressions of geologically recent mantle convection over the past 100 Myrs.

The African continent presents an exceptional opportunity to explore the interaction between dynamic topography and mantle convection. An interesting attribute of the continent is its distinct Basin and Swell topography which has long been suggested to result from convective processes in the underlying mantle (e.g. Burke and Gunnell, 2008). Further evidence for the interaction between African dynamic topography and mantle flow

comes from river profile studies (Paul et al., 2014) which also suggest that the modern African topography developed since the Oligocene (33 - 23 Ma). In a seminal work, Bond (1978, 1979) analysed continent-scale sediment distributions to argue for substantial uplift of continental platforms. He concluded that Africa experienced late Tertiary (66 - 2 Ma) uplift relative to other continents (Bond, 1978), in agreement with Burke et al. (1973). The African plate has moved slowly North-eastward within a hot spot frame of reference since the early Oligocene (Burke, 1996), implying that the analysis of the vertical motions of Africa is not complicated by horizontal plate motions (Lithgow-Bertelloni and Silver, 1998). Turning to southern Africa, there is a complete absence of marine sediments in both the Oligocene and Pleistocene (2.5 Ma - 11 thousand years ago), suggesting that this part of the continent reached a high elevation in the Oligocene, subsided in the Miocene-Pliocene (23 - 5 Ma), and has been on the rise again since the latest Pliocene (5 - 2.5 Ma) or Pleistocene (Carena et al., 2019).

The essential role of dynamic topography has long been recognized by geodynamicists in their studies of the geoid. They realized that the mass anomalies associated with surface deflections yield gravity anomalies of comparable amplitude with the driving mantle density contrasts, thus accounting for the existence of dynamic topography (Richards and Hager 1984; Ricard et al. 1984; Forte and Peltier 1991). This explains why the dynamic topography of Earth represents a crucial geological observation against which mantle convection models can be tested. Another reason for testing mantle models against dynamic topography is that mantle convection, as expressed in terms of time-dependent flow, cannot be directly observed. As such, one must link mantle models to their surface manifestations, including dynamic topography. To this end, one can construct time trajectories of mantle flow and use them to obtain predictions of dynamic topography. These predictions would then be compared to the real Earth dynamic topography (see Flament et al., 2013, for a recent comparison of dynamic topography maps) and the model parameters can be thus adjusted until a best fit between model and observation is found.

In comparing model-predicted dynamic topography to the observed dynamic topography, several approaches are possible. Qualitative comparisons by visually identifying areas of (dis-)agreement on predicted and observed dynamic topography maps (e.g. Colli et al. 2018) are an option. On the other hand, quantitative gridpoint analyses of dynamic topography fields, such as root-mean-square (rms) errors/amplitudes (Flament et al., 2013) and spectral decompositions/correlations (Davies et al., 2019) offer a first order measure of model performance in numerical terms. These quantitative measures, however, suffer from a key drawback that has been explored extensively by meteorologists in the context of weather models (Baldwin and Kain 2006; Casati et al. 2008; Wilks 2011; Jolliffe and Stephenson 2012): it is often difficult to infer a physical interpretation of their numerical output. This is because these measures do not offer information regarding the exact manner in which a model prediction (dis-)agrees with the observation. Also, the results of these measures are often different from what one would infer based on a visual examination of the predicted and observed data. For instance, it is possible for a predicted dynamic

topography field to match observed data in terms of timing, intensity and pattern of uplift (or subsidence) but to be wrong in location. An informed visual observation would classify this as a good prediction and separately account for the location error. A gridpoint-based rms error or correlation score, however, would penalize the prediction and classify it as poor. This is a known concept in meteorology, where it is appropriately termed the *double penalty problem* (e.g. Anthes 1983; Mass et al. 2002). By double penalty, it is meant that a prediction which closely matches an observation in all other respects except in location is penalized twice; first at the points in the prediction that do not overlap the observation, and at those points in the observation that do not overlap the prediction. As such, new approaches for the comparison of model-predicted with real Earth dynamic topography need to be investigated.

One such approach is the usage of object-based verification techniques (see Gilleland et al., 2009, for a recent summary). Such techniques have been applied by meteorologists to assess forecasts of extratropical and lee cyclones (Wernli and Schwierz 2006; Smith and Mullen 1993), sea breezes (Case et al., 2004), precipitation (Ebert and McBride 2000; Davis et al. 2006a,b, 2009) as well as deep, moist convection (Fowle and Roebber 2003; Done et al. 2004). These object-based methods decompose 2-D weather fields of prediction and observation into their distinct objects and compare prediction with observation based on the properties of identified objects. Since the dynamic topography field is also a 2-D field, it is instructive to investigate if, and to what extent, such object-based measures can be applied in comparing model-predicted to real Earth dynamic topography. It is, however, necessary, as a first step, to test such measures on purely synthetic dynamic topography maps so that they are properly understood, without the additional complexities that arise while dealing with real Earth dynamic topography. It is worth recalling a few scaling rules. Mantle convection is often expressed in terms of a transit time for which one divides the mantle depth ($\approx 3000km$) by a characteristic velocity ($3cm/yr$) to obtain a transit time of $\approx$ 100 Myrs. On the other hand, weather patterns would have a velocity scale of 1-50 m/s (Cushman-Roisin and Beckers, 2011). If we assume a synoptic lengthscale of 5000 km, and a velocity scale of 50 km/h, this translates into a transit time of a few days in the atmosphere. Given that key observables of the mantle convection system are coming into focus for 100 Myrs, equivalent to a few days of weather in the atmosphere, it is attractive to use these object-based metrics in the evaluation of mantle convection models.

In this thesis, I investigate the construction of robust mantle flow trajectories and their link to dynamic topography. I also delve into the meteorological literature and probe to what extent metrics for assessing the accuracy of meteorological model predictions can be applied to dynamic topography predictions. In this process, I adapt and develop metrics suitable for dynamic topography. Furthermore, I explore the evolution of the southern Africa dynamic topography high as produced by the adjoint-based reconstruction of Ghelichkhan et al. (2021) and apply the developed metrics in comparing multiple predictions of this dynamic topography. I arrange my thesis as follows: Chapter 2 addresses the question: given the butterfly effect, can reliable mantle flow trajectories even be constructed? Here,

I employ 3-D spherical synthetic mantle convection models via twin experiments (Lorenz, 1965) and make links to dynamic topography. I show that it is possible to construct robust, accurate mantle flow trajectories if the horizontal component of the surface velocity field of one twin is assimilated into the other twin, despite uncertainties associated with the initial heterogeneity state of the mantle, thus confirming earlier results (Colli et al. 2015; Vynnytska and Bunge 2015; Bocher et al. 2016, 2018). I also introduce the Taylor Diagram (Taylor, 2001), originally developed in meteorology, and apply it to the comparison of dynamic topography maps. In Chapter 3, I explore object-based meteorological metrics and their applicability in the assessment of dynamic topography predictions. Here, I show that these metrics are well-suited to the study of dynamic topography, albeit with some modifications. In this regard, I develop a metric that separately assesses uplift and subsidence regions on dynamic topography maps based on a shape comparison of the boundaries surrounding these regions. The results in this chapter also reinforce my earlier findings that velocity assimilation leads to reliable mantle flow trajectories. In Chapter 4, I apply the developed metrics to study the evolution of the southern Africa uplift based on synthetic dynamic topography predictions obtained from multiple mantle flow reconstructions (Ghelichkhan et al., 2021) via the adjoint method. I also do a comparison of global and regional assessment metrics. The results of this chapter display the power of these object-based metrics and open the door to their application in the more complex real Earth. Finally, in Chapter 5, I provide an outlook into the future of constructing mantle flow trajectories.

Bibliography

Anthes, R. A. (1983). Regional Models of the Atmosphere in Middle Latitudes. *Monthly Weather Review*, (6):1306–1335.

Baldwin, M. E. and Kain, J. S. (2006). Sensitivity of several performance measures to displacement error, bias, and event frequency. *Weather and forecasting*, 21(4):636–648.

Bauer, S., Bunge, H.-P., Drzisga, D., Ghelichkhan, S., Huber, M., Kohl, N., Mohr, M., Rüde, U., Thönnes, D., and Wohlmuth, B. (2020). In *Software for Exascale Computing - SPPEXA 2016-2019*, Cham.

Bello, L., Coltice, N., Rolf, T., and Tackley, P. J. (2014). On the predictability limit of convection models of the Earth's mantle. *Geochem. Geophys. Geosyst.*, (15).

Bocher, M., Coltice, N., Fournier, A., and Tackley, P. (2016). A sequential data assimilation approach for the joint reconstruction of mantle convection and surface tectonics. *Geophysical Journal International*, 204:200–214.

Bocher, M., Fournier, A., and Coltice, N. (2018). Ensemble Kalman filter for the reconstruction of the Earth's mantle circulation. *Nonlinear Processes in Geophysics*, (1):99–123.

Bond, G. (1978). Evidence for late tertiary uplift of africa relative to north america, south america, australia and europe. *The Journal of Geology*, 86(1):47–65.

Bond, G. (1978). Speculations on real sea-level changes and vertical motions of continents at selected times in the Cretaceous and Tertiary Periods. *Geology*, 6(4):247.

Bond, G. C. (1979). Evidence for some uplifts of large magnitude in continental platforms. *Tectonophysics*, 61(1):285–305.

Bower, D. J., Gurnis, M., and Seton, M. (2013). Lower mantle structure from paleogeographically constrained dynamic earth models. *Geochemistry, Geophysics, Geosystems*, 14(1):44–63.

Braun, J. (2010). The many surface expressions of mantle dynamics. *Nature Geoscience*, 3(12):825–833.

Bunge, H.-P., Hagelberg, C. R., and Travis, B. J. (2003). Mantle circulation models with variational data assimilation: inferring past mantle flow and structure from plate motion histories and seismic tomography. *Geophysical Journal International*, 152(2):280–301.

Bunge, H.-P., Richards, M. A., and Baumgardner, J. R. (1997). A sensitivity study of three-dimensional spherical mantle convection at 108 Rayleigh number: Effects of depth-dependent viscosity, heating mode, and an endothermic phase change. *Journal of Geophysical Research: Solid Earth*, 102(B6):11991–12007.

Bunge, H.-P., Richards, M. A., Lithgow-Bertelloni, C., Baumgardner, J. R., Grand, S. P., and Romanowicz, B. A. (1998). Time Scales and Heterogeneous Structure in Geodynamic Earth Models. *Science*, 280(5360):91–95.

Burke, K. (1996). Africa's distinctive behavior over the past 30 million years.

Burke, K. and Gunnell, Y. (2008). The African Erosion Surface: A Continental-Scale Synthesis of Geomorphology, Tectonics, and Environmental Change over the Past 180 Million Years. In *The African Erosion Surface: A Continental-Scale Synthesis of Geomorphology, Tectonics, and Environmental Change over the Past 180 Million Years*. Geological Society of America.

Burke, K. C. A., Whiteman, A. J., et al. (1973). Uplift, rifting and the break-up of africa.

Burstedde, C., Stadler, G., Alisic, L., Wilcox, L. C., Tan, E., Gurnis, M., and Ghattas, O. (2013). Large-scale adaptive mantle convection simulation. *Geophysical Journal International*, 192(3):889–906.

Carena, S., Bunge, H.-P., and Friedrich, A. M. (2019). Analysis of geological hiatus surfaces across Africa in the Cenozoic and implications for the timescales of convectively-maintained topography. *Canadian Journal of Earth Sciences*, 56(12):1333–1346.

Casati, B., Wilson, L., Stephenson, D., Nurmi, P., Ghelli, A., Pocernich, M., Damrath, U., Ebert, E., Brown, B., and Mason, S. (2008). Forecast verification: current status and future directions. *Meteorological Applications: A journal of forecasting, practical applications, training techniques and modelling*, 15(1):3–18.

Case, J. L., Manobianco, J., Lane, J. E., Immer, C. D., and Merceret, F. J. (2004). An objective technique for verifying sea breezes in high-resolution numerical weather prediction models.

Cathles, L. M. (1975). *The viscosity of the earth's mantle [by] Lawrence M. Cathles, III*. Princeton University Press Princeton.

Chust, T. C., Steinle-Neumann, G., Dolejš, D., Schuberth, B. S. A., and Bunge, H.-P. (2017). MMA-EoS: A Computational Framework for Mineralogical Thermodynamics. *Journal of Geophysical Research: Solid Earth*, 122(12):9881–9920.

Colli, L., Bunge, H.-P., and Schuberth, B. S. A. (2015). On retrodictions of global mantle flow with assimilated surface velocities. *Geophys. Res. Lett.*, 42.

Colli, L., Ghelichkhan, S., Bunge, H.-P., and Oeser, J. (2018). Retrodictions of Mid Paleogene mantle flow and dynamic topography in the Atlantic region from compressible high resolution adjoint mantle convection models: Sensitivity to deep mantle viscosity and tomographic input model. *Gondwana Research*, pages 252–272. Rifting to Passive Margins.

Cushman-Roisin, B. and Beckers, J.-M. (2011). *Introduction to geophysical fluid dynamics: physical and numerical aspects*. Academic press.

Czarnota, K., Hoggard, M. J., White, N., and Winterbourne, J. (2013). Spatial and temporal patterns of Cenozoic dynamic topography around Australia. *Geochemistry, Geophysics, Geosystems*, 14(3):634–658.

Davies, D. R., Goes, S., Davies, J., Schuberth, B., Bunge, H.-P., and Ritsema, J. (2012). Reconciling dynamic and seismic models of Earth's lower mantle: The dominant role of thermal heterogeneity. *Earth and Planetary Science Letters*, 353-354:253–269.

Davies, D. R., Valentine, A. P., Kramer, S. C., Rawlinson, N., Hoggard, M. J., Eakin, C. M., and Wilson, C. R. (2019). Earth's multi-scale topographic response to global mantle flow. *Nature Geoscience*, 12.

Davies, G. and Richards, A. (1992). Mantle Convection. *The Journal of Geology*, 100(2):151–206.

Davis, C., Brown, B., and Bullock, R. (2006a). Object-Based Verification of Precipitation Forecasts. Part I: Methodology and Application to Mesoscale Rain Areas. *Monthly Weather Review*, 134(7):1772.

Davis, C., Brown, B., and Bullock, R. (2006b). Object-Based Verification of Precipitation Forecasts. Part II: Application to Convective Rain Systems. *Monthly Weather Review*, 134(7):1785.

Davis, C. A., Brown, B. G., Bullock, R., and Halley-Gotway, J. (2009). The Method for Object-Based Diagnostic Evaluation (MODE) Applied to Numerical Forecasts from the 2005 NSSL/SPC Spring Program. *Weather and Forecasting*, 24(5):1252.

DiCaprio, L., Gurnis, M., and Müller, R. D. (2009). Long-wavelength tilting of the Australian continent since the Late Cretaceous. *Earth and Planetary Science Letters*, 278(3):175–185.

Done, J., Davis, C., and Weisman, M. (2004). The next generation of nwp: Explicit forecasts of convection using weather research and forecast (wrf) model.

Ebert, E. E. and McBride, J. L. (2000). Verification of precipitation in weather systems: determination of systematic errors. *Journal of Hydrology*, 239(1):179–202.

Ehlers, T. A. and Farley, K. A. (2003). Apatite (U–Th)/He thermochronometry: methods and applications to problems in tectonic and surface processes. *Earth and Planetary Science Letters*, 206(1):1–14.

Fernandes, V. M. and Roberts, G. G. (2020). Cretaceous to Recent net continental uplift from paleobiological data: Insights into sub-plate support. *GSA Bulletin*, 133(5-6):1217–1236.

Flament, N., Gurnis, M., and Müller, R. D. (2013). A review of observations and models of dynamic topography. *Lithosphere*, 5(2):189–210.

Flament, N., Gurnis, M., Williams, S., Seton, M., Skogseid, J., Heine, C., and Müller, R. D. (2014). Topographic asymmetry of the south atlantic from global models of mantle flow and lithospheric stretching. *Earth and Planetary Science Letters*, 387:107–119.

Forte, A. M. and Peltier, R. (1991). Viscous flow models of global geophysical observables: 1. forward problems. *Journal of Geophysical Research: Solid Earth*, 96(B12):20131–20159.

Fowle, M. A. and Roebber, P. J. (2003). Short-range (0–48 h) numerical prediction of convective occurrence, mode, and location.

Fowler, C. M. R. (2004). *The Solid Earth*.

French, S. W. and Romanowicz, B. A. (2014). Whole-mantle radially anisotropic shear velocity structure from spectral-element waveform tomography. *Geophysical Journal International*, 199(3):1303–1327.

Friedrich, A. M., Bunge, H.-P., Rieger, S. M., Colli, L., Ghelichkhan, S., and Nerlich, R. (2018). Stratigraphic framework for the plume mode of mantle convection and the analysis of interregional unconformities on geological maps. *Gondwana Research*, pages 159–188. Rifting to Passive Margins.

Ghelichkhan, S. and Bunge, H.-P. (2016). The compressible adjoint equations in geodynamics: derivation and numerical assessment. *International Journal on Geomathematics (GEM)*.

Ghelichkhan, S., Bunge, H.-P., and Oeser, J. (2021). Global mantle flow retrodictions for the early Cenozoic using an adjoint method: evolving dynamic topographies, deep mantle structures, flow trajectories and sublithospheric stresses. *Geophysical Journal International*, 226(2):1432–1460.

Gilleland, E., Ahijevych, D., Brown, B. G., Casati, B., and Ebert, E. E. (2009). Intercomparison of spatial forecast verification methods. *Weather and Forecasting*, 24(5):1416–1430.

Guillocheau, F., Rouby, D., Robin, C., Helm, C., Rolland, N., Le Carlier de Veslud, C., and Braun, J. (2012). Quantification and causes of the terrigeneous sediment budget at the scale of a continental margin: a new method applied to the Namibia–South Africa margin. *Basin Research*, 24(1):3–30.

Guillocheau, F., Simon, B., Baby, G., Bessin, P., Robin, C., and Dauteuil, O. (2018). Planation surfaces as a record of mantle dynamics: The case example of Africa. *Gondwana Research*, 53:82–98. Rifting to Passive Margins.

Hager, B. H., Clayton, R. W., Richards, M. A., Comer, R. P., and Dziewonski, A. M. (1985). Lower mantle heterogeneity, dynamic topography and the geoid. *Nature*, 313.

Hartley, R. A., Roberts, G. G., White, N., and Richardson, C. (2011). Transient convective uplift of an ancient buried landscape. *Nature Geoscience*, 4.

Haskell, N. A. (1935). The Motion of a Viscous Fluid Under a Surface Load. *Physics*, 6(8):265–269.

Hayek, J. N., Vilacís, B., Bunge, H.-P., Friedrich, A. M., Carena, S., and Vibe, Y. (2021). Correction: Continent-scale hiatus maps for the atlantic realm and australia since the upper jurassic and links to mantle flow-induced dynamic topography. *Proc. R. Soc. A*, 477(2251):20210437.

Hayek, N., Vilacis, B., Bunge, H.-P., Friedrich, A., Carena, S., and Vibe, Y. (2020). Continent-scale Hiatus Maps for the Atlantic Realm and Australia since the Upper Jurassic and links to mantle flow induced dynamic topography. *Proc. R. Soc. A*.

Heister, T., Dannberg, J., Gassmöller, R., and Bangerth, W. (2017). High accuracy mantle convection simulation through modern numerical methods – II: realistic models and problems. *Geophysical Journal International*, 210(2):833–851.

Hoggard, M. J., Winterbourne, J., Czarnota, K., and White, N. (2017). Oceanic residual depth measurements, the plate cooling model, and global dynamic topography. *Journal of Geophysical Research: Solid Earth*, 122(3):2328–2372.

Holdt, M. C., White, N. J., Stephenson, S. N., and Conway-Jones, B. W. (2022). Densely sampled global dynamic topographic observations and their significance. *Journal of Geophysical Research: Solid Earth*, 127(7):e2022JB024391. e2022JB024391 2022JB024391.

Horbach, A., Bunge, H.-P., and Oeser, J. (2014). The adjoint method in geodynamics: derivation from a general operator formulation and application to the initial condition problem in a high resolution mantle circulation model. *GEM - International Journal on Geomathematics*, 5(2):163–194.

Ismail-Zadeh, A., Schubert, G., Tsepelev, I., and Korotkii, A. (2004). Inverse problem of thermal convection: numerical approach and application to mantle plume restoration. *Physics of the Earth and Planetary Interiors*, 145(1):99–114.

Japsen, P. (2018). Sonic velocity of chalk, sandstone and marine shale controlled by effective stress: Velocity-depth anomalies as a proxy for vertical movements. *Gondwana Research*, 53:145–158. Rifting to Passive Margins.

Jeanloz, R. (1990). The Nature of the Earth's Core. *Annual Review of Earth and Planetary Sciences*, 18:357.

Jolliffe, I. T. and Stephenson, D. B. (2012). *Forecast verification: a practitioner's guide in atmospheric science*. John Wiley & Sons.

Kaufmann, G. and Lambeck, K. (2002). Glacial isostatic adjustment and the radial viscosity profile from inverse modeling. *Journal of Geophysical Research: Solid Earth*, 107(B11):ETG 5–1–ETG 5–15.

King, L. C. (1955). Pediplanation and Isostasy: An Example from South Africa. *Quarterly Journal of the Geological Society*, 111(1-4):353–359.

Kohn, M. J. and Dettman, D. L. (2018). *5. Paleoaltimetry from Stable Isotope Compositions of Fossils*, pages 119–154. De Gruyter.

Kronbichler, M., Heister, T., and Bangerth, W. (2012). High accuracy mantle convection simulation through modern numerical methods. *Geophysical Journal International*, 191(1):12–29.

Lithgow-Bertelloni, C. and Silver, P. G. (1998). Dynamic topography, plate driving forces and the African superswell. *Nature*, 395:269–272.

Lorenz, E. N. (1965). A study of the predictability of a 28-variable atmospheric model. *Tellus*, 17(3):321–333.

Mass, C. F., Ovens, D., Westrick, K., and Colle, B. A. (2002). Does Increasing Horizontal Resolution Produce More Skillful Forecasts?. *Bulletin of the American Meteorological Society*, 83(3):407–430.

Matthews, K. J., Hale, A. J., Gurnis, M., Müller, R. D., and DiCaprio, L. (2011). Dynamic subsidence of Eastern Australia during the Cretaceous. *Gondwana Research*, 19(2):372–383.

McNamara, A. K. and Zhong, S. (2005). Thermochemical structures beneath Africa and the Pacific Ocean. *Nature*, 437.

Meinhold, G. (2010). Rutile and its applications in earth sciences. *Earth-Science Reviews*, 102(1):1–28.

Mitrovica, J. X. (1996). Haskell [1935] revisited. *Journal of Geophysical Research: Solid Earth*, 101(B1):555–569.

Morgan, W. J. (1971). Convection Plumes in the Lower Mantle. , 230(5288):42–43.

Paul, J. D., Roberts, G. G., and White, N. (2014). The african landscape through space and time. *Tectonics*, 33(6):898–935.

Paulson, A., Zhong, S., and Wahr, J. (2007). FAST TRACK PAPER: Inference of mantle viscosity from GRACE and relative sea level data. *Geophysical Journal International*, 171(2):497–508.

Pekeris, C. L. (1935). Thermal Convection in the Interior of the Earth. *Geophysical Supplements to the Monthly Notices of the Royal Astronomical Society*, 3:343–367.

Piazzoni, A. S., Steinle-Neumann, G., Bunge, H.-P., and Dolejs, D. (2007). A mineralogical model for density and elasticity of the Earth's mantle. *Geochemistry, Geophysics, Geosystems*, 8(11).

Price, M. G. and Davies, J. H. (2017). Profiling the robustness, efficiency and limits of the forward-adjoint method for 3-D mantle convection modelling. *Geophysical Journal International*, 212(2):1450–1462.

Ricard, Y., Fleitout, L., and Froidevaux, C. (1984). Geoid heights and lithospheric stresses for a dynamic Earth. *Annales Geophysicae*, 2:267–285.

Ricard, Y., Richards, M., Lithgow-Bertelloni, C., and Le Stunff, Y. (1993). A geodynamic model of mantle density heterogeneity. *Journal of Geophysical Research: Solid Earth*, 98(B12):21895–21909.

Richards, F. D., Hoggard, M. J., and White, N. J. (2016). Cenozoic epeirogeny of the Indian peninsula. *Geochemistry, Geophysics, Geosystems*, 17(12):4920–4954.

Richards, M. A. and Hager, B. H. (1984). Geoid anomalies in a dynamic Earth. *Journal of Geophysical Research: Solid Earth*, 89(B7):5987–6002.

Ritsema, J., A. Deuss, H. v. H., and Woodhouse, J. (2011). S40RTS: a degree-40 shear-velocity model for the mantle from new Rayleigh wave dispersion, teleseismic traveltime and normal-mode splitting function measurements. *Geophysical Journal International*, 184:1223–1236.

Roberts, G. G. and White, N. (2010). Estimating uplift rate histories from river profiles using African examples. *Journal of Geophysical Research: Solid Earth*, 115(B2).

Said, A., Moder, C., Clark, S., and Abdelmalak, M. M. (2015a). Sedimentary budgets of the Tanzania coastal basin and implications for uplift history of the East African rift system. *Journal of African Earth Sciences*, 111:288–295.

Said, A., Moder, C., Clark, S., and Ghorbal, B. (2015b). Cretaceous–Cenozoic sedimentary budgets of the Southern Mozambique Basin: Implications for uplift history of the South African Plateau. *Journal of African Earth Sciences*, 109:1–10.

Schuberth, B. S. A., Bunge, H.-P., and Ritsema, J. (2009a). Tomographic filtering of high-resolution mantle circulation models: Can seismic heterogeneity be explained by temperature alone? *Geochemistry, Geophysics, Geosystems*, (5).

Schuberth, B. S. A., Bunge, H.-P., Steinle-Neumann, G., Moder, C., and Oeser, J. (2009b). Thermal versus elastic heterogeneity in high-resolution mantle circulation models with pyrolite composition: High plume excess temperatures in the lowermost mantle. *Geochemistry, Geophysics, Geosystems*, 10(1).

Şengör, A. M. C. (2001). Elevation as indicator of mantle-plume activity. In *Mantle plumes: their identification through time*. Geological Society of America.

Simmons, N., Forte, A., and Grand, S. (2007). Thermochemical structure and dynamics of the african superplume. *Geophys. Res. Lett*, 34(2).

Simmons, N. A., Forte, A. M., and Grand, S. P. (2009). Joint seismic, geodynamic and mineral physical constraints on three-dimensional mantle heterogeneity: Implications for the relative importance of thermal versus compositional heterogeneity. *Geophysical Journal International*, 177(3):1284–1304.

Smith, B. B. and Mullen, S. L. (1993). An evaluation of sea level cyclone forecasts produced by nmc's nested-grid model and global spectral model.

Stephenson, S. N., White, N. J., Li, T., and Robinson, L. F. (2019). Disentangling interglacial sea level and global dynamic topography: Analysis of Madagascar. *Earth and Planetary Science Letters*, 519:61–69.

Stewart, C. A. and Turcotte, D. L. (1989). The route to chaos in thermal convection at infinite Prandtl number: 1. Some trajectories and bifurcations. *Journal of Geophysical Research: Solid Earth*, 94(B10):13707–13717.

Stixrude, L. and Lithgow-Bertelloni, C. (2011). Thermodynamics of mantle minerals - II. Phase equilibria. *Geophysical Journal International*, 184(3):1180–1213.

Taylor, K. E. (2001). Summarizing multiple aspects of model performance in a single diagram. *Journal of Geophysical Research: Atmospheres*, 106(D7):7183–7192.

Trampert, J., Deschamps, F., Resovsky, J., and Yuen, D. (2004). Probabilistic Tomography Maps Chemical Heterogeneities Throughout the Lower Mantle. *Science*, 306(5697):853–856.

Trampert, J. and Spetzler, J. (2006). FAST TRACK PAPER: Surface wave tomography: finite-frequency effects lost in the null space. *Geophysical Journal International - GEOPHYS J INT*, 164:394–400.

Vibe, Y., Friedrich, A., Bunge, H.-P., and Clark, S. (2018). Correlations of oceanic spreading rates and hiatus surface area in the North Atlantic realm. *Lithosphere*, 10(5):677–684.

Vynnytska, L. and Bunge, H. (2015). Restoring past mantle convection structure through fluid dynamic inverse theory: regularisation through surface velocity boundary conditions. *Int. J. Geomath.*, 6.

Wernli, H. and Schwierz, C. (2006). Surface Cyclones in the ERA-40 Dataset (1958 2001). Part I: Novel Identification Method and Global Climatology. *Journal of Atmospheric Sciences*, 63(10):2486–2507.

Wilks, D. S. (2011). *Statistical methods in the atmospheric sciences*, volume 100. Academic press.

Zhong, S., Zuber, M. T., Moresi, L., and Gurnis, M. (2000). Role of temperature-dependent viscosity and surface plates in spherical shell models of mantle convection. *Journal of Geophysical Research: Solid Earth*, 105(B5):11063–11082.

Chapter 2

Robust Global Mantle Flow Trajectories and their Validation via Dynamic Topography Histories

This chapter was entirely written by A. Taiwo. On 11. April 2023, this chapter was accepted for publication by Geophysical Journal International. It addresses the problem whether reliable trajectories of global mantle flow can be constructed despite the butterfly effect and explores the usage of model-predicted dynamic topography as a proxy for assessing mantle flow trajectories.

Robust Global Mantle Flow Trajectories and their Validation via Dynamic Topography Histories

A. Taiwo[1]

[1] Department of Earth and Environmental Sciences, University of Munich, *80333* Munich, Germany. E-mail: ataiwo@geophysik.uni-muenchen.de

ABSTRACT

The ability to construct time-trajectories of mantle flow is crucial to move from studies of instantaneous to time-dependent Earth models and to exploit geologic constraints for mantle convection modelling. But mantle convection is chaotic and subject to the butterfly effect: the trajectories of two identical mantle convection models initialized with slightly different temperature fields diverge exponentially in time until they become uncorrelated. Because one may use seismic inferences about the mantle state as a starting or terminal condition to project mantle flow forward or backward in time, and because the seismic inference is invariably subject to uncertainties, this seemingly would rule out any construction of robust mantle flow trajectories. Here we build upon earlier work which showed that assimilation of the horizontal component of the surface velocity field from a known reference model allows one to overcome the butterfly effect and to construct robust mantle flow trajectories, regardless of the choice of the initial state perturbation. To this end, we use high resolution 3-D spherical mantle convection models in four end-member configurations: an isoviscous purely internally heated model, an isoviscous purely bottom heated model, a model with a radial increase in viscosity along with pure internal heating as well as a model that combines the effects of radial viscosity increase, internal and bottom heating. In order to capture the impact of seismic filtering, we perturb the initial temperature fields of these end-member models through either radial or horizontal smoothing of the temperature field or the application of the tomographic filter of seismic model S20RTS. We assess the quality of the constructed model trajectories via a number of statistical measures as well as comparisons of their dynamic topography histories. The latter is an essential step since mantle flow cannot be directly observed but has to be inferred via its surface manifestations. Importantly, linking mantle flow to surface observations yields patterns representable on a latitude-longitude grid similar to meteorological observables such as precipitation. This invites the application of meteorological quality metrics, such as the power ratio and Taylor diagram, to assess the quality of mantle flow trajectories. We introduce these metrics for the first time in the context of mantle convection and demonstrate their viability based on the compact manner in which they summarize model performance.

Keywords: Mantle processes, Numerical modelling, Dynamics: convection currents, and mantle plumes, Statistical methods, Dynamics of lithosphere and mantle, Plametary Interiors

1 INTRODUCTION

Mantle convection provides the driving forces that support plate tectonics, earthquakes, mountain building and a host of other geological activities. Numerical models that simulate mantle convection have seen great improvement in the last couple of decades (Zhong et al. (2015); Coltice et al. 2017). And coupled with increasing computational power, these parallelized, highly scalable and progressively more sophisticated models are simulating mantle convection at very high numerical resolutions (e.g Kronbichler et al. 2012; Burstedde et al. 2013; Heister et al. 2017; Bauer et al. 2020). A number of mantle properties, such as its rheology and chemical composition are, however, only poorly known. There is thus a need to test mantle convection models against geological observables. One way of doing this is by using these models along with our best guess for mantle parameters to make predictions over time about a geological observable, such as the convectively-maintained topography, known as dynamic topography (e.g. Hager et al. 1985). One would then compare how well these predictions match the actual observable. Models of mantle flow can in theory be allowed to evolve into the future. However, given the very long timescales over which mantle flow evolves (millions of years), it is unreasonable to do so if one wanted to test them against the geological observables. To mitigate this fundamental problem, a data assimilation method has been developed that links the present day state of the mantle to its past states. It does so by constructing so-called retrodictions (Colli et al. 2018; Ghelichkhan et al. 2021) which, in essence, are time trajectories of geodynamic Earth models from the present day into the past. These retrodictions are then compared with constraints gleaned from the geological record. In fact, over the last few decades, geophysicists have devised various techniques to assimilate geophysical data into models of the mantle including backward advection (Steinberger and O'Connell, 1997), sequential assimilation (Bunge et al., 1998), the adjoint method (Bunge et al. 2003; Liu and Gurnis 2008) and the (ensemble) Kalman filter (Bocher et al. 2015, 2018).

Convection in the Earth's mantle is chaotic. This was demonstrated by Stewart and Turcotte (1989) who showed that the mantle's chaotic convection, which arises as a result of boundary layer instabilities, is a consequence of its high Rayleigh number/infinite Prandtl number. Two main features of chaotic systems are sensitivity to initial conditions — *i.e. butterfly effect*, — as well as ergodicity (Nikolaevsky, 1969), — *i.e. rapid mixing of model solutions or phase trajectories.* Earth scientists have for several decades studied the impact of initial condition errors on the predictability limit of other chaotic systems including the atmosphere, oceans as well as the geodynamo. Using a simple atmospheric model, Lorenz (1963, 1965) showed that chaotic circulation in the atmosphere ensured that small initial condition errors grow rapidly with time until they become intolerable. Exploiting modern computing power, Zhang et al. (2019) performed high-resolution ensemble twin experiments which suggested a predictability limit for midlatitude weather of around 10 days. Hulot et al. (2010) performed similar twin experiments for the geodynamo and suggested a predictability limit of one century. In geodynamics, Bello et al. (2014) studied the impact of small, random initial condition errors on the predictability limit of mantle convection and suggested a

predictability limit of around 95 million years (Myrs).

The predictability limit of mantle convection models can be extended by the assimilation of estimates pertaining to the state of the mantle convection system. An estimate of the present-day state can be derived from seismic tomography (Nolet, 1987). But information on the temporal evolution of the underlying mantle convection system is also present in the surface velocity field. The surface velocity field of the Earth is known over time from past plate motion models (e.g. Müller et al. 2016). Geodynamicists have learned that knowledge of this surface velocity field is key in minimising the growth of initial uncertainties in a chaotically convecting mantle and enabling a robust reconstruction of past mantle structure. Vynnytska and Bunge (2015) showed that assimilating the horizontal component of the surface velocity field into mantle convection model was necessary for restoration of past mantle structure. This was validated by Colli et al. (2015) who showed that assimilating the horizontal surface velocity field over time even led to convergence between two mantle models started from slightly different initial conditions. Also, Bocher et al. (2015) found it necessary to assimilate the horizontal surface velocity field in their Kalman-filter-based reconstruction approach. To sum up, horizontal surface motions are a key input to construct trajectories of past mantle flow. The implication of this is that they can therefore not be used as an independent test of the correctness of a mantle model.

However, in addition to horizontal motions, mantle convection also produces significant vertical deflections of the Earth's surface, away from its isostatically compensated state (Pekeris, 1935). Referred to as dynamic topography, as mentioned before (Hager et al., 1985), these deflections have received renewed attention (Braun 2010; Hoggard et al. 2016; Davies et al. 2019; Valentine and Davies 2020) including in passive margin environments (Bunge and Glasmacher, 2018), where the proximity to a base-level allows one to gauge topographic changes better than at other places. There has been much improvement in the amount and quality of dynamic topography inferences in recent years. Through calculations of oceanic residual bathymetry (Hoggard et al. 2017; Holdt et al. 2022), new information has been obtained on the present-day scale and amplitude of dynamic topography. Moreover, a wealth of geological indicators provide constraints on the temporal evolution of dynamic topography. Amongst these are studies of river profiles (Roberts and White, 2010), sediment compaction (Japsen, 2018) and provenance (Meinhold 2010; Şengör 2001), landform analysis (Guillocheau et al., 2018) based on planation surfaces (King, 1955), estimates of palaeoaltimetry (Kohn and Dettman, 2018), constraints from thermochronological data (Ehlers and Farley, 2003) or quantifications of sediment budgets at the scale of continental margins (Guillocheau et al. 2012; Said et al. 2015a,b). Further inferences are drawn from geological hiatus maps (Friedrich et al. 2018; Vibe et al. 2018; Carena et al. 2019; Hayek et al. 2020, 2021), palaeobiological and palaeoenvironmental data (Fernandes and Roberts, 2020), past sea-level markers (DiCaprio et al. 2009; Matthews et al. 2011; Stephenson et al. 2019) or sequence stratigraphy (Czarnota et al. 2013; Richards et al. 2016; Hartley et al. 2011). In a technical way, the vertical surface deflections are governed by kernels that relate dynamic topography to a unit mass anomaly of given wavelength and mantle depth (Richards and Hager 1984; Colli et al. 2016). The convolution of mass anomalies with the kernels over time thus provides an independent means of comparing retrodictions with the time evolution of Earth's dynamic topography field as inferred from geological observations. It should be noted that while kernels are appropriate for

horizontally-constant viscosity profiles, evidence from geoid studies (e.g. Ghosh et al. 2010) suggests that lateral viscosity variations may not affect results very much at the larger scales.

A prerequisite for performing mantle flow retrodictions is an estimate of the present-day state of the mantle which can be inferred from the heterogeneity structure imaged by global 3-D seismic tomography (Simmons et al. 2007; Ritsema et al. 2011; French and Romanowicz 2014). One approach to translating from seismic velocity to temperature, involves assuming a homogeneous pyrolitic mantle composition which implies a predominantly thermal origin for large-scale mantle seismic anomalies. The stable mineral assemblage and its average mechanical and thermodynamical properties at each p-T point can then be computed from thermodynamically self-consistent models of mantle mineralogy (Piazzoni et al. 2007; Stixrude and Lithgow-Bertelloni 2011; Chust et al. 2017). There are, however, uncertainties in the interpretation of tomographically imaged structures. On the one hand, arguments have been made for both purely thermal as well as thermochemical interpretations of mantle seismic heterogeneities (Trampert et al. 2004; McNamara and Zhong 2005; Simmons et al. 2009; Schuberth et al. 2009a,b; Davies et al. 2012) with each approach producing different convective flow scenarios. On the other hand, the seismic inversion process is subject to its own uncertainties. Specifically, limited data coverage in seismic studies implies that the tomographic inverse problem is ill-posed. Thus, regularization methods in form of damping and smoothing typically have to be applied. These methods, however, impact the shape and amplitude of imaged seismic anomalies (Trampert and Spetzler, 2006), which hinders their interpretation. In fact, tomographic models of the Earth show similarity on large scales, on the order of thousands of km but have significant differences over short length scales, on the order of ≈ 100 km (equivalent to a thermal boundary layer thickness) (Becker and Boschi, 2002). These small-scale structures, however, play an active role in generating buoyancies responsible for convection within the mantle. The current limits of seismic tomography thus imply that these dynamically significant structures are either smeared or completely absent (Schuberth et al. 2009a; Ritsema et al. 2011). Recently Zaroli et al. (2013) proposed certain objective measures for setting a threshold on model damping, based on data noise and measurement errors. Yet, the range of acceptable damping values is still large enough to result in a factor of ≈ 2 uncertainty in the root-mean-square (rms) amplitude of seismic anomalies. To sum up, the state estimate of the volume, derived from seismic tomography, has uncertainties related to interpretation as well as regularization.

As noted earlier, geodynamicists have investigated the construction of time trajectories for mantle flow with the aid of twin experiments (Bello et al. 2014; Colli et al. 2015; Bocher et al. 2015, 2018). However, metrics for measuring the accuracy of the constructed trajectories have focused so far on assessing the similarities of the structures generated within the mantle, which, in real-Earth applications, are not directly observable, particularly for the geological past. The dynamic topography field of the Earth, instead, is accessible and trackable over time, through a variety of proxy observables, and reflects the mantle heterogeneity structure as mediated by viscous stresses. It is therefore paramount to measure model accuracy via comparisons of predicted dynamic topography — a field that can be represented on a latitude-longitude grid. To this end, attention must be paid to work done in neighbouring disciplines such as meteorology, oceanography and hydrology amongst others. Some metrics have already been developed in meteorology for assessing the accuracy of model predictions representable on a latitude-longitude grid.

These methods range from grid-point comparisons (Taylor 2001; Roebber 2009) to object-based verification metrics (Ebert and McBride 2000; Davis et al. 2006a,b, 2009) as well as optical flow methods (Keil and Craig 2007, 2009; Marzban and Sandgathe 2010) where one field is deformed and morphed until it best matches a specified reference field.

In this paper, we build on previous work in constructing mantle convection trajectories and present trajectories for simple end-member mantle convection models with different initial heterogeneity structures as well as model parameterizations (i.e. radial viscosity profiles and heating modes). We follow the twin experiment approach (Lorenz, 1965) and introduce tomographically-relevant perturbations to the temperature field of a reference mantle. We then track their trajectories over time for cases with and without the assimilation of the horizontal component of the surface velocity field of the reference mantle model. The surface velocity field is assimilated with a gain of 1 and we assume that there are no measurement errors and that the assimilated information is perfectly known. Importantly, we begin to explore the link to dynamic topography and apply some of the previously mentioned techniques from neighbouring research disciplines to the comparison of predicted dynamic topography. We organize our paper as follows: Section 2 lists the methodology used for this study. We specify the exact nature of tomographic smoothing that we perform, describe the forward mantle convection equations and detail a number of metrics with which our twin experiments are assessed. In Section 3, we present the main results of our study. We start by showing slices of the mantle temperature field for all twin experiments. Next we display several grid-point metrics to test the efficacy of our horizontal surface velocity field assimilation scheme. Finally, we present maps of dynamic topography computed from all twin experiments and compare them. In Section 4, we discuss these results in the context of the broader geoscience literature and we draw conclusions in Section 5.

2 METHODS

We follow the twin experiment approach (Lorenz, 1965), where a reference (true state) and a perturbed mantle model are allowed to evolve forward in time and their trajectories are tracked. The true state is obtained by allowing a mantle model to evolve until a statistical steady-state is reached, in which model quantities such as the rms velocity field are quasi-steady. Perturbations of the true mantle model are then generated in such a way as to reflect the effects of seismic filtering on the structure of the deep Earth. Tomography images differ from each other in part depending on the extent to which horizontal and radial smoothing have been applied (Trampert and Spetzler, 2006). To this end, we mimic radial smoothing by performing a radial averaging of the temperature field of the reference model throughout the mantle, averaging up to depths of 200 km at a time. To mimic horizontal smoothing, we expand the temperature field of the reference case into its spherical harmonic components and truncate at degree 20. This serves to keep the large scale structures, on the order of 1000 km, while discarding the details. In both radial and horizontal smoothing, we do not alter the temperature field of the uppermost 120 km of the reference mantle model corresponding to a boundary layer thickness in our models. Finally, we perform a more realistic comparison with seismic tomography by applying the S20RTS resolution operator (Ritsema et al. 2004; Schuberth et al. 2009b) to modify our reference temperature field. This approach accounts not only for the finite resolution of tomographic models, but also for the effects of heterogeneous data coverage and

damping. We allow the reference and perturbed mantle models (with and without velocity assimilation) to evolve over the course of a vertical transit time (described later, and thereafter referred to simply as transit time) and track their trajectories. To account for uncertainty in rheology and heating modes, we consider several end-members namely: Isoviscous Internal Heating (uniform viscosity, heated entirely from within), Isoviscous Bottom Heating (uniform viscosity, heated purely from the core-mantle boundary (CMB)), Radial Viscosity Internal Heating (increasing viscosity with depth, heated entirely from within) and Radial Viscosity Mixed Heating (increasing viscosity with depth, 10% bottom heating). All model parameters are listed in Table 1.

We solve the forward mantle convection equations that comprise the principles of conservation of mass, momentum and energy. To this end, we model three-dimensional (3-D) time-dependent incompressible mantle convection via the Boussinesq approximation (Chandrasekhar, 1961) and solve the equations using the finite element TERRA code (Bunge et al. 1996, 1997) on a cluster optimized for geophysics-capacity simulations (Oeser et al., 2006). The equations are presented below:

$$\nabla \cdot (\mathbf{v}) = 0 \tag{1}$$

$$\eta(\nabla^2 \mathbf{v}) - \nabla P + \rho g = 0 \tag{2}$$

$$\partial_t T + \mathbf{v} \cdot \nabla T - \kappa \nabla^2 T + H = 0 \tag{3}$$

subject to a set of appropriate boundary and initial conditions. κ, ρ, η, $\mathbf{v}$, P, T, g, t and H denote the thermal diffusivity, density, viscosity, velocity, pressure, temperature, gravitational acceleration, time and internal heat sources, respectively. Note the absence of the inertial term in the momentum equation, reflective of the infinitesimally low Reynolds number (on the order of 10^{-20}) creeping flow of the mantle. Our choice of values for the simulations are presented in Table 1.

Since our mean radial velocities are significantly lower than in the real Earth (Butterworth et al., 2014), we rescale model time to Earth time. For convenience, we express time in terms of a vertical transit time (Bunge et al., 1998), which is the time it takes for material to traverse the mantle depth and is thus a relevant timescale to observe changes in the large scale buoyancy structure of the mantle. It is also the timescale for which a dynamic mantle model completely decorrelates from its initial state. Following Iaffaldano and Bunge (2015), we take a transit time of 150 Myrs for the mantle. We rescale model time to Earth-time based on the radial velocities within the models. To allow for cross-model comparison, all simulations are allowed to run for one transit time at which point they are stopped.

To ensure adequate numerical resolution, the computational domain is discretized with a mesh, derived from the regular icosahedron, with ≈ 80 million finite element grid nodes. For this mesh size, the horizontal grid point resolution is 30 km at the surface and decreases to half that value at the CMB, while the radial grid spacing is 22 km throughout the mantle. All plots of the temperature field show temperatures normalized between 0 (surface temperature) and 1 (CMB temperature). To guarantee that all models have similar convective vigor, we set the CMB temperature of the isoviscous bottom heating case to 4200 K. While this value is high for an incompressible mantle, it represents our approach to achieving a

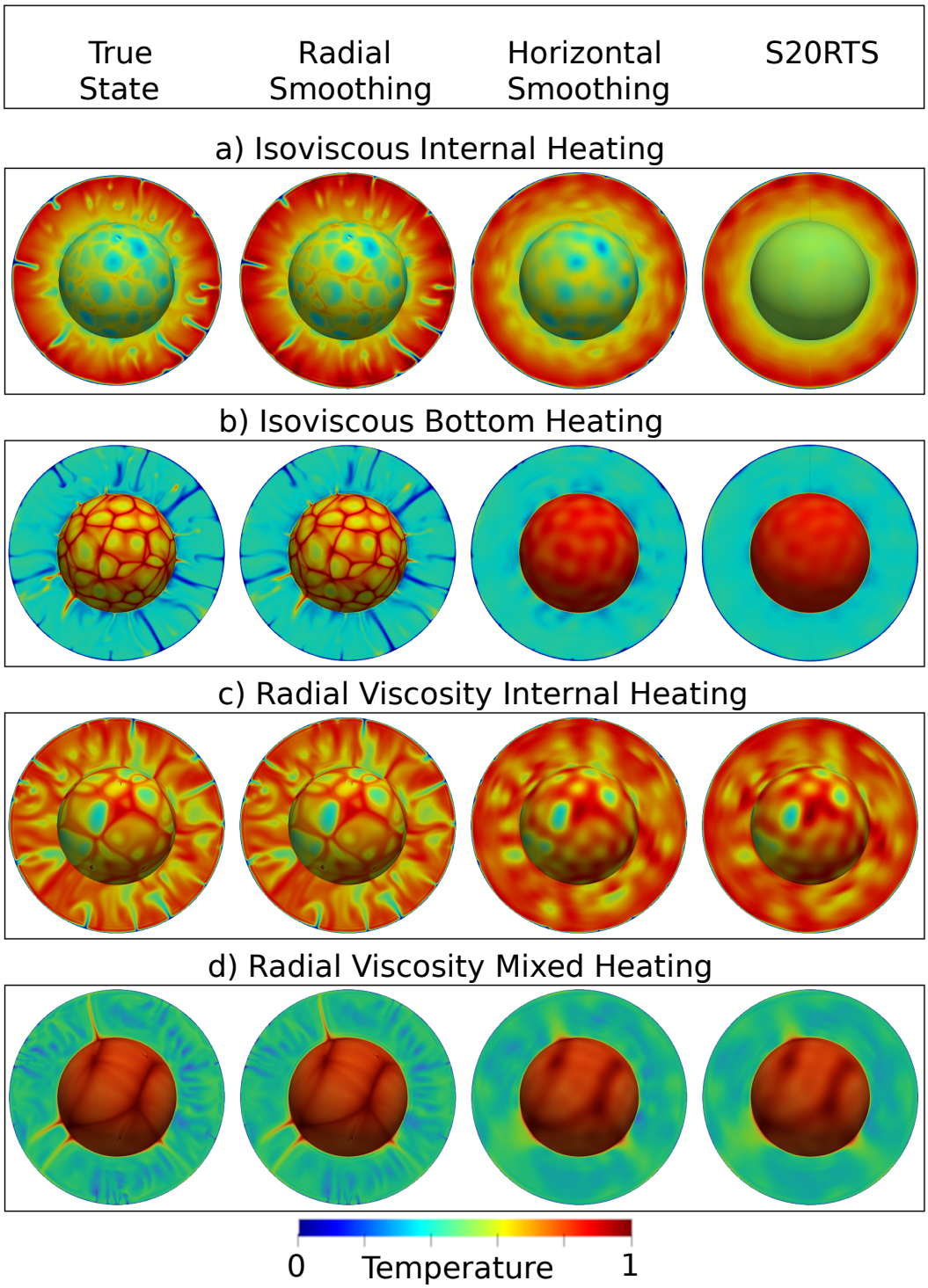

Figure 1: Slices through the 3-D temperature field of four global mantle convection models ((a) Isoviscous, Internal Heating Only; b) Isoviscous, Bottom Heating Only; c) Radial Viscosity Increase, with Internal Heating Only; d) Radial Viscosity Increase, with Mixed Bottom and Internal Heating, see Table 1 for details) that serve as the initial conditions of mantle flow trajectories, where temperatures (blue=cold, red=hot) are normalized to range between 0 (cold) and 1 (hot). Red/blue structures represent upwellings/downwellings. First column: True (Reference) state; Second column: Radial smoothing, obtained by radially averaging the thermal field of the true state over 200 km at each layer; Third column: Horizontal smoothing, obtained via a spherical harmonic expansion of the true state and truncated at degree 20; 4th column: S20RTS filtering, obtained via applying the seismic resolution operator of S20RTS (Ritsema et al. 2004; Schuberth et al. 2009b) to the thermal field of the true state. Note that radial smoothing preserves most of the true state field while horizontal and S20RTS smoothing smear out significant portions of the true state field.

2.3 METHODS 27

Rayleigh number for this class of models that yields a comparable convective vigor to the internal heating models. For the purely internal heating case, we apply a no-heat-flux boundary condition at the CMB.

Fig. 1 shows cross-sections through the initial 3-D temperature fields for all mantle models. Each row represents a different assumed mantle parameterization and the columns show the reference mantle model along with the 3 perturbed models (radial smoothing, horizontal smoothing, S20RTS filtering). In general, the radial smoothing preserves most of the original structure of the true state while horizontal smoothing and S20RTS filtering smear away most of the structure in the true state.

Table 1: Assumed Simulation Parameters for the Mantle Models

Parameter	Value	Units
Density	4500	kgm^{-3}
Outer Core Radius (R_{CMB})	3480	km
Earth Radius (R_{Earth})	6370	km
Gravitational Acceleration	10	ms^{-2}
Thermal Expansivity	2.5×10^{-5}	K^{-1}
Thermal Conductivity	3	$\mathrm{Wm}^{-1}\mathrm{K}^{-1}$
Specific Heat Capacity	1000	$\mathrm{Jkg}^{-1}\mathrm{K}^{-1}$
Surface Temperature	300	K
Internal Heating Rate	2×10^{-12}	Wkg^{-1}
CMB Temperature (pure bottom heating)	4200	K
CMB Temperature (mixed heating)	2300	K
Reference Viscosity (Isoviscous models)	3×10^{22}	Pa s
Reference Viscosity (Layered viscosity models, upper mantle)	3×10^{20}	Pa s
Reference Viscosity (Layered viscosity models, lower mantle)	3×10^{22}	Pa s
Rayleigh Number (Isoviscous Bottom Heating models)	5×10^{6}	
Rayleigh Number (Isoviscous Internal Heating models)	3×10^{7}	
Rayleigh Number (Radial Viscosity models)	5×10^{7}	

2.1 Measures of Model Similarity

2.1.1 Absolute Difference Fields and Histograms

After one transit time, a first-order analysis of the similarities (and differences) between the reference models and their perturbed twins with and without velocity assimilation can be obtained by simply subtracting the temperature values of the perturbed fields from the reference field at every grid point and visualizing this difference field as follows:

Table 2: End-Member Cases and their Properties. For each case, the "X" symbol shows the relevant properties for that model. Cases 1, 2, 3 represent the base cases with varying properties, while case 4 is a combination of the properties of all three base cases.

Case Name	Internal Heating	Bottom Heating	Radial Viscosity
1) Isoviscous Internal Heating	X		
2) Isoviscous Bottom Heating		X	
3) Radial Viscosity Internal Heating	X		X
4) Radial Viscosity Mixed Heating	X	X	X

$$D(\mathbf{x}) = |T(\mathbf{x}) - T_p(\mathbf{x})| \tag{4}$$

where

$D(\mathbf{x})$ is the absolute value of the pointwise difference between reference and perturbed twin,

$T_p(\mathbf{x})$ is the temperature field of the perturbed twin,

$T(\mathbf{x})$ is the temperature field of the reference twin

Such a visualization provides, however, only a qualitative description of the similarities and differences among models. Therefore, we group the difference values obtained via eqn. 4 into bins of equal sizes, compute the frequencies of occurrence for each bin and then plot the results as histograms.

2.1.2 Model Correlations

In the following, we describe a number of statistical measures to compare the twin experiments. We define the spectral power of the temperature field per spherical harmonic degree ℓ as:

$$\sigma_\ell^2 = \sum_{m=0}^{\ell} (a_{\ell m}^2 + b_{\ell m}^2) \tag{5}$$

where $a_{\ell m}$ and $b_{\ell m}$ are the fully normalized (Stacey, 1992) coefficients of the spherical harmonic expansion at degree ℓ and order m.

The rms amplitude is then given by:

$$\sigma_{rms} = \sqrt{\sum_{\ell=1}^{\ell_{max}} \sigma_\ell^2} \tag{6}$$

To evaluate the similarity of reference and perturbed models at every depth, we calculate the correlation between the spherical harmonic expansions of the corresponding temperature fields at every wavelength ℓ up to $\ell = 40$ (Eckhardt, 1984). We calculate the cross-model correlation for every degree as:

$$r^\ell = \frac{\sum_{m=0}^{\ell}(a_{\ell m}c_{\ell m} + b_{\ell m}d_{\ell m})}{\sqrt{\sum_{m=0}^{\ell}(a_{\ell m}^2 + b_{\ell m}^2)}\sqrt{\sum_{m=0}^{\ell}(c_{\ell m}^2 + d_{\ell m}^2)}} \tag{7}$$

where $a_{\ell m}$, $b_{\ell m}$ are the coefficients of the spherical harmonic expansion for the reference field and $c_{\ell m}$, $d_{\ell m}$ are the expansions for the perturbed field.

The total correlation up to $\ell_{max} = 40$ is given by:

$$r_{\ell_{max}}^{tot} = \frac{\sum_{\ell=1}^{\ell_{max}}\sum_{m=0}^{\ell}(a_{\ell m}c_{\ell m} + b_{\ell m}d_{\ell m})}{\sigma_{rms}^{\{a_{\ell m},b_{\ell m}\}}\sigma_{rms}^{\{c_{\ell m},d_{\ell m}\}}} \tag{8}$$

where $\sigma_{rms}^{\{a_{\ell m},b_{\ell m}\}}$ and $\sigma_{rms}^{\{c_{\ell m},d_{\ell m}\}}$ are the rms amplitudes for reference and perturbed models respectively.

2.3 METHODS 29

Equation 8 is applied repeatedly from the beginning of the evolution of the manle flow system up until one transit time.

Proceeding according to Puster et al. (1995), we compute the radial correlation matrix between the lateral structures of the reference model and the perturbed models at any two depths, known as the Two-Point Radial Correlation Function (TPRCF):

$$R(r_1, r_2) = \frac{1}{4\pi\sigma_1(r_1)\sigma_2(r_2)} \int_S \delta T_1(r_1, \Omega)\delta T_2(r_2, \Omega) d\Omega \tag{9}$$

where $\delta T_1(r_1, \Omega)$ and $\delta T_2(r_2, \Omega)$ are the angular temperature deviations of the reference and perturbed fields from their respective horizontal means at radii r_1 and r_2 and $\sigma_1(r_1)$ and $\sigma_2(r_2)$ are the total rms temperature variations of the reference and perturbed fields respectively over the spherical surface S at radii r_1 and r_2.

To serve as basis of comparison for other TPRCF computations, we first compute the TPRCF of the reference model with itself (in which case $T_1 = T_2 = T$, $\delta T_1(r, \Omega) = \delta T_2(r, \Omega) = \delta T(r, \Omega)$). In this case, the TPRCF achieves a maximum value of 1 for equal depths (i.e. on the diagonal, since the field is identical to itself at equal depths) and decreases outwards. We then compute the TPRCF between the reference model and all perturbed models according to equation 9. We superimpose the contour lines of the TPRCF of the reference model on the other TPRCF plots in order to better present the similarities (and differences) between the true states and the (un-)assimilated perturbed states.

2.2 Power Ratio

In the field of meteorology, Surcel et al. (2015) recently introduced the power ratio — a metric for the comparison of an ensemble of precipitation forecasts, but which can equally be applied to our mantle convection problem. It provides a decorrelation scale for model ensembles, which separates the correlated from the uncorrelated scales, and, in essence, is a lengthscale beyond which models become uncorrelated. Given $T_i, T_j, (i, j = 1, ..., N)$ mantle temperature fields and assuming their variance is defined, the following holds:

$$Var\Big(\sum_{i=1}^{N} T_i\Big) = \sum_{i=1}^{N} Var(T_i) + \sum_{i \neq j} Cov(T_i, T_j) \tag{10}$$

where $Var(T_i)$ is the variance for the ith temperature field and $Cov(T_i, T_j)$ are the pairwise covariances. We perform a spherical harmonic expansion of the temperature fields and for each harmonic degree, we compute a variance Var_λ at the lengthscale corresponding to that harmonic degree.

The power ratio for each lengthscale λ is then defined as:

$$R(\lambda) = \frac{\sum_{i=1}^{N} Var(T_i)_\lambda}{Var\Big(\sum_{i=1}^{N} T_i\Big)_\lambda} \tag{11}$$

If the fields are fully decorrelated, it follows that their pairwise covariance $Cov(T_i, T_j) = 0$ for all $i \neq j$.

We therefore have that

$$R(\lambda) = 1 \tag{12}$$

And for perfectly correlated ensembles, we have:

$$R(\lambda) = 1/N \tag{13}$$

For negatively correlated ensembles, the power ratio exceeds 1 and for anti-correlated ensembles, the power ratio is undefined.

2.3 Dynamic Topography

Mantle flow, as expressed here in terms of time-dependent temperature fields, cannot be directly observed, as noted before. Yet, the surface dynamic topography field is, however, an expression of mantle convection. We compute dynamic topography from the propagator matrix technique (Richards and Hager, 1984). The problem is solved via a spherical harmonic expansion of all necessary quantities and the semi-analytical solutions are presented as sensitivity kernels, $K_l(r)$. These kernels can be interpreted as impulse-response functions which relate dynamic topography to a unit density anomaly of given wavelength and depth. Each spherical harmonic coefficient δh_{lm} for surface dynamic topography is computed in the spectral domain by

$$\delta h_{lm} = \int_{R_{CMB}}^{R_{Earth}} \delta\rho_{lm}(r) K_l(r) dr \tag{14}$$

In equation 14, r is the radius, R_{Earth} and R_{CMB} are the radii of the Earth at the surface and the CMB, respectively, and $\delta\rho_{lm}$ is the density anomaly of spherical harmonic degree l, and order m. Following Colli et al. (2018), we disregard all density anomalies shallower than 200 km during the computation of dynamic topography, as they are related to either the thermal cooling of the oceanic lithosphere or compositional heterogeneity of the continental lithosphere (Lithgow-Bertelloni and Silver, 1998). The final dynamic topography values are obtained by a resummation of the spherical harmonic coefficients computed from equation 14 truncated at $\ell_{max} = 20$.

2.4 Taylor Diagram

A commonly employed measure in meteorology and hydrology for comparing multiple predictions of the same observation is the Taylor diagram (Taylor, 2001). It provides a concise way of displaying the degree of correspondence between reference and perturbed fields. The diagram shows the Pearson correlation coefficient (i.e. the covariance between two variables divided by the product of their standard deviations) and centered rms error (i.e. mean-removed rms difference) between the two fields, along with their respective standard deviations all at once. The benefit of plotting all 3 variables on the same figure is seen in the fact that each metric complements the rest. For example, the correlation coefficient provides information about the pattern of variation between the two fields but doesn't offer any information regarding the amplitude of their variations. This second, important, information can be gleaned from the centered rms error. Therefore, in combination, the correlation coefficient and the centered rms error

provide information about pattern and amplitude of variations between two fields but do not provide information on how much variation is due to differences in structure and phase. In combination with the standard deviations of the fields, a summary of the important aspects of the differences between the two fields can thus be obtained. These 3 quantities are related by the following error propagation formula:

$$E^2 = \sigma_r^2 + \sigma_p^2 - 2\sigma_r\sigma_p\rho \tag{15}$$

where ρ and E are the correlation coefficient and centered rms difference between the reference and perturbed fields respectively and σ_r and σ_p are their respective standard deviations. We first obtain spherical harmonic expansions of the fields using SHTOOLS (Wieczorek and Meschede, 2018) after which we calculate correlations and standard deviations according to eqns. 8 and 6 respectively. By comparing with the law of cosines, a geometrical relationship between the four quantities in equation 15 is formed and thus we obtain the Taylor Diagram, which in our case is plotted by adapting code from Copin (2012).

3 RESULTS

3.1 Evolution of Mantle Flow Trajectories across Models

Fig. 2 shows the model states after a transit time. We group the results according to models with and without velocity assimilation. For isoviscous internal heating models (Fig. 2a), the cases without velocity assimilation show a clearly different pattern from the true state. The positions and extents of their downwellings are uncorrelated with those in the true state. With velocity assimilation, however, the models are able to reproduce the dimensions, extents and positions of the downwellings. A visual comparison between panel 2a and the other panels shows that velocity assimilation has the most effect on isoviscous internal heating models. Fig. 2b shows isoviscous bottom heating models. Due to heating from the CMB, these bottom heated models present a lower thermal boundary layer that leads to the generation of plumes that actively ascend through the mantle. As seen from Fig. 2b, the models with no assimilation evolve plumes and downwellings whose behavior is uncorrelated with the true state. The bottom row, on the other hand, more closely resembles the true state and the locations and extents of downwellings are predicted for all cases with a high accuracy. For example, the double downwellings seen on the eastern side of the true state are reproduced to varying degrees by all cases with velocity assimilation (Fig. 2b, lower row) but are completely absent from the models without velocity assimilation (Fig. 2b, upper row). Similarly, the two downwellings as well as the two upwellings adjacent to them in the northern part of the true state are also reproduced by the models with velocity assimilation but are completely absent in the models of the upper row. For the radial viscosity internal heating case with velocity assimilation (Fig. 2c, lower row), the clusters of downwellings in the northern, eastern and western regions of the true state are very well reproduced by the models with velocity asssimilation but are absent in the models without velocity asssimilation. Finally, for the radial viscosity mixed heating case, we observe the evolution shown in Fig. 2d. Due to the very small amount of bottom heating, these models do not develop as many plumes as in the pure bottom heated cases of Fig. 2b. In fact all models develop at most 3 significant plumes in the cross-section shown. Without velocity assimilation, the models again develop structures that are different from the true state. With velocity assimilation, the downwelling patterns are almost exactly like the true state. The plume locations are well replicated but their dimensions differ. For example, the thick

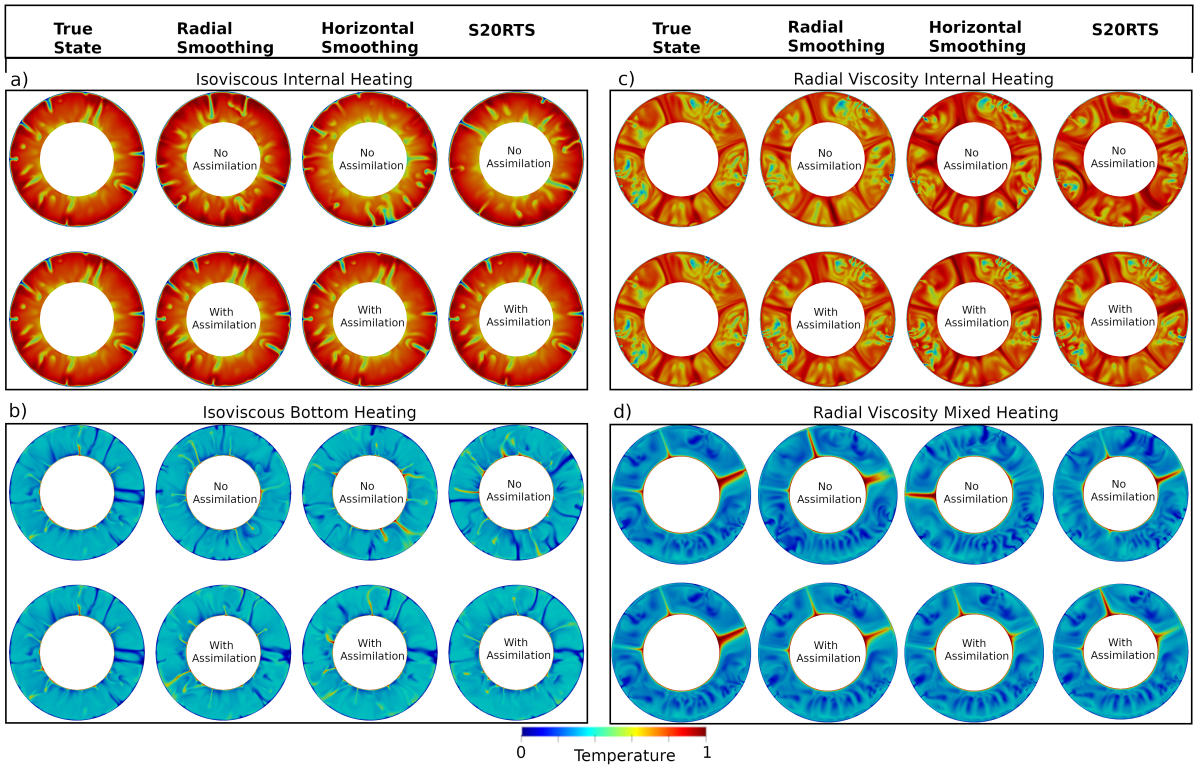

Figure 2: Slices through the 3-D temperature field of four global mantle convection models ((a) Isoviscous, Internal Heating Only; b) Isoviscous, Bottom Heating Only; c) Radial Viscosity Increase, with Internal Heating Only; d) Radial Viscosity Increase, with Mixed Bottom and Internal Heating, see Table 1 for details) after one transit time (see text), where temperatures (blue=cold, red=hot) are normalized to range between 0 (cold) and 1 (hot). Red/blue structures represent upwellings/downwellings. For each panel, the upper/lower row shows the temperature field in the absence/presence of the assimilation of the horizontal component of the surface velocity field of the true state. Note that models with velocity assimilation show up- and downwellings with similar form and location as in the true state while models without velocity assimilation differ significantly from the true state.

plume on the eastern side of the true state appears much thinner in the other 3 models.

3.2 Absolute Difference Fields

Fig. 3 summarizes the results of an absolute grid-point subtraction of the temperature field of the perturbed twins from the reference twin after a transit time. A visual inspection shows that in all cases (with and without velocity assimilation), most of the mantle has a blue color, implying that most temperature differences are close to zero everywhere in the mantle except for the regions that are near the up- and downwellings. For isoviscous internal heating models (Fig. 3a), the cases without velocity assimilation show the largest differences from the true state. These differences are concentrated around the areas with subducting slabs while the rest of the mantle is again close to zero difference. The isoviscous bottom heating models (fig 3b) show differences both in the upper and lower thermal boundary layers close to subducting slabs and upwelling plumes. In the case of radial viscosity internal heating models (Fig. 3c), the differences are again confined majorly to areas close to the subducting slabs. In this case, however, these differences occupy more volume due to the thickness of these slabs. For the radial viscosity mixed heating scenario (Fig. 3d), the thickness of the up- and downwellings means that the differences occupy more volume similar to the case in Fig. 3c. Away from the plumes and subducting material, however, the differences are close to zero. In all model types shown in Fig. 3a, b, c, d, the models with velocity assimilation show more areas close to zero temperature difference than models without velocity assimilation. In general, we also observe that the radial smoothing case has the smallest amount of temperature differences for all models. To aid visualization, we bin the differences from Fig. 3a, b, c, d into histograms as shown in the lower panel of Fig. 3. The isoviscous internal heating case of Fig. 3f shows the largest contrast between models with and without surface velocity assimilation. For this case, over 90% of all grid points for models with velocity assimilation have temperature differences between 0 and 0.04 and the histogram bins rapidly decrease in size, indicating higher similarity with the true state. The models without velocity assimilation, however, have only 50% of grid points with temperature differences between 0 and 0.04. For the isoviscous bottom heating case of Fig. 3g, we observe again that the case with velocity assimilation have around 70% of grid points with temperature differences between 0 and 0.04 while cases without velocity assimilation have around 60% of grid points in this range. Fig. 3h shows the histograms for the radial viscosity internal heating case. For this class of models, the case with velocity assimilation has 80% of all grid points with temperature differences between 0 and 0.04 while the case without velocity assimilation has around 50% of grid points in this range. In the radial viscosity mixed heating case (Fig. 3i), the case with velocity assimilation has 80% of grid points with temperature differences between 0 and 0.04. For the case without velocity assimilation, 60% of grid points have temperature differences between 0 and 0.04.

3.3 Total Correlations

Fig. 4 shows the total correlation between the true state and each one of the perturbed models over a transit time for all cases. At 1/2 of a transit time, the isoviscous internal heating models (Fig. 4a) show correlation values very close to 1 for all cases with velocity assimilation suggesting that assimilation of surface velocities leads to a convergence between the true and perturbed states in less than a transit time. The cases without velocity assimilation, however, already show correlation values close to 0 at 1/2 of a transit time. In the isoviscous bottom heating case of Fig. 4b, the radial smoothing model with velocity

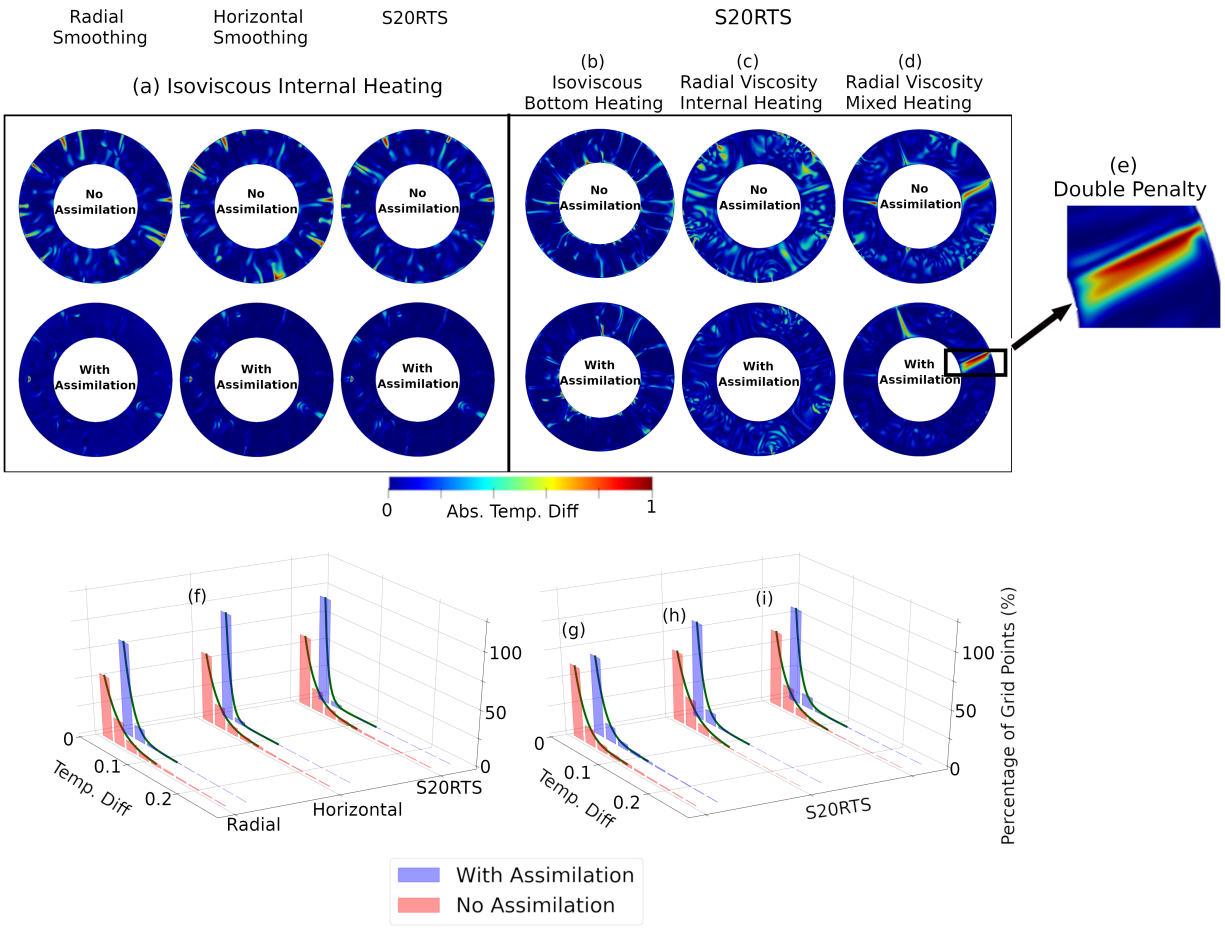

Figure 3: (Top panel) Temperature absolute difference field (true minus perturbed state, see Fig. 2) of four global mantle convection models ((a) Isoviscous, Internal Heating Only; b) Isoviscous, Bottom Heating Only; c) Radial Viscosity Increase, with Internal Heating Only; d) Radial Viscosity Increase, with Mixed Bottom and Internal Heating, see Table 1 for details) after one transit time (see text). The left side of the panel shows the temperature differences for radial, horizontal smoothing as well as the seismic filter of S20RTS for case (a). The right side shows the temperature differences only for S20RTS for cases (b, c, d). Temperature differences are shown as absolute values between 0 and 1. Red/blue structures represent large/small deviations from the true state. The upper/lower row shows the temperature differences in the absence/presence of the assimilation of the horizontal component of the surface velocity field of the true state. Note that models with/without velocity assimilation show lower/higher differences. Also note that across all models, the largest temperature differences are concentrated close to up- and downwellings. Fig. 3e highlights the strong temperature difference close to the plume region, which is a consequence of the double penalty problem (see text). (Bottom panel) 3-D histograms of the absolute grid point temperature differences shown in top panel. Histograms in Fig. 3f, g, h, i correspond to Fig. 3a, b, c, d respectively. Red/blue colors represent models without/with the assimilation of the horizontal component of the surface velocity field of the true state. Note that models with velocity assimilation have longer bars at the 0 temperature difference as well as longer tails compared to models without velocity assimilation, meaning that they have overall lower differences to the true state than models without velocity assimilation.

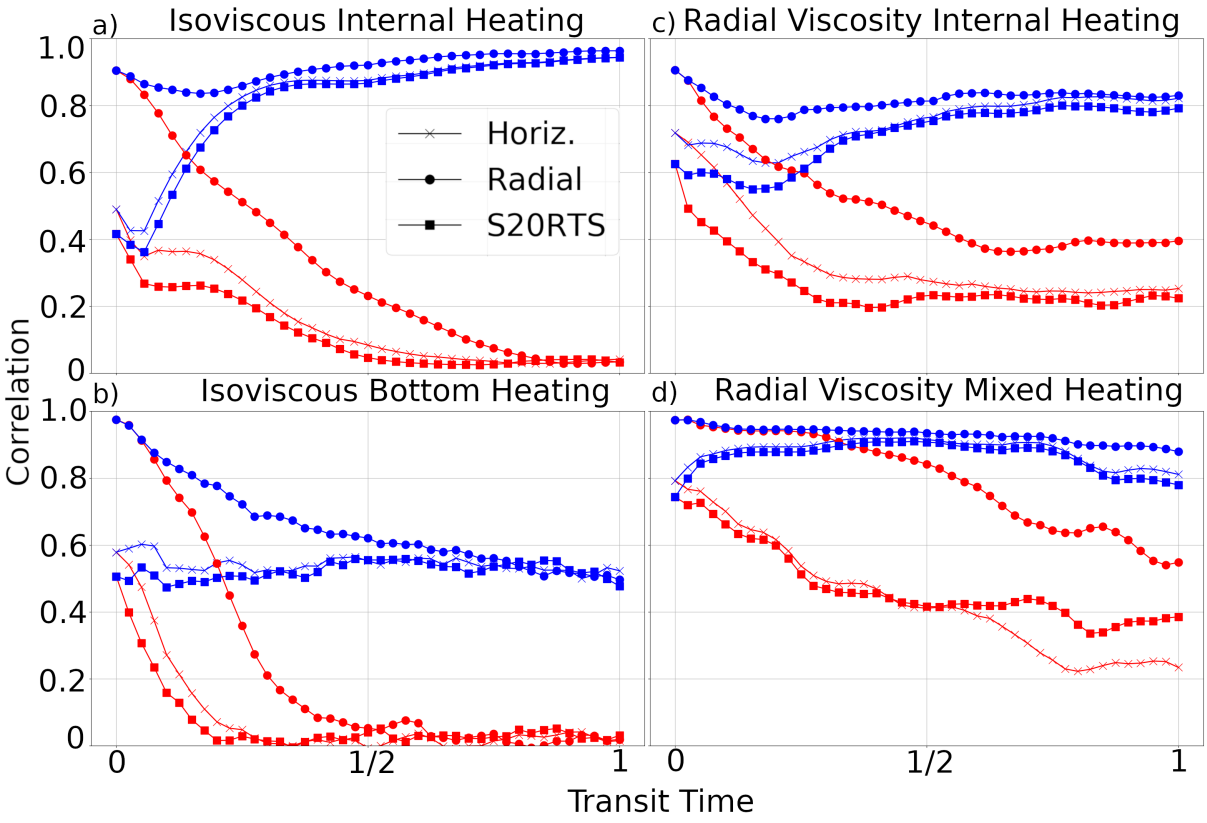

Figure 4: Total correlations of the temperature fields for four models ((a) Isoviscous, Internal Heating Only; b) Isoviscous, Bottom Heating Only; c) Radial Viscosity Increase, with Internal Heating Only; d) Radial Viscosity Increase, with Mixed Bottom and Internal Heating, see Table 1 for details) after one transit time (see text). For every model class, correlations are calculated between the true state and the radial, horizontal and S20RTS smoothings respectively. Red/blue colors represent models without/with the assimilation of the horizontal component of the surface velocity field of the true state. 1/0 represents perfect positive correlation/no correlation. Note that models with velocity assimilation (blue) generally show better correlation over time while models without velocity assimilation (red) show decreasing correlation.

assimilation shows a decrease in correlation values while the horizontal smoothing and S20RTS cases show a roughly constant correlation value and all cases converge to a value of ≈ 0.6 within 1/2 a transit time before finally setling at 0.5 after a full transit time. The models without velocity assimilation, however, are already completely decorrelated from the true state by 1/2 of a transit time. In the radial viscosity internal heating case of Fig. 4c, cases with velocity assimilation show a peak correlation of 0.8 at around 1/2 of a transit time suggesting strong positive correlation. Cases with no velocity assimilation decorrelate from the true state in about 1/4 of a transit time and settle between 0.2 and 0.4 suggesting weak positive correlation. In Fig. 4d, we see for the radial viscosity mixed heating case that the correlation values for models with velocity assimilation saturate at ≈ 0.8 while the models without velocity assimilation decrease in correlation over time. Without velocity assimilation, the radial smoothing case saturates close to 0.6, the S20RTS case to 0.4 and the horizontal smoothing case close to 0.2.

3.4 Two-Point Radial Correlation Functions

The TPRCF of the true state shows a symmetrical pattern with the highest correlations occuring along the diagonal and gradually decreasing outwards. For the models without velocity assimilation in Fig. 5, this symmetrical pattern is absent and there is an observed decorrelation to the true state even at identical depths where a correlation value of 1 is expected. In the isoviscous internal heating case, the models without velocity assimilation (Fig. 5a (i)) are uncorrelated with the true state across all depths and are even negatively correlated at certain depths. With velocity assimilation (Fig. 5a (ii)), however, the radial smoothing, horizontal smoothing and S20RTS models all correlate well with the true state across depth as evidenced by the good fit of the dotted lines in these models. For the bottom heating case without velocity assimilation (Fig. 5b(i)), correlation values everywhere for the S20RTS model are close to zero and at certain depths, this model is even negatively correlated with the true state. With velocity assimilation (Fig. 5b(ii)), the model is only slightly correlated with the true state. In the radial viscosity internal heating as well as radial viscosity mixed heating without velocity assimilation (Figs. 5c(i), d(i)), the S20RTS models show slightly positive correlations to the true state with correlation coefficients between 0.2 and 0.4 even though the contour patterns from the true state are absent. With velocity assimilation (Figs. 5c(ii), d(ii)), however, the contour patterns are more similar to the true state.

3.5 Power Ratio

Fig. 6 shows the power ratio for all models. As noted before, the power ratio takes a value of 1/N for N perfectly correlated fields and a value of 1 for zero correlation. We see that in general, without velocity assimilation, the amount of decorrelation increases with increasing time while for models with assimilation, correlation increases with increasing time. The black circle shows the decorrelation scale after a transit time. In the isoviscous internal heating case (Fig. 6a), the models without assimilation completely decorrelate from the true state around spherical harmonic degree 5. The models with assimilation, however, show very strong correlations with the true state evidenced by their closeness to the solid black line at 0.25 (i.e. 1/N which for 4 fields is $1/4 = 0.25$). In the unassimilated isoviscous bottom heating case (Fig. 6b), the models completely decorrelate already at spherical harmonic degree 1 while the models with velocity assimilation lie much closer to the 0.25 line and show a general increase in decorrelation with decreasing scale. For the radial viscosity internal heating case (Fig. 6c), the unassimilated models completely decorrelate at a wavelength around spherical harmonic degree 28. The assimilated models also

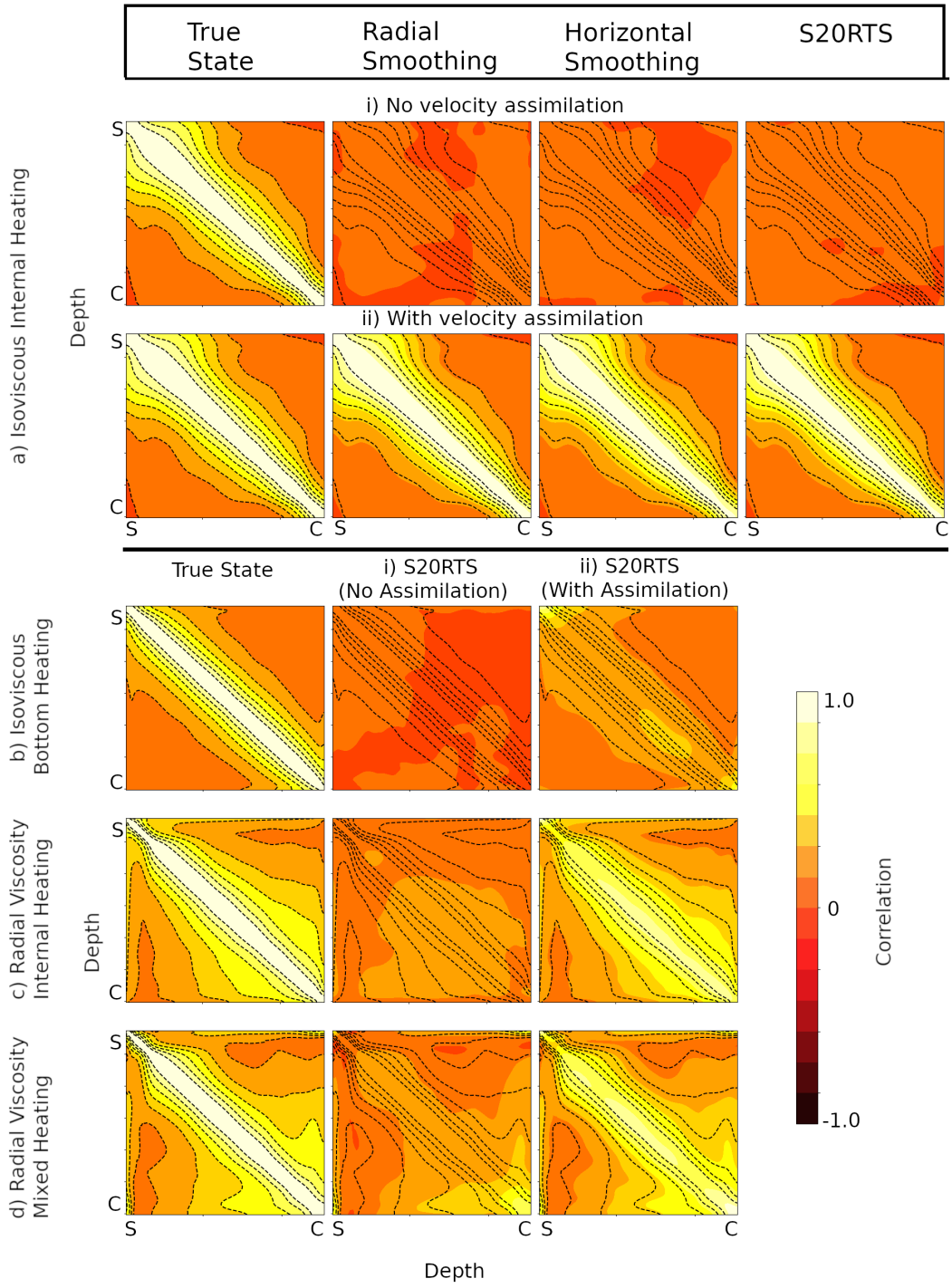

Figure 5: Two-Point Radial Correlation Functions (TPRCF) for four models ((a) Isoviscous, Internal Heating Only; b) Isoviscous, Bottom Heating Only; c) Radial Viscosity Increase, with Internal Heating Only; d) Radial Viscosity Increase, with Mixed Bottom and Internal Heating, see Table 1 for details) after one transit time (see text) with and without assimilation of the horizontal component of the surface velocity field of the true state. The TPRCF is a radial correlation matrix that shows the correlation between any two layers of a mantle model. Dotted black lines show the correlation contours for the true state (first column) superposed on all other plots to aid comparison. Contours decrease in increments of 0.2 away from the axis of symmetry. On the plot, S/C stand for surface/CMB. For the isoviscous internal heating scenario (a), we show TPRCF plots for radial, horizontal smoothing and the seismically filtered S20RTS. For the other scenarios (b, c, d) we show only the case for S20RTS. Note that without/with velocity assimilation, the correlation contours of the true state (dotted black lines) cannot/can be fitted onto the contour patterns of the perturbed states.

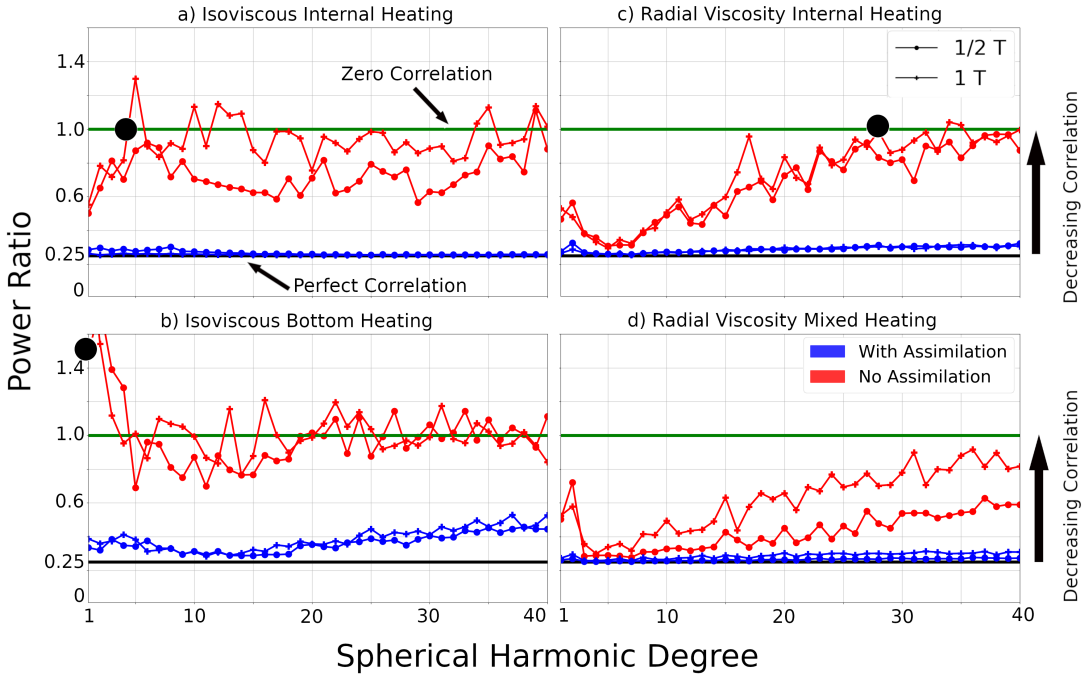

Figure 6: Power Ratio for four models ((a) Isoviscous, Internal Heating Only; b) Isoviscous, Bottom Heating Only; c) Radial Viscosity Increase, with Internal Heating Only; d) Radial Viscosity Increase, with Mixed Bottom and Internal Heating, see Table 1 for details) across different fractions of a transit time, T, shown after one half (1/2 T) and a full transit time (1 T). The vertical axis shows the power ratio, which is a ratio of variances that points to the lengthscales (or spherical harmonic degrees) at which an ensemble of mantle models begin to decorrelate. The exact decorrelation degree after a full transit time is given by the black circle. The horizontal black/green line denotes perfect/zero correlation. The horizontal axis shows the spherical harmonic degree. Models without/with assimilation of the horizontal component of the surface velocity field of the true state are shown in red/blue. Note that models without/with the assimilation of the horizontal component of the surface velocity field of the true state generally approach a power ratio of 1/0.25.

lie close to the 0.25 line and their decorrelation increases slightly with a decrease in scale. For the radial viscosity mixed heating case (Fig. 6d), the models without velocity assimilation never fully completely decorrelate and therefore do not reach the solid green line at 1. There is still, however, an increase in decorrelation with decreasing scale. The models with assimilation lie very close to the perfect correlation line with only a very slight deviation from the line at very small scales.

3.6 Dynamic Topography

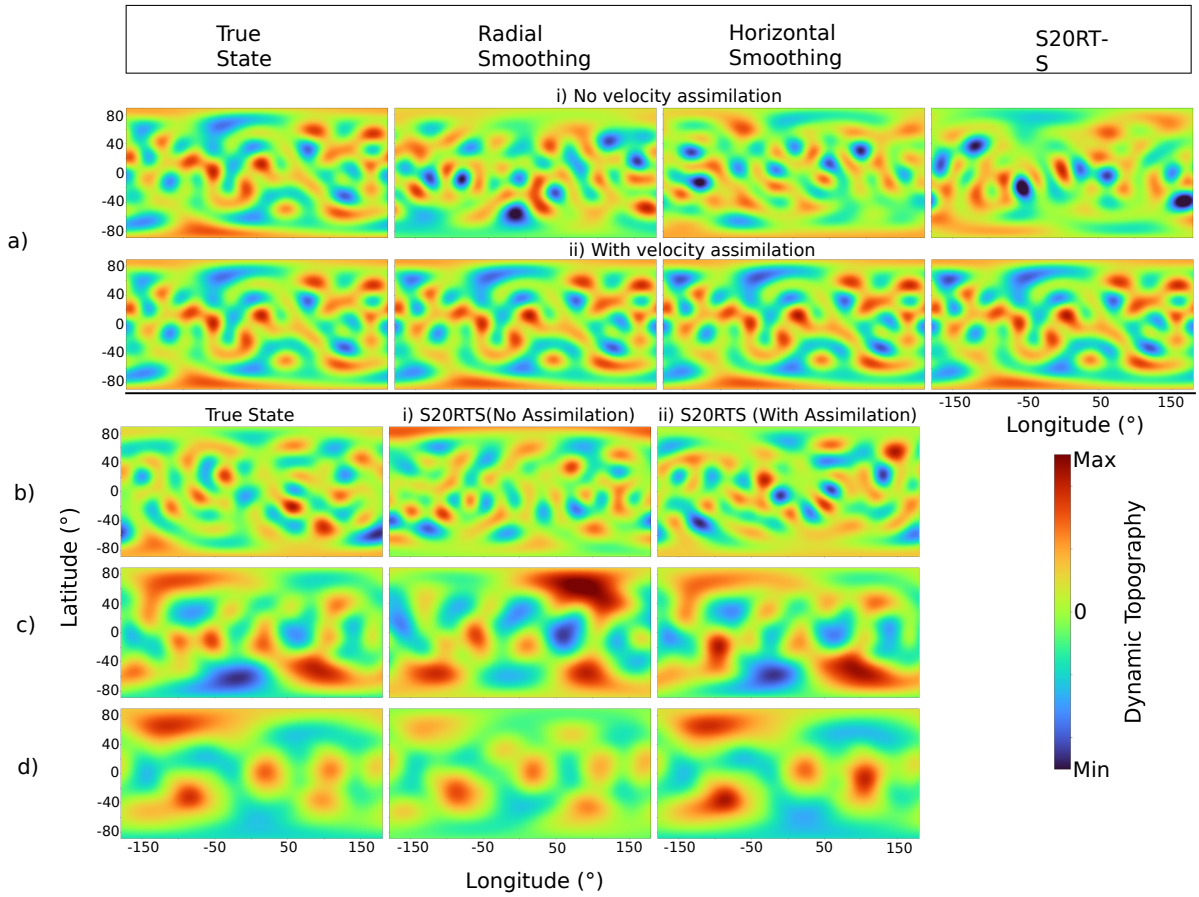

Figure 7: Global dynamic topography maps for four models ((a) Isoviscous, Internal Heating Only; b) Isoviscous, Bottom Heating Only; c) Radial Viscosity Increase, with Internal Heating Only; d) Radial Viscosity Increase, with Mixed Bottom and Internal Heating, see Table 1 for details) after one transit time (see text) with and without the assimilation of the horizontal component of the surface velocity field of the true state. Red/blue colors represent uplift/subsidence. Uplift/subsidence refer to positive/negative dynamic topography. For the isoviscous internal heating scenario (a), we show maps for the cases of radial, horizontal smoothing and the seismically filtered S20RTS. For the other scenarios (b, c, d), we show only maps for S20RTS. Note that without/with velocity assimilation, perturbed models are generally unable/able to reconstruct the uplift and subsidence patterns seen in the true state.

Fig. 7 shows dynamic topography maps for all models after a transit time. In all cases, we observe that in the absence of velocity assimilation, models generally show a poor resemblance to the dynamic topography of the true state. For the no-assimilation isoviscous internal heating case of Fig. 7a(i), the strong dynamic topography high at latitude 0° between longitudes 0° and 50° in the true state is absent in all other cases. In fact, the other cases predict the opposite signal — a dynamic topography low — at the same point. Also the broad dynamic topography low at latitude 80° between longitudes −100°

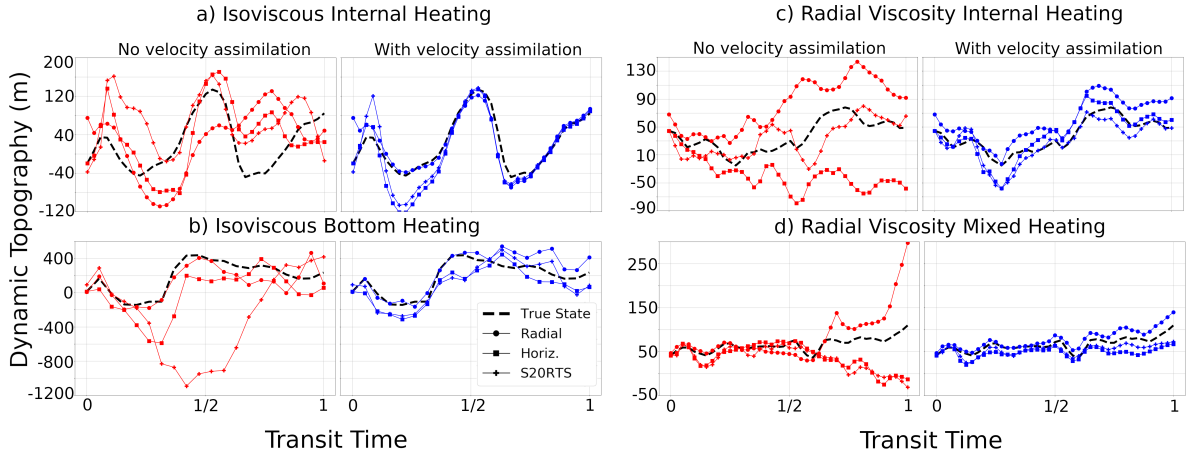

Figure 8: Dynamic topography evolution for a chosen latitude-longitude pair for four models ((a) Isoviscous, Internal Heating Only; b) Isoviscous, Bottom Heating Only; c) Radial Viscosity Increase, with Internal Heating Only; d) Radial Viscosity Increase, with Mixed Bottom and Internal Heating, see Table 1 for details) over one transit time (see text). For all cases, the true state is shown in dotted black lines. Red/blue curves show models without/with assimilation of the horizontal component of the surface velocity field of the true state. Time is given in terms of a transit time, T. Note that by 1/2T, models without/with velocity assimilation already converge/diverge to/from the true state and remain so until a full transit time is reached.

and 50° in the true state are absent in the radial smoothing model, and only very weakly predicted in both horizontal smoothing and S20RTS models. In the isoviscous bottom heating cases with no velocity assimilation (Fig. 7b), we see that the expected dynamic topography low present in the true state at latitude 80° between longitudes −50° and 50° is not correctly predicted by the S20RTS model, which in fact, predicts a dynamic topography high. A similar phenomenon is observed at latitude −80° where a dynamic topography high extending across longitudes −180° and 180° in the true state is not seen in the S20RTS case. In the radial viscosity internal heating case (Figs. 7c), all models show much broader dynamic topography patterns and extend over longer regions than in the isoviscous cases. One notable discrepancy between the true state and the S20RTS model without velocity assimilation can be seen at latitude 80° between longitudes 50° and 150°. In this region, the true state (Fig. 7c) predicts a dynamic topography low, but the S20RTS case predicts a very strong dynamic topography high in that region. The radial viscosity mixed heating cases (Figs. 7d) also show broad patterns similar to the radial viscosity internal heating cases. The true state predicts a strong uplift at latitude 80° between longitudes −150° and −50°. Without velocity assimilation, the S20RTS case shows a much weaker uplift pattern than the true state.

With velocity assimilation, the isoviscous internal heating case (Fig. 7a(ii)), shows the same pattern of dynamic topography highs and lows as in the true state. For example, the dynamic topography low between latitudes 80° and 40° and longitudes −50° and 50° are well reproduced by the radial, horizontal and S20RTS cases. In the isoviscous bottom heating case with velocity assimilation (Fig. 7b(ii)), we see that the strong dynamic topography low at latitude −40° and longitude −150° is reproduced by the S20RTS case. The dynamic topography low present at latitude 80° between longitudes −50° and 50° in the true state is also correctly reproduced by this case. For the radial viscosity internal heating case with velocity assimilation (Fig. 7c(ii)), the S20RTS model also predicts very similar dynamic topography

signals to the true state. For example, the overall dynamic topography pattern of lows and highs observed at between $-40°$ and $-80°$ latitude and between longitudes $-100°$ and $150°$ in the true state are correctly replicated by this model. Finally, in the radial viscosity mixed heating models with velocity assimilation (Fig. 7d(ii)), the dynamic topography high of the true state at latitude $-40°$ and between longitudes $-100°$ and $-50°$ are well reproduced by the S20RTS model.

Fig. 8 shows the evolution of dynamic topography over the entire simulation time for a randomly chosen location. We observe that for all cases, the models with velocity assimilation closely resemble the true state after a transit time. On the other hand, models without velocity assimilation show patterns that are completely uncorrelated with respect to the true state. For example, in the isoviscous internal heating case (Fig. 8a) all models without velocity assimilation predict uplift after 1/2 of a transit time while the true state predicts a subsidence. In Fig. 8b, the S20RTS models of the isoviscous bottom heating case without velocity assimilation show significant subsidence around 1/2 of a transit time while the true state predicts an uplift signal. The radial and horizontal smoothing models perform better in this regard. In the radial viscosity internal heating case (Fig. 8c), after 1/2 of a transit time, the horizontal smoothing models predict subsidence while the true state predicts uplift. For this case, even though the radial smoothing models predict uplift at this time, the signal is much stronger than in the true state. The S20RTS is the best model here with a pattern somewhat following the true state. In the radial viscosity mixed heating case (Fig. 8d), the models without velocity assimilation closely follow the true state until shortly after 1/2 of a transit time after which they all diverge, with the horizontal smoothing model showing the largest divergence after a transit time.

3.7 Taylor Diagram

In the Taylor diagrams of Fig. 9 all models with velocity assimilation lie closer to the reference case than those without assimilation. In the isoviscous internal heating case (Fig. 9a), all models with velocity assimilation have correlation values close to 0.99 and their standard deviations are also close to that of the reference field. Their centered rms differences are also generally less than 20 m. In contrast, the models without velocity assimilation have correlations close to zero and their centered rms errors are more than 5 times higher than the models with velocity assimilation. In the isoviscous bottom heating case (Fig. 9b), all models with velocity assimilation have a correlation of about 0.7 and an centered rms error of about 240 m. For models without velocity assimilation, the horizontal smoothing model has a correlation of 0 and a centered rms error more than 400 m. The radial smoothing and S20RTS cases have correlations of 0.2 and centered rms errors slightly less than 400 m. For the radial viscosity internal heating case (Fig. 9c), the models with velocity assimilation have correlations close to 0.95 and centered rms errors around 30 m. Among the models without velocity assimilation, the radial smoothing model performs better than the others and has a correlation close to 0.9 and a centered rms error close to 40 m. The horizontal smoothing and S20RTS cases have correlations of 0.6 and 0.4 respectively. They also show higher centered rms errors around 75 m and 100 m respectively. With radial viscosity mixed heating cases (Fig. 9d), the models with velocity assimilation are clustered around the $0.95-0.99$ correlation lines and have centered rms error values around 30 m. Among models without velocity assimilation, the radial smoothing model has a correlation around 0.9 and a centered rms error of 60 m. The S20RTS model has

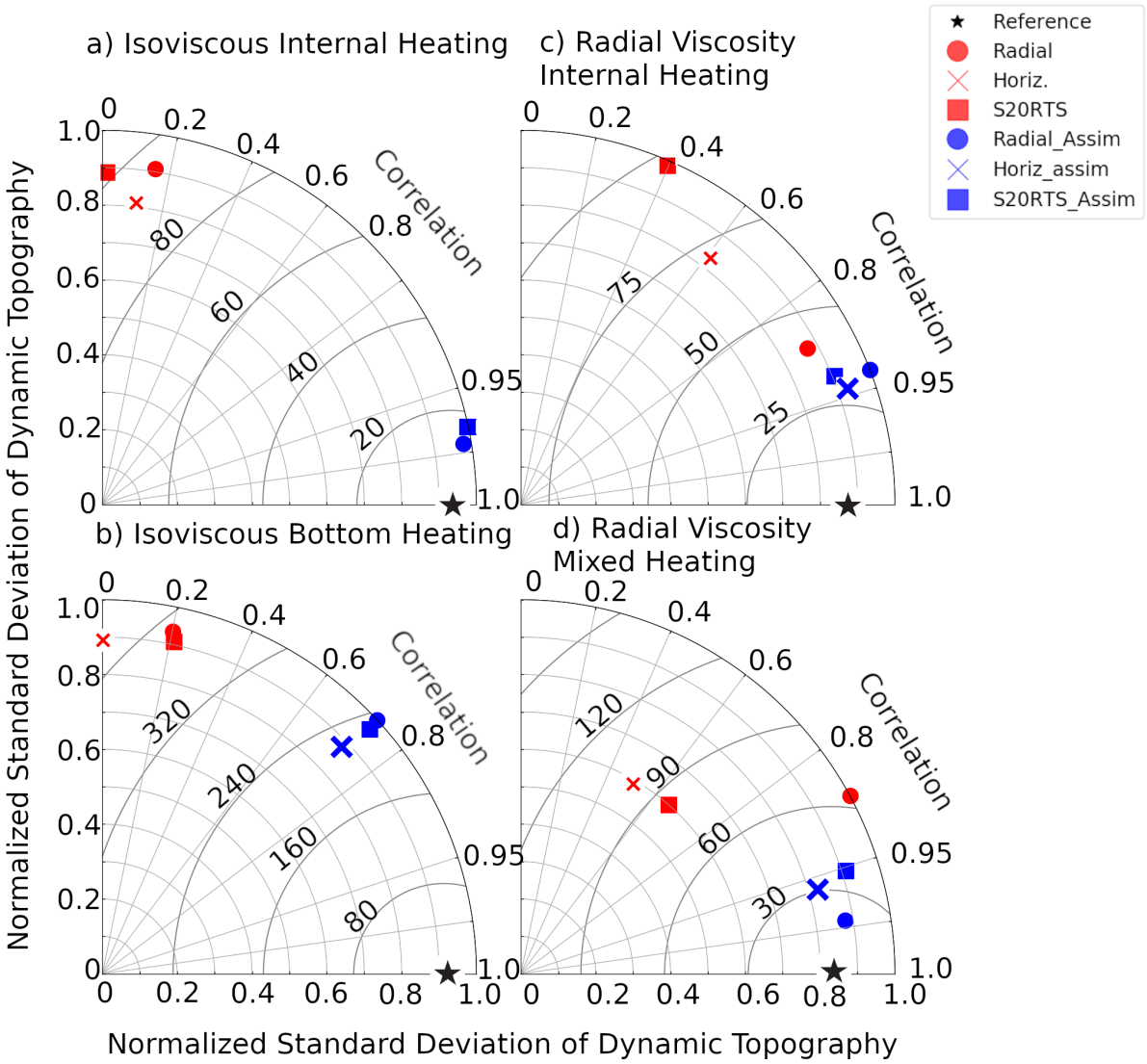

Figure 9: Taylor Diagram showing centered rms errors and Pearson correlations between the true dynamic topography field and the dynamic topography field of perturbed states for four models ((a) Isoviscous, Internal Heating Only; b) Isoviscous, Bottom Heating Only; c) Radial Viscosity Increase, with Internal Heating Only; d) Radial Viscosity Increase, with Mixed Bottom and Internal Heating, see Table 1 for details) after one transit time (see text). It also shows the normalized (with respect to the largest standard deviation of that case) standard deviations for each field. Blue/red icons represent models with/without assimilation of the horizontal component of the surface velocity field of the true state. The reference (true) state is shown as the black star. The centered rms errors (in metres, m) are represented by contours. Correlation lines are drawn in increments of 0.1 except after 0.9 where the last 3 values are 0.95. 0.99 and 1.0. Note that models with velocity assimilation (blue) lie close to the true state (black star) thus depicting similar standard deviations, higher correlations and lower centered rms errors with the true state while models without velocity assimilation (red) lie farther away from the true state.

a correlation around 0.7 and centered rms error slightly less than 90. The horizontal smoothing model has a correlation of 0.5 and a centered rms error of about 100 m.

4 DISCUSSION

Creating trajectories of mantle flow and linking the present-day mantle state with its past states is crucial for testing geodynamic models against observations. In principle, methods for linking mantle states are available. One such method for constructing trajectories is the adjoint optimization approach (Bunge et al. 2003; Ismail-Zadeh et al. 2004; Horbach et al. 2014; Ghelichkhan and Bunge 2016; Price and Davies 2017) which seeks to reduce the misfit between the model-generated final state temperature and the reference temperature field representative of the current mantle state. However, the presence of the butterfly effect raises the question: can a reliable trajectory be created? Several studies (Colli et al. 2015; Vynnytska and Bunge 2015; Colli et al. 2018; Bocher et al. 2015, 2018) have shown that this is possible if one assimilates the horizontal component of the surface velocity field. Here, using forward simulations, we revisit this problem with the aid of simple end-member models and apply more realistic model perturbations rather than pointwise errors, where random perturbations of the initial temperature field, uniformly distributed in space, are performed, as in previous work.

4.1 Convective Vigor at High Rayleigh Numbers

We note that while the mantle has a high Rayleigh number, it is difficult to accurately infer this from surface symptoms, such as plate velocities, in particular due to poorly known plate boundary forces. For example, the South American plate slowed down in speed by about 30% in the Miocene. This velocity change is commonly attributed to the rise of Altiplano, unrelated to the convective vigor of the mantle (Iaffaldano et al., 2006).

The high Rayleigh number of the mantle, in turn, makes it possible to understand mantle convection in terms of boundary layer behaviour (Turcotte and Oxburgh 1967; Davies 1999). At high Rayleigh numbers, plumes and slabs are typically thin and occupy a small portion of the volume. Therefore away from up- and downwellings, the rest of the model volume is near mean temperature. This implies that for models with different initial conditions, the heterogeneity difference away from up- and downwellings is close to zero. Our results in this study confirm this and we observe that across all models (with and without velocity assimilation), the differences between the true state and perturbed models are around 0 (blue colors) everywhere in the mantle except in the areas close to subduction or plume activity (Fig. 3e). This phenomenon is referred to as the double penalty problem. Double penalty arises when two models make similar predictions about an observable, but the location of the observable in one model is slightly offset from that in the other model. This then results in large differences and rms errors in the region where the model predictions do not overlap. This also explains why for every class of models in our experiments, those with velocity assimilation saturate to roughly the same high correlation value while those without velocity assimilation incur larger errors close to up- and downwellings. As pointed out by Colli et al. (2015), once initial condition perturbations are propagated within a mantle model and memory of the initial state is lost, perturbed mantle models are merely a different expression of the underlying physical system of the true state and are thus statistically similar.

4.2 Performance of End-Member Models

We have used a combination of different end-member models to account for various model parameterizations (i.e. viscosity, heating mode). The heat budget of the mantle is dominated by internal heating (from the decay of radioactive nuclides), secular cooling (which, for our present discussion, is analogous to an additional volumetric heat source) and heating from the bottom by the core. However, the relative magnitude of internal heating versus bottom heating remains under investigation (Lay et al. 2008; Bellini et al. 2022). The viscosity profile of the mantle is also under debate. Estimates of mantle viscosity have been previously obtained via inversions of postglacial rebound observations (Haskell 1935; Mitrovica 1996; Cathles 1975; Kaufmann and Lambeck 2002) as well as via the long-wavelength anomalies of the geoid (Ricard et al. 1984; Richards and Hager 1984; Hager and Richards 1989). Satellite observations of secular changes in the gravity field coupled with measurements of sea level changes have also been used recently to infer mantle viscosity (Paulson et al., 2007). All these studies have inferred an increase in viscosity with mantle depth. Recently, Colli et al. (2018) and Ghelichkhan et al. (2021) tested the impact of various viscosity profiles on the reconstruction of mantle thermal structure.

In this study, we selected three end-member models summarized in Table 2. The most realistic model — radial viscosity mixed heating — is then a combination of all three end-members. In all our experiments, the isoviscous internal heating case, which represents the base scenario, provided the best results for velocity assimilation. This class of models has a very simple thermal profile with only an upper thermal boundary layer, a flow pattern dominated by active downwellings (Bunge et al., 1997) and structures rising and sinking at relatively uniform velocity. The absence of a lower thermal boundary layer in this class of models means that there are no actively rising plumes whose locations would be unconstrained because, by nature of the geophysical problem, velocity assimilation cannot happen at the CMB. These properties ensure that as soon as the exact positions of downwellings are constrained by the assimilated surface velocity field, the information is propagated uniformly within the mantle and the perturbed systems quickly converge to the true state as seen in the final flow fields (Fig. 2a) and the difference fields/histograms (Figs. 3a, f). This class of models also achieves maximum corrrelation very quickly (by 1/2 of a transit time) with the true state if velocity assimilation is done (Fig. 4a) and also quickly decorrelates (again by 1/2 of a transit time) from the true state in the absence of velocity assimilation.

In the isoviscous purely bottom heated case, which represents another end member, a second thermal boundary layer forms around the CMB in addition to the thermal boundary layer at the surface. This implies that a number of upwelling plumes are generated at the lower boundary layer and the flow pattern is a complex interaction between the sinking and rising structures (Houseman 1988; Bercovici et al. 1992). Since the surface velocity field is assimilated only at the upper thermal boundary layer, we inherently leave the lower thermal boundary layer unconstrained and free to evolve in response to the downwellings. The impact is a tendency for this class of models to converge more slowly and less completely to the true state as seen in Figs. 2b and 3b, g. These models decorrelate quickly (by 1/2 of a transit time) from the reference model in the absence of velocity assimilation (Fig. 4b) and with velocity assimilation the correlation settles at half the value of their isoviscous internal heating counterparts.

Models with radial viscosity increase develop very large-scale structures (Bunge et al., 1996). It is these large-scale structures that are readily influenced by velocity assimilation, leaving out the small scales. We observed that after a transit time, the extent and shapes of the downwellings in the true state were recovered in the perturbed models with assimilation, as seen in Figs. 2c and 3c, h while models without velocity assimilation diverged from the true state.

The radial viscosity mixed heating case is perhaps the most realistic of all cases considered and as mentioned previously, is a combination of the model parameterizations of the previous 3 cases. In this class of models, the plumes are stably anchored in the lower mantle due to the increase in viscosity, reminiscent of the hotspot reference frame (Duncan and Richards, 1991). This explains why the model correlations, even without velocity assimilation (Fig. 4d), remain higher than the isoviscous bottom heating case (where plumes move readily, see Fig. 4b) and the radial viscosity internal heating case (where there are no plumes at all, see Fig. 4c).

4.3 Seismic Resolution

Accurately linking the present-day state of the mantle with its past states and constructing trajectories depends on our ability to image the state of the interior of the Earth via seismic tomography. This is, however, not a trivial problem. Limited data coverage available for seismic studies makes tomographic inverse problems ill-posed. In solving these linearized ill-posed inverse problems, as is done in seismic tomography, the regularization parameter (λ) controls the balance between minimising residual data misfit and model norm. However, due to our poor knowledge of data uncertainties, the choice of values for the regularization parameter is unknown to a certain extent. Tomographers typically consider two regularization approaches: radial smoothing and horizontal smoothing. The former is typically implemented in seismic tomography as λ times an operator which describes a radial derivative while the latter is implemented as λ times an operator describing a horizontal gradient on the sphere (Trampert and Spetzler, 2006). In essence, the tomographic image is a filtered version of the real Earth interior. In our work, we considered two smoothing approaches as well as a tomographic filtering. We chose to implement radial smoothing as a radial averaging of the mantle temperature field and horizontal smoothing as a spherical harmonic expansion and truncation of the mantle temperature field. Both implementations serve as simple analogues to the actual tomographic smoothing process. We also implemented a more realistic representation of the seismic filtering process via the resolution operator of S20RTS (Ritsema et al. 2004; Schuberth et al. 2009a). Recently, other resolution operators have also been introduced (Zaroli 2016; Zaroli et al. 2017; Koelemeijer et al. 2018; Freissler et al. 2020; Simmons et al. 2019). In all experiments, the radial smoothing case introduced the lowest amount of initial discrepancy as evidenced by the very high starting correlations (Fig. 4). This is an expected consequence of the boundary layer nature of mantle convection resulting in radial sinking and rising of structures. In contrast the horizontal smoothing and S20RTS cases start off poorly correlated with the true state. This is because both smoothing types act across instead of along, the original ascending and descending structures. After a transit time, we find that regardless of the type of smoothing performed, all twin experiments diverge without velocity assimilation and converge with velocity assimilation. In the difference fields (upper panel of Fig. 3), we see large differences in radial, horizontal and S20RTS smoothings without velocity assimilation and much

smaller differences with velocity assimilation. This observation is reiterated in the histograms (lower panel of Fig. 3) where cases without velocity assimilation have shorter histogram bars at the 0 temperature difference compared to the cases with velocity assimilation. All correlation plots, regardless of smoothing type, show increasing/constant (decreasing) correlation over time with (without) velocity assimilation as evidenced from Fig. 4.

4.4 TPRCF

The TPRCF computations shown here were performed in line with Puster et al. (1995) but with slight differences. While they compute the TPRCF as an autocorrelation function of a model with itself at every depth, we first compute the TPRCF of the true state with itself and then compute the TPRCFs of the true state with the perturbed states. The logic is that if velocity assimilation drives the trajectory of the perturbed model back toward the true state, then after a period of assimilation, the perturbed system should resemble the true state enough so that the TPRCF of the true state with itself is similar to the TPRCF of the true state with the perturbed state. We find from Fig. 5 that this is the case for all models with velocity assimilation and that for models with no velocity assimilation, the mantle layers in the true state are completely uncorrelated with those of the perturbed states. In the isoviscous internal heating case with velocity assimilation (Fig. 5a(ii)), there is extremely high correlation between the true states and other models. This is expected since both the total correlation plots and power ratio for this class of models already show extremely high correlations with velocity assimilation. For the isoviscous bottom heating models, the somewhat poor correlation observed in Fig. 4b despite velocity assimilation are again obvious in the TPRCF plots (Fig. 5b(ii)) which is because the lower thermal boundary layer is unconstrained and allowed to evolve freely. For both the radial viscosity internal heating as well as mixed heating cases, the TPRCF patterns align closely with the true state in the presence of velocity assimilation (Figs. 5c(ii), d(ii)). The TPRCF is a measure of radial mass flux. These mass fluxes and their associated radial stresses are a driving force for the uplift and subsidence patterns in the form of dynamic topography observed on Earth's surface. As such, models with a TPRCF contour pattern similar to the true state are also expected to produce a similar global dynamic topography pattern and vice-versa.

4.5 Links to Dynamic Topography

All measures considered so far assess model performance in terms of the heterogeneity throughout the volume. However, the actual heterogeneity structure of the mantle in past times is, in practice, not accessible. In essence, trajectories for the real Earth can only express themselves through surface geological information. The consequences of mantle convection on the geological record have become much clearer in recent years. It is thus necessary to focus on linking geodynamic models with geological observations. One such observation is the uplift and subsidence pattern of the Earth, away from its isostatically compensated state and referred to as dynamic topography (Hager et al., 1985).

There are various ways of comparing numerical predictions of dynamic topography as has been demonstrated in this work. Evolution plots (Fig. 8), which show how dynamic topography at a given location evolves over time, provide a first-order visualization of the similarities and differences across various geodynamic models. However, it is not succinct enough, as one would have to make several thousand of

such plots to cover every location on Earth. Other alternatives for comparing dynamic topography maps include histograms of point-wise differences between any two model predictions of dynamic topography as well as spherical harmonic correlations. Such histograms provide a summary of the distribution of model differences across an entire map, albeit at a single time. One would therefore have to make histogram plots for every time period, which can be cumbersome. On the other hand, spherical harmonic correlations can be useful in providing information about model similarity across lengthscales, and one readily sees the exact scales at which model-predicted dynamic topography maps become more or less similar. All of these grid-point methods have the advantage that they are quite straightforward to implement and often provide a single number as an output. However, each approach measures model properties in isolation and their results cannot be readily interpreted together. To overcome these limitations, several model comparison methods have been developed in neighbouring disciplines. One such method is the Taylor diagram (Fig. 9) which simultaneously displays correlation, centered rms error and standard deviations in a single plot. In essence, the Taylor diagram has the advantage of showing amplitude and phase information all at once. Since its introduction (Taylor, 2001), it has been used extensively in meteorology (e.g. Pierce et al. 2009; Helmert and Hellmuth 2001; Achberger et al. 2003), hydrology/soil science (e.g. Maurer et al. 2002; Challinor et al. 2004) as well as oceanography (e.g. Gnanadesikan et al. 2004; Bingham and Haines 2004). Most meteorological and oceanographic applications of the Taylor diagram have focused on small, regional domains, where the assumption of a flat Earth is reasonable. As such, their computations of correlations and standard deviations follow the standard approach used in statistics. For global fields, however, the flat Earth assumption is inaccurate. Close to the equator, lines of longitude are further apart and at the poles lines of longitude are much closer to each other. To account for this in the Taylor diagram, we computed correlations and standard deviations via a spherical harmonic expansion of the dynamic topography fields. We learn from the Taylor diagram (Fig. 9) that the dynamic topography predictions of assimilated models correlate well with the true state and also have low centered rms errors compared to predictions of unassimilated models. In addition, their standard deviations are very similar to those of the true state. On the other hand, dynamic topography predictions for models without velocity assimilation poorly correlate, have higher centered rms errors and much different standard deviations compared to the true state. Thus, the Taylor diagram is a highly succinct way of summarizing the much better performance of models with velocity assimilation compared to models without velocity assimilation. In addition, it paves the way for much more sophisticated metrics that overcome the limitations of common grid-point measures.

The need to shift away from traditional grid-point metrics is also motivated by the so-called double penalty problem, well known in the meteorological community (e.g. Anthes 1983; Mass et al. 2002): a forecast of an observable (e.g. precipitation) that is correct in terms of intensity, size, and timing, but incorrect concerning location, results in very large rms errors and poor correlations. It is unrealistic for model forecasts to exactly match the observations one-to-one and thus metrics that reward models for making correct predictions in terms of intensity, shape and timing, even if location differences exist, should be adopted in the study of dynamic topography. It is also important to be able to identify coherent, contiguous uplift and subsidence areas on dynamic topography maps and compare such identified areas with respect to location, amplitude and volume. As such, object identification as well as image processing tech-

niques are an attractive tool for studying dynamic topography as well as other geological observations. Meteorologists have already applied several of these techniques to study precipitation patterns, cyclones and storms (Ebert and McBride 2000; Davis et al. 2006a,b, 2009) representable on 2-D latitude-longitude grids and a summary is provided by Gilleland et al. (2009).

4.6 Model Limitations

It is important to address the limitations of our study. Firstly, we assume an incompressible mantle where there are no radial density variations from the surface to the CMB. However, compressibility is significant in mantle convection as density increases with mantle depth (Dziewonski and Anderson, 1981). In a compressible mantle, the flow slows down with depth but has faster velocities close to the surface in comparison to an incompressible mantle (Bunge et al., 1997). This is necessary in order to maintain constant mass flux (Panasyuk et al., 1996). As such, a density anomaly in the lower mantle will generate less viscous stresses and make a lower contribution to dynamic topography while a density anomaly close to the surface would make a higher contribution to dynamic topography in comparison to an incompressible mantle. A second limitation is that the Rayleigh numbers based on internal heating (on the order of 10^7) used in this study are below Earth-like values. As such, we had to rescale model time to Earth time via the transit time. A lower Rayleigh number implies a reduction in the overall vigor of convection and results in volumetrically larger thermal boundary layers in comparison to a high Rayleigh number flow. Thus at higher Rayleigh number, the smaller bouyancies would result in a lower amplitude of dynamic topography when compared to a low Rayleigh number convective flow. Thirdly, our assumptions for mantle rheology are very simple and the temperature-dependence of mantle viscosity is ignored. Coltice and Shephard (2017) showed that tectonic predictions of mantle convection models for periods over 10Myrs are highly sensitive to assumed rheological parameters even though the latter are not well known. Bello et al. (2015) further showed that a temperature-dependent mantle viscosity profile enhances vertical and lateral coherence of slabs. Vertical and lateral coherence would presumably enhance transfer of information from assimilated surface velocity field to the depth of the mantle. Fourthly, all our calculations assume no error in the assimilated surface velocity field. In reality, our knowledge of actual past plate motions has a level of uncertainty associated with it. This is particularly evident in regions completely surrounded by subduction zones (Wu et al., 2016) although developments in slab unfolding techniques may help alleviate this problem (Wu and Suppe, 2017). The work of Iaffaldano et al. (2012) also shows that it is possible to reduce finite-rotation noise and improve the temporal resolution of plate motions via a hierarchical Bayesian framework. The choice of an appropriate reference frame is another source of uncertainty in past plate motion models (Shephard et al., 2012) and should be accounted for in order to extend retrodiction times. With respect to tomographic filtering of geodynamic models, an important aspect is the source location of actual earthquakes. These locations are obviously tied to source-receiver distributions which, in the real Earth, are different than in our models. Also, since we do not assimilate actual plate velocity information, our surface velocity fields do not account for continents and slabs. We note that future experiments should be done with assimilation of plate-like surface velocities. Finally, we assume perfect knowledge of the dynamic topography and its evolution in time. While there are improvements in linking past dynamic topography to mantle convection models (Müller et al., 2018), further work is needed in constraining the amplitude, areal extent and temporal change of dynamic topography.

5 CONCLUSION

Constructing robust time trajectories of mantle flow and linking them to surface observables is crucial to properly constrain poorly known mantle parameters. However, the butterfly effect seemingly constitutes a hindrance. In this work, we have shown the results of an ensemble of model calculations aimed at understanding how the effects of assimilating the horizontal component of the surface velocity field strongly minimize the butterfly effect. Through the introduction of tomographically relevant perturbations combined with different model parameterizations, we followed the trajectories of several end-member mantle convection models and found that the assimilation of surface velocities seems to be crucial in limiting the butterfly effect and enabling the construction of reliable trajectories. In particular, we have assessed the quality of model trajectories through the use of their predicted dynamic topography as a proxy, because this constitutes a crucial geological observable. This focus on dynamic topography, which, in essence, is a 2-D field, allows us to use the Taylor diagram - a metric from atmospheric and oceanic sciences – to evaluate model performance. Further, object-based metrics, which assess spatial patterns of 2-D fields, could be adopted for future use.

6 ACKNOWLEDGMENTS

We acknowledge the support and funding provided by the Deutscher Akademischer Austausch Dienst(DAAD) as well as the Deutsche Forschungsgemeinschaft (DFG) under project nos. 412338397, 202416587 (TETHYS-2G) as well as 233171740 (Mass Storage System). We are also grateful to Mario Parente (Jülich Center for Neutron Science) and George Craig (Meteorological Institute Munich) for their fruitful discussions. Numerical simulations were undertaken on the TETHYS-2G machine at LMU Munich, Germany. Many thanks to Jens Oeser for excellent maintenance of the machine.

7 DATA AVAILABILITY

The 2-D and 3-D rendering of the temperature field visualizations are done in Paraview software (Ahrens et al., 2005). For formatting of the figures and other type of visualizations, we have used Matplotlib (Hunter, 2007). All the data and softwares in this study are properly referenced. Model results can be made available upon request.

8 Collaborator Contribution

1. H.-P. Bunge supervised the research and corrected the manuscript
2. B.S.A. Schuberth provided help with seismic filtering
3. L. Colli supported with dynamic topography calculations
4. B. Vilacis supported with verification of dynamic topography results

References

Achberger, C., Linderson, M.-L., and Chen, D. (2003). Performance of the Rossby Centre regional atmospheric model in Southern Sweden: comparison of simulated and observed precipitation. *Theoretical and Applied Climatology*, 76(3):219–234.

Ahrens, J., Geveci, B., and Law, C. (2005). 36 - paraview: An end-user tool for large-data visualization. In Hansen, C. D. and Johnson, C. R., editors, *Visualization Handbook*, page 717–731. Butterworth-Heinemann, Burlington.

Anthes, R. A. (1983). Regional Models of the Atmosphere in Middle Latitudes. *Monthly Weather Review*, (6):1306–1335.

Bauer, S., Bunge, H.-P., Drzisga, D., Ghelichkhan, S., Huber, M., Kohl, N., Mohr, M., Rüde, U., Thönnes, D., and Wohlmuth, B. (2020). In *Software for Exascale Computing - SPPEXA 2016-2019*, Cham.

Becker, T. W. and Boschi, L. (2002). A comparison of tomographic and geodynamic mantle models. *Geochemistry, Geophysics, Geosystems*, 3(1).

Bellini, G., Inoue, K., Mantovani, F., Serafini, A., Strati, V., and Watanabe, H. (2022). Geoneutrinos and geoscience: an intriguing joint-venture. *Nuovo Cimento Rivista Serie*, 45(1):1–105.

Bello, L., Coltice, N., Rolf, T., and Tackley, P. J. (2014). On the predictability limit of convection models of the Earth's mantle. *Geochem. Geophys. Geosyst.*, (15).

Bello, L., Coltice, N., Tackley, P. J., Dietmar Müller, R., and Cannon, J. (2015). Assessing the role of slab rheology in coupled plate-mantle convection models. *Earth and Planetary Science Letters*, 430:191–201.

Bercovici, D., Schubert, G., and Glatzmaier, G. A. (1992). Three-dimensional convection of an infinite-Prandtl-number compressible fluid in a basally heated spherical shell. *Journal of Fluid Mechanics*, 239:683–719.

Bingham, R. and Haines, K. (2004). Mean dynamic topography: Inter-comparisons and errors. *European Space Agency,(Special Publication) ESA SP*, (569):231–236.

Bocher, M., Coltice, N., Fournier, A., and Tackley, P. (2015). A sequential data assimilation approach for the joint reconstruction of mantle convection and surface tectonics. *Geophysical Journal International*, 204:200–214.

Bocher, M., Fournier, A., and Coltice, N. (2018). Ensemble Kalman filter for the reconstruction of the Earth's mantle circulation. *Nonlinear Processes in Geophysics*, (1):99–123.

Braun, J. (2010). The many surface expressions of mantle dynamics. *Nature Geoscience*, 3(12):825–833.

Bunge, H.-P. and Glasmacher, U. A. (2018). Models and observations of vertical motion (MoveOn) associated with rifting to passive margins: Preface. *Gondwana Research*, 53:1–8. Rifting to Passive Margins.

Bunge, H.-P., Hagelberg, C. R., and Travis, B. J. (2003). Mantle circulation models with variational data assimilation: inferring past mantle flow and structure from plate motion histories and seismic tomography. *Geophysical Journal International*, 152(2):280–301.

Bunge, H.-P., Richards, M. A., and Baumgardner, J. R. (1996). Effect of depth-dependent viscosity on the planform of mantle convection. *Nature*, 379(6564):436–438.

Bunge, H.-P., Richards, M. A., and Baumgardner, J. R. (1997). A sensitivity study of three-dimensional spherical mantle convection at 108 Rayleigh number: Effects of depth-dependent viscosity, heating mode, and an endothermic phase change. *Journal of Geophysical Research: Solid Earth*, 102(B6):11991–12007.

Bunge, H.-P., Richards, M. A., Lithgow-Bertelloni, C., Baumgardner, J. R., Grand, S. P., and Romanowicz, B. A. (1998). Time Scales and Heterogeneous Structure in Geodynamic Earth Models. *Science*, 280(5360):91–95.

Burstedde, C., Stadler, G., Alisic, L., Wilcox, L. C., Tan, E., Gurnis, M., and Ghattas, O. (2013). Large-scale adaptive mantle convection simulation. *Geophysical Journal International*, 192(3):889–906.

Butterworth, N. P., Talsma, A. S., Müller, R. D., Seton, M., Bunge, H. P., Schuberth, B. S. A., Shephard, G. E., and Heine, C. (2014). Geological, tomographic, kinematic and geodynamic constraints on the dynamics of sinking slabs. *Journal of Geodynamics*, 73:1–13.

Carena, S., Bunge, H.-P., and Friedrich, A. M. (2019). Analysis of geological hiatus surfaces across Africa in the Cenozoic and implications for the timescales of convectively-maintained topography. *Canadian Journal of Earth Sciences*, 56(12):1333–1346.

Cathles, L. M. (1975). *The viscosity of the earth's mantle [by] Lawrence M. Cathles, III.* Princeton University Press Princeton.

2.9 REFERENCES 51

Challinor, A., Wheeler, T., Craufurd, P., Slingo, J., and Grimes, D. (2004). Design and optimisation of a large-area process-based model for annual crops. *Agricultural and forest meteorology*, 124(1-2):99–120.

Chandrasekhar, S. (1961). *Hydrodynamic and hydromagnetic stability.*

Chust, T. C., Steinle-Neumann, G., Dolejš, D., Schuberth, B. S. A., and Bunge, H.-P. (2017). MMA-EoS: A Computational Framework for Mineralogical Thermodynamics. *Journal of Geophysical Research: Solid Earth*, 122(12):9881–9920.

Colli, L., Bunge, H.-P., and Schuberth, B. S. A. (2015). On retrodictions of global mantle flow with assimilated surface velocities. *Geophys. Res. Lett.*, 42.

Colli, L., Ghelichkhan, S., and Bunge, H.-P. (2016). On the ratio of dynamic topography and gravity anomalies in a dynamic Earth. *Geophysical Research Letters*, 43(6):2510–2516.

Colli, L., Ghelichkhan, S., Bunge, H.-P., and Oeser, J. (2018). Retrodictions of Mid Paleogene mantle flow and dynamic topography in the Atlantic region from compressible high resolution adjoint mantle convection models: Sensitivity to deep mantle viscosity and tomographic input model. *Gondwana Research*, pages 252–272. Rifting to Passive Margins.

Coltice, N., Gérault, M., and Ulvrová, M. (2017). A mantle convection perspective on global tectonics. *Earth Science Reviews*, 165:120–150.

Coltice, N. and Shephard, G. E. (2017). Tectonic predictions with mantle convection models. *Geophysical Journal International*, 213(1):16–29.

Copin, Y. (2012). Taylor diagram for python/matplotlib.

Czarnota, K., Hoggard, M. J., White, N., and Winterbourne, J. (2013). Spatial and temporal patterns of Cenozoic dynamic topography around Australia. *Geochemistry, Geophysics, Geosystems*, 14(3):634–658.

Davies, D. R., Goes, S., Davies, J., Schuberth, B., Bunge, H.-P., and Ritsema, J. (2012). Reconciling dynamic and seismic models of Earth's lower mantle: The dominant role of thermal heterogeneity. *Earth and Planetary Science Letters*, 353-354:253–269.

Davies, D. R., Valentine, A. P., Kramer, S. C., Rawlinson, N., Hoggard, M. J., Eakin, C. M., and Wilson, C. R. (2019). Earth's multi-scale topographic response to global mantle flow. *Nature Geoscience*, 12.

Davies, G. F. (1999). *Dynamic Earth: Plates, Plumes and Mantle Convection.* Cambridge University Press.

Davis, C., Brown, B., and Bullock, R. (2006a). Object-Based Verification of Precipitation Forecasts. Part I: Methodology and Application to Mesoscale Rain Areas. *Monthly Weather Review*, 134(7):1772.

Davis, C., Brown, B., and Bullock, R. (2006b). Object-Based Verification of Precipitation Forecasts. Part II: Application to Convective Rain Systems. *Monthly Weather Review*, 134(7):1785.

Davis, C. A., Brown, B. G., Bullock, R., and Halley-Gotway, J. (2009). The Method for Object-Based Diagnostic Evaluation (MODE) Applied to Numerical Forecasts from the 2005 NSSL/SPC Spring Program. *Weather and Forecasting*, 24(5):1252.

DiCaprio, L., Gurnis, M., and Müller, R. D. (2009). Long-wavelength tilting of the Australian continent since the Late Cretaceous. *Earth and Planetary Science Letters*, 278(3):175–185.

Duncan, R. A. and Richards, M. A. (1991). Hotspots, mantle plumes, flood basalts, and true polar wander. *Reviews of Geophysics*, 29(1):31–50.

Dziewonski, A. M. and Anderson, D. L. (1981). Preliminary reference Earth model. *Physics of the Earth and Planetary Interiors*, 25(4):297–356.

Ebert, E. E. and McBride, J. L. (2000). Verification of precipitation in weather systems: determination of systematic errors. *Journal of Hydrology*, 239(1):179–202.

Eckhardt, D. H. (1984). Correlations between global features of terrestrial fields. *Journal of the International Association for Mathematical Geology*, (2).

Ehlers, T. A. and Farley, K. A. (2003). Apatite (U–Th)/He thermochronometry: methods and applications to

problems in tectonic and surface processes. *Earth and Planetary Science Letters*, 206(1):1–14.

Fernandes, V. M. and Roberts, G. G. (2020). Cretaceous to Recent net continental uplift from paleobiological data: Insights into sub-plate support. *GSA Bulletin*, 133(5-6):1217–1236.

Freissler, R., Zaroli, C., Lambotte, S., and Schuberth, B. (2020). Tomographic filtering via the generalized inverse: A way to account for seismic data uncertainty. *Geophys. J. Int.*, 223(1):254–269.

French, S. W. and Romanowicz, B. A. (2014). Whole-mantle radially anisotropic shear velocity structure from spectral-element waveform tomography. *Geophysical Journal International*, 199(3):1303–1327.

Friedrich, A. M., Bunge, H.-P., Rieger, S. M., Colli, L., Ghelichkhan, S., and Nerlich, R. (2018). Stratigraphic framework for the plume mode of mantle convection and the analysis of interregional unconformities on geological maps. *Gondwana Research*, pages 159–188. Rifting to Passive Margins.

Ghelichkhan, S. and Bunge, H.-P. (2016). The compressible adjoint equations in geodynamics: derivation and numerical assessment. *International Journal on Geomathematics (GEM)*.

Ghelichkhan, S., Bunge, H.-P., and Oeser, J. (2021). Global mantle flow retrodictions for the early Cenozoic using an adjoint method: evolving dynamic topographies, deep mantle structures, flow trajectories and sublithospheric stresses. *Geophysical Journal International*, 226(2):1432–1460.

Ghosh, A., Becker, T. W., and Zhong, S. J. (2010). Effects of lateral viscosity variations on the geoid. , 37(1):L01301.

Gilleland, E., Ahijevych, D., Brown, B. G., Casati, B., and Ebert, E. E. (2009). Intercomparison of spatial forecast verification methods. *Weather and Forecasting*, 24(5):1416–1430.

Gnanadesikan, A., Dunne, J. P., Key, R. M., Matsumoto, K., Sarmiento, J. L., Slater, R. D., and Swathi, P. (2004). Oceanic ventilation and biogeochemical cycling: Understanding the physical mechanisms that produce realistic distributions of tracers and productivity. *Global Biogeochemical Cycles*, 18(4).

Guillocheau, F., Rouby, D., Robin, C., Helm, C., Rolland, N., Le Carlier de Veslud, C., and Braun, J. (2012). Quantification and causes of the terrigeneous sediment budget at the scale of a continental margin: a new method applied to the Namibia–South Africa margin. *Basin Research*, 24(1):3–30.

Guillocheau, F., Simon, B., Baby, G., Bessin, P., Robin, C., and Dauteuil, O. (2018). Planation surfaces as a record of mantle dynamics: The case example of Africa. *Gondwana Research*, 53:82–98. Rifting to Passive Margins.

Hager, B. H., Clayton, R. W., Richards, M. A., Comer, R. P., and Dziewonski, A. M. (1985). Lower mantle heterogeneity, dynamic topography and the geoid. *Nature*, 313.

Hager, B. H. and Richards, M. A. (1989). Long-wavelength variations in Earth’s geoid: physical models and dynamical implications. *Philosophical Transactions of the Royal Society of London. Series A, Mathematical and Physical Sciences*, 328(1599):309–327.

Hartley, R. A., Roberts, G. G., White, N., and Richardson, C. (2011). Transient convective uplift of an ancient buried landscape. *Nature Geoscience*, 4.

Haskell, N. A. (1935). The Motion of a Viscous Fluid Under a Surface Load. *Physics*, 6(8):265–269.

Hayek, J. N., Vilacís, B., Bunge, H.-P., Friedrich, A. M., Carena, S., and Vibe, Y. (2021). Correction: Continent-scale hiatus maps for the atlantic realm and australia since the upper jurassic and links to mantle flow-induced dynamic topography. *Proc. R. Soc. A*, 477(2251):20210437.

Hayek, N., Vilacis, B., Bunge, H.-P., Friedrich, A., Carena, S., and Vibe, Y. (2020). Continent-scale Hiatus Maps for the Atlantic Realm and Australia since the Upper Jurassic and links to mantle flow induced dynamic topography. *Proc. R. Soc. A*.

Heister, T., Dannberg, J., Gassmöller, R., and Bangerth, W. (2017). High accuracy mantle convection simulation through modern numerical methods – II: realistic models and problems. *Geophysical Journal International*, 210(2):833–851.

Helmert, J. and Hellmuth, O. (2001). On the impact of turbulence length-scales, derived from large-eddy simulations on predicted mesoscale fields using the "Lokal-Modell". *Biennial Report 2001 & 2002*, page 24.

Hoggard, M. J., White, N., and Al-Attar, D. (2016). Global dynamic topography observations reveal limited influence of large-scale mantle flow. *Nature Geoscience*, 9.

Hoggard, M. J., Winterbourne, J., Czarnota, K., and White, N. (2017). Oceanic residual depth measurements, the plate cooling model, and global dynamic topography. *Journal of Geophysical Research: Solid Earth*, 122(3):2328–2372.

Holdt, M. C., White, N. J., Stephenson, S. N., and Conway-Jones, B. W. (2022). Densely sampled global dynamic topographic observations and their significance. *Journal of Geophysical Research: Solid Earth*, 127(7):e2022JB024391. e2022JB024391 2022JB024391.

Horbach, A., Bunge, H.-P., and Oeser, J. (2014). The adjoint method in geodynamics: derivation from a general operator formulation and application to the initial condition problem in a high resolution mantle circulation model. *GEM - International Journal on Geomathematics*, 5(2):163–194.

Houseman, G. (1988). The dependence of convection planform on mode of heating. *Nature*, 332:346–349.

Hulot, G., Lhuillier, F., and Aubert, J. (2010). Earth's dynamo limit of predictability. *Geophysical Research Letters*, 37(6).

Hunter, J. D. (2007). Matplotlib: A 2d graphics environment. *Computing in Science & Engineering*, 9(3):90–95.

Iaffaldano, G., Bodin, T., and Sambridge, M. (2012). Reconstructing plate-motion changes in the presence of finite-rotations noise. *Nature Communications*, 3:1048.

Iaffaldano, G. and Bunge, H.-P. (2015). Rapid plate motion variations through geological time: Observations serving geodynamic interpretation. *Annual Review of Earth and Planetary Sciences*, 43(1):571–592.

Iaffaldano, G., Bunge, H.-P., and Dixon, T. H. (2006). Feedback between mountain belt growth and plate convergence. *Geology*, 34(10):893.

Ismail-Zadeh, A., Schubert, G., Tsepelev, I., and Korotkii, A. (2004). Inverse problem of thermal convection: numerical approach and application to mantle plume restoration. *Physics of the Earth and Planetary Interiors*, 145(1):99–114.

Japsen, P. (2018). Sonic velocity of chalk, sandstone and marine shale controlled by effective stress: Velocity-depth anomalies as a proxy for vertical movements. *Gondwana Research*, 53:145–158. Rifting to Passive Margins.

Kaufmann, G. and Lambeck, K. (2002). Glacial isostatic adjustment and the radial viscosity profile from inverse modeling. *Journal of Geophysical Research: Solid Earth*, 107(B11):ETG 5–1–ETG 5–15.

Keil, C. and Craig, G. (2007). A displacement-based error measure applied in a regional ensemble forecasting system. *Monthly Weather Review*, 135:3248–3259.

Keil, C. and Craig, G. (2009). A displacement and amplitude score employing an optical flow technique. *Weather and Forecasting*, 24:1297–1308.

King, L. C. (1955). Pediplanation and Isostasy: An Example from South Africa. *Quarterly Journal of the Geological Society*, 111(1-4):353–359.

Koelemeijer, P., Schuberth, B. S. A., Davies, D. R., Deuss, A., and Ritsema, J. (2018). Constraints on the presence of post-perovskite in Earth's lowermost mantle from tomographic-geodynamic model comparisons. *Earth and Planetary Science Letters*, 494:226–238.

Kohn, M. J. and Dettman, D. L. (2018). *5. Paleoaltimetry from Stable Isotope Compositions of Fossils*, pages 119–154. De Gruyter.

Kronbichler, M., Heister, T., and Bangerth, W. (2012). High accuracy mantle convection simulation through modern numerical methods. *Geophysical Journal International*, 191(1):12–29.

Lay, T., Hernlund, J., and Buffett, B. A. (2008). Core–mantle boundary heat flow. *Nature Geoscience*, 1.

Lithgow-Bertelloni, C. and Silver, P. G. (1998). Dynamic topography, plate driving forces and the African superswell. *Nature*, 395:269–272.

Liu, L. and Gurnis, M. (2008). Simultaneous inversion of mantle properties and initial conditions using an adjoint

of mantle convection. *Journal of Geophysical Research: Solid Earth*, 113(B8).

Lorenz, E. N. (1963). Deterministic Nonperiodic Flow. *Journal of Atmospheric Sciences*, (2):130–141.

Lorenz, E. N. (1965). A study of the predictability of a 28-variable atmospheric model. *Tellus*, 17(3):321–333.

Marzban, C. and Sandgathe, S. (2010). Optical flow for verification. *Weather and Forecasting*, 25(5):1479 – 1494.

Mass, C. F., Ovens, D., Westrick, K., and Colle, B. A. (2002). DOES INCREASING HORIZONTAL RESOLUTION PRODUCE MORE SKILLFUL FORECASTS?: The Results of Two Years of Real-Time Numerical Weather Prediction over the Pacific Northwest. *Bulletin of the American Meteorological Society*, 83(3):407–430.

Matthews, K. J., Hale, A. J., Gurnis, M., Müller, R. D., and DiCaprio, L. (2011). Dynamic subsidence of Eastern Australia during the Cretaceous. *Gondwana Research*, 19(2):372–383.

Maurer, E. P., Wood, A. W., Adam, J. C., Lettenmaier, D. P., and Nijssen, B. (2002). A long-term hydrologically based dataset of land surface fluxes and states for the conterminous United States. *Journal of climate*, 15(22):3237–3251.

McNamara, A. K. and Zhong, S. (2005). Thermochemical structures beneath Africa and the Pacific Ocean. *Nature*, 437.

Meinhold, G. (2010). Rutile and its applications in earth sciences. *Earth-Science Reviews*, 102(1):1–28.

Mitrovica, J. X. (1996). Haskell [1935] revisited. *Journal of Geophysical Research: Solid Earth*, 101(B1):555–569.

Müller, R., Hassan, R., Gurnis, M., Flament, N., and Williams, S. (2018). Dynamic topography of passive continental margins and their hinterlands since the cretaceous. *Gondwana Research*, 53:225–251. Rifting to Passive Margins.

Müller, R. D., Seton, M., Zahirovic, S., Williams, S. E., Matthews, K. J., Wright, N. M., Shephard, G. E., Maloney, K. T., Barnett-Moore, N., Hosseinpour, M., Bower, D. J., and Cannon, J. (2016). Ocean Basin Evolution and Global-Scale Plate Reorganization Events Since Pangea Breakup. *Annual Review of Earth and Planetary Sciences*, 44(1):107–138.

Nikolaevsky, V. N. (1969). Statistical Continuum Theories. By MARK J. BERAN. Interscience, 1968. 424 pp. *Journal of Fluid Mechanics*, 38(4):859–860.

Nolet, G. (1987). Seismic tomography with applications in global seismology and exploration geophysics.

Oeser, J., Bunge, H.-P., and Mohr, M. (2006). Cluster Design in the Earth Sciences Tethys. In Gerndt, M. and Kranzlmüller, D., editors, *High Performance Computing and Communications*, pages 31–40, Berlin, Heidelberg. Springer Berlin Heidelberg.

Panasyuk, S. V., Hager, B. H., and Forte, A. M. (1996). Understanding the effects of mantle compressibility on geoid kernels. *Geophysical Journal International*, 124(1):121–133.

Paulson, A., Zhong, S., and Wahr, J. (2007). FAST TRACK PAPER: Inference of mantle viscosity from GRACE and relative sea level data. *Geophysical Journal International*, 171(2):497–508.

Pekeris, C. L. (1935). Thermal Convection in the Interior of the Earth. *Geophysical Supplements to the Monthly Notices of the Royal Astronomical Society*, 3:343–367.

Piazzoni, A. S., Steinle-Neumann, G., Bunge, H.-P., and Dolejs, D. (2007). A mineralogical model for density and elasticity of the Earth's mantle. *Geochemistry, Geophysics, Geosystems*, 8(11).

Pierce, D. W., Barnett, T. P., Santer, B. D., and Gleckler, P. J. (2009). Selecting global climate models for regional climate change studies. *Proceedings of the National Academy of Sciences*, 106(21):8441–8446.

Price, M. G. and Davies, J. H. (2017). Profiling the robustness, efficiency and limits of the forward-adjoint method for 3-D mantle convection modelling. *Geophysical Journal International*, 212(2):1450–1462.

Puster, P., Jordan, T. H., and Hager, B. H. (1995). Characterization of mantle convection experiments using two-point correlation functions. *Journal of Geophysical Research: Solid Earth*, (B4):6351–6365.

Ricard, Y., Fleitout, L., and Froidevaux, C. (1984). Geoid heights and lithospheric stresses for a dynamic Earth. *Annales Geophysicae*, 2:267–285.

Richards, F. D., Hoggard, M. J., and White, N. J. (2016). Cenozoic epeirogeny of the Indian peninsula. *Geochem-*

istry, Geophysics, Geosystems, 17(12):4920–4954.

Richards, M. A. and Hager, B. H. (1984). Geoid anomalies in a dynamic Earth. *Journal of Geophysical Research: Solid Earth*, 89(B7):5987–6002.

Ritsema, J., A. Deuss, H. v. H., and Woodhouse, J. (2011). S40RTS: a degree-40 shear-velocity model for the mantle from new Rayleigh wave dispersion, teleseismic traveltime and normal-mode splitting function measurements. *Geophysical Journal International*, 184:1223–1236.

Ritsema, J., van Heijst, H. J., and Woodhouse, J. H. (2004). Global transition zone tomography. *Journal of Geophysical Research: Solid Earth*, 109(B2).

Roberts, G. G. and White, N. (2010). Estimating uplift rate histories from river profiles using African examples. *Journal of Geophysical Research: Solid Earth*, 115(B2).

Roebber, P. J. (2009). Visualizing Multiple Measures of Forecast Quality. *Weather and Forecasting*, (2):601–608.

Said, A., Moder, C., Clark, S., and Abdelmalak, M. M. (2015a). Sedimentary budgets of the Tanzania coastal basin and implications for uplift history of the East African rift system. *Journal of African Earth Sciences*, 111:288–295.

Said, A., Moder, C., Clark, S., and Ghorbal, B. (2015b). Cretaceous–Cenozoic sedimentary budgets of the Southern Mozambique Basin: Implications for uplift history of the South African Plateau. *Journal of African Earth Sciences*, 109:1–10.

Schuberth, B. S. A., Bunge, H.-P., and Ritsema, J. (2009a). Tomographic filtering of high-resolution mantle circulation models: Can seismic heterogeneity be explained by temperature alone? *Geochemistry, Geophysics, Geosystems*, (5).

Schuberth, B. S. A., Bunge, H.-P., Steinle-Neumann, G., Moder, C., and Oeser, J. (2009b). Thermal versus elastic heterogeneity in high-resolution mantle circulation models with pyrolite composition: High plume excess temperatures in the lowermost mantle. *Geochemistry, Geophysics, Geosystems*, 10(1).

Şengör, A. M. C. (2001). Elevation as indicator of mantle-plume activity. In *Mantle plumes: their identification through time*. Geological Society of America.

Shephard, G., Bunge, H.-P., Schuberth, B., Müller, R., Talsma, A., Moder, C., and Landgrebe, T. (2012). Testing absolute plate reference frames and the implications for the generation of geodynamic mantle heterogeneity structure. *Earth and Planetary Science Letters*, 317-318:204–217.

Simmons, N., Forte, A., and Grand, S. (2007). Thermochemical structure and dynamics of the african superplume. *Geophys. Res. Lett*, 34(2).

Simmons, N. A., Forte, A. M., and Grand, S. P. (2009). Joint seismic, geodynamic and mineral physical constraints on three-dimensional mantle heterogeneity: Implications for the relative importance of thermal versus compositional heterogeneity. *Geophysical Journal International*, 177(3):1284–1304.

Simmons, N. A., Schuberth, B. S. A., Myers, S. C., and Knapp, D. R. (2019). Resolution and Covariance of the LLNL-G3D-JPS Global Seismic Tomography Model: Applications to Travel time Uncertainty and Tomographic Filtering of Geodynamic Models. *Geophysical Journal International*, 217(3):1543–1557.

Stacey, F. D. (1992). *Physics of the Earth.*

Steinberger, B. and O'Connell, R. (1997). Changes of the Earth's rotation axis owing to advection of mantle density heterogeneities. *Nature*, 387:169–173.

Stephenson, S. N., White, N. J., Li, T., and Robinson, L. F. (2019). Disentangling interglacial sea level and global dynamic topography: Analysis of Madagascar. *Earth and Planetary Science Letters*, 519:61–69.

Stewart, C. A. and Turcotte, D. L. (1989). The route to chaos in thermal convection at infinite Prandtl number: 1. Some trajectories and bifurcations. *Journal of Geophysical Research: Solid Earth*, 94(B10):13707–13717.

Stixrude, L. and Lithgow-Bertelloni, C. (2011). Thermodynamics of mantle minerals - II. Phase equilibria. *Geophysical Journal International*, 184(3):1180–1213.

Surcel, M., Zawadzki, I., and Yau, M. K. (2015). A Study on the Scale Dependence of the Predictability of Precipitation Patterns. *Journal of the Atmospheric Sciences*, 72(1):216–235.

Taylor, K. E. (2001). Summarizing multiple aspects of model performance in a single diagram. *Journal of Geophysical Research: Atmospheres*, 106(D7):7183–7192.

Trampert, J., Deschamps, F., Resovsky, J., and Yuen, D. (2004). Probabilistic Tomography Maps Chemical Heterogeneities Throughout the Lower Mantle. *Science*, 306(5697):853–856.

Trampert, J. and Spetzler, J. (2006). FAST TRACK PAPER: Surface wave tomography: finite-frequency effects lost in the null space. *Geophysical Journal International - GEOPHYS J INT*, 164:394–400.

Turcotte, D. L. and Oxburgh, E. R. (1967). Finite amplitude convective cells and continental drift. *Journal of Fluid Mechanics*, 28(1):29–42.

Valentine, A. P. and Davies, D. R. (2020). Global Models From Sparse Data: A Robust Estimate of Earth's Residual Topography Spectrum. *Geochemistry, Geophysics, Geosystems*, 21(8):e2020GC009240. e2020GC009240 10.1029/2020GC009240.

Vibe, Y., Friedrich, A., Bunge, H.-P., and Clark, S. (2018). Correlations of oceanic spreading rates and hiatus surface area in the North Atlantic realm. *Lithosphere*, 10(5):677–684.

Vynnytska, L. and Bunge, H.-P. (2015). Restoring past mantle convection structure through fluid dynamic inverse theory: regularisation through surface velocity boundary conditions. *Int. J. Geomath.*, 6.

Wieczorek, M. A. and Meschede, M. (2018). SHTools: Tools for Working with Spherical Harmonics. *Geochemistry, Geophysics, Geosystems*, 19(8):2574–2592.

Wu, J. and Suppe, J. (2017). Proto-south china sea plate tectonics using subducted slab constraints from tomography. *Journal of Earth Science*, 29.

Wu, J., Suppe, J., Lu, R., and Kanda, R. (2016). Philippine sea and east asian plate tectonics since 52ma constrained by new subducted slab reconstruction methods. *Journal of Geophysical Research: Solid Earth*, 121(6):4670–4741.

Zaroli, C. (2016). Global seismic tomography using Backus-Gilbert inversion. *Geophysical Journal International*, 207(2):876–888.

Zaroli, C., Koelemeijer, P., and Lambotte, S. (2017). Toward seeing the earth's interior through unbiased tomographic lenses. *Geophysical Research Letters*, 44(22):11,399–11,408.

Zaroli, C., Sambridge, M., Lévêque, J.-J., Debayle, E., and Nolet, G. (2013). An objective rationale for the choice of regularisation parameter with application to global multiple-frequency S-wave tomography. *Solid Earth*, 4(2):357–371.

Zhang, F., Sun, Y. Q., Magnusson, L., Buizza, R., Lin, S.-J., Chen, J.-H., and Emanuel, K. (2019). What Is the Predictability Limit of Midlatitude Weather? *Journal of the Atmospheric Sciences*, 76(4):1077–1091.

Zhong, S., Yuen, D., Moresi, L., and Knepley, M. (2015). *Numerical Methods for Mantle Convection*, volume 7, pages 197–222. Elsevier Inc.

Chapter 3

A New Approach To Assessing Dynamic Topography Predictions Using Object-Based Image Processing Methods

This chapter was entirely written by A. Taiwo. It is currently under review in Geophysical Research Letters. It links to work done in meteorology and introduces an image-processing approach for the assessment and verification of dynamic topography maps.

A Meteorology Approach To Assess Mantle Flow Induced Dynamic Topography Using Object-Based Image Processing Methods

A. Taiwo[1]

[1] Department of Earth and Environmental Sciences, University of Munich, *80333* Munich, Germany. E-mail: ataiwo@geophysik.uni-muenchen.de

Key Points

- Linking mantle flow trajectories to their dynamic topography responses is critical in constraining poorly known mantle properties
- However currently applied methods for assessing dynamic topography maps are limited by double penalty
- Meteorological forecast assessment approaches that have been applied to weather maps can overcome this limitation

1 Abstract

The construction and assessment of model trajectories that link multiple mantle states is essential to constrain poorly known mantle convection parameters. Previously, volumetric approaches have been applied to assess the quality of constructed mantle flow trajectories. However, there is a need to assess these trajectories based on their dynamic topography predictions because mantle convection cannot be directly observed and must be inferred via its surface geological expressions. Typical metrics for assessing dynamic topography suffer from the *double penalty problem* — a prediction that is correct in intensity, size, and timing, but incorrect in location, results in large root-mean-square errors when compared to an observation. Here, we introduce metrics, gleaned from meteorology, that decompose any number of dynamic topography fields into their distinct objects after which the similarity between objects is compared. We find that this object-based approach overcomes double penalty and assesses models in a robust manner.

2 Plain Language Summary

Our knowledge of the amplitude, scale and temporal evolution of Earth's dynamic topography, which is steadily improving, holds important information on mantle dynamics. It is now possible to test mantle model predictions of dynamic topography against the real Earth and

thereby constrain poorly known mantle parameters. In order to properly assess dynamic topography predictions, there is a need to move away from straightforward but non-robust metrics, such as root-mean-square (rms) errors, that are unable to capture the full extent of model performance. In this paper, we introduce easily interpretable, object-based metrics which assess model performance in a way similar to what an informed human would do. We find that these object-based metrics are flexible enough that they can be used to score multiple aspects of model quality simultaneously.

3 Introduction

Over the past years, our understanding of the surface expressions of mantle convection has much improved. One such expression is the dynamic topography (Hager et al., 1985) of the Earth, which represents Earth's uplift and subsidence, away from its isostatically compensated state (see Braun, 2010, for a recent review). In attempting to compare mantle flow trajectories against the real Earth, it is necessary to assess the fit between an actual geological observable and a mantle flow prediction of the same observable. Recently, dynamic topography has been extensively studied both for the present-day (Hoggard et al. 2016; Richards et al. 2020; Holdt et al. 2022) and the past (Bunge and Glasmacher, 2018). For instance, information on its scale, amplitude and temporal evolution has been gleaned via sediment provenance (Şengör, 2001) and river profile studies (Roberts and White, 2010). The most recent effort to obtain proxy constraints about its temporal evolution is the analysis of hiatus maps (Friedrich et al. 2018; Vibe et al. 2018; Carena et al. 2019; Hayek et al. 2020, 2021). These observations provide insight into the rapidly evolving nature of geologically recent mantle convection. In other words, they offer a lens into the mantle convection system.

Parallel to this, geodynamicists have made progress in computing mantle flow trajectories for the geological past. To this end, two main computational approaches have been developed. The first, referred to as mantle circulation models (MCMs), starts off with a randomly chosen past state of the mantle and models mantle flow forward in time while assimilating plate motions and subduction histories (Bunge et al. 2002; McNamara and Zhong 2005). The second is the adjoint method (Bunge et al. 2003; Ismail-Zadeh et al. 2004; Horbach et al. 2014; Price and Davies 2017) in which a present-day estimate of the mantle state, obtained from seismic tomography (Simmons et al. 2007; Ritsema et al. 2011; French and Romanowicz 2014) is retrodicted in such a way as to improve the unknown past structure. Because of the chaotic nature of mantle convection (Stewart and Turcotte, 1989), mantle flow is subject to the so-called *butterfly effect* — the trajectories of two identical mantle convection models initialized with slightly different temperature fields diverge exponentially in time until they become uncorrelated as demonstrated by Bello et al. (2015). This effect seemingly rules out the construction of reliable mantle flow trajectories. However, geodynamicists have learned (Colli et al. 2015; Vynnytska and Bunge 2015; Bocher et al. 2016, 2018) that by assimilating the horizontal component of the surface velocity field into a mantle model, the butterfly effect can be overcome and robust mantle flow trajectories can be constructed. For the real Earth, these horizontal surface velocity motions are now available through past plate motion reconstructions over a period of at least 230 million years (Myrs) (Müller et al., 2016).

These developments necessitate an exploration of ways in which mantle models can be compared via their dynamic topography responses. One approach involves qualitative comparisons that visually identify areas of (dis-)agreement on multiple dynamic topography maps

(e.g. Colli et al. 2018). Another approach — quantitative gridpoint analyses, such as root-mean-square (rms) errors/amplitudes and spectral decompositions/correlations (e.g. Davies et al. 2019) — offers a numerical measure of model performance. This approach, however, suffers from a key drawback that has been explored extensively by meteorologists studying weather models (Baldwin and Kain 2006; Casati et al. 2008; Wilks 2011; Jolliffe and Stephenson 2012), namely: it is often difficult to give a physical interpretation to their numerical output. Also, the results of these measures often differ from, rather than complement, inferences based on a visual examination of the prediction and observation. For instance, it is possible for a predicted dynamic topography field to match observations in terms of timing, intensity and pattern of uplift (or subsidence) but to be wrong in location. An informed visual observation would classify this as a good prediction and separately account for the location error. A gridpoint-based rms quality measure, however, would penalize the prediction and classify it as poor. This is termed the *double penalty problem* (e.g. Anthes 1983; Mass et al. 2002). By double penalty, it is meant that a prediction which matches an observation in all respects except in location is penalized twice; first at the gridpoints in the prediction that do not overlap the observation, and at those gridpoints in the observation that do not overlap the prediction. It is thus imperative, in the use of dynamic topography as an indicator for mantle convection trajectories, to introduce object-based verification metrics which overcome the double penalty problem.

Though new to geodynamics, object-based verification (see Gilleland et al., 2009, for a recent summary) has been routinely performed in meteorology to evaluate forecasts of extratropical and lee cyclones (Smith and Mullen, 1993), sea breezes (Case et al., 2004), as well as deep, moist convection (Fowle and Roebber, 2003). One of the more prominent object-based techniques is the Method for Object-based Diagnostic Evaluation (MODE) (Davis et al. 2006a,b, 2009) applied to precipitation forecasts. The method uses a convolution-thresholding procedure to identify precipitation objects on forecast and observation maps and compares statistics (centroid, grid points, bounding contours, area, total rainfall etc.) for every matched pair of objects, thus allowing one to focus on regions of interest on a map.

In this paper, we link to meteorology and introduce object-based tools for assessment of dynamic topography. To this end, we use a multi-level approach as follows: the first level assesses the ability of the prediction to match objects in the observation (Roebber, 2009). The second level compares the structure, amplitude and location differences among all predicted and observed objects without matching them (Wernli et al., 2008). The final level compares the statistics of matched objects and performs a Procrustes shape analysis (Micheas et al. 2007; Lack et al. 2010) to produce a final score that represents the accuracy of a prediction. Our paper is arranged as follows: Section 3.1 describes the models used in this study. Section 4 outlines the methodology of our study. Here we describe the details of our multi-level approach. In Section 5, we present the results of our study and in Section 6, we discuss the results and draw conclusions.

3.1 Models

Our dynamic topography maps (Fig. 1) are a result of standard incompressible isoviscous, pure internal heating mantle convection simulations (e.g. Bunge and Richards 1996) at an internal heating Rayleigh number of 3×10^7 and a radial grid spacing of 22km and 30 km tangentially at the surface, decreasing to half that value at the CMB. We allow a dynamic mantle

model to evolve until it reaches a statistical steady-state at which point model quantities such as the rms velocity field are quasi-steady (see True State of Fig. 1a). This reference field is then perturbed in a manner analogous to seismic tomographic regularizations (Trampert and Spetzler, 2006). Three types of perturbations were introduced namely: radial smoothing (see Radial Smoothing in Fig. 1a), which is a radial averaging (over an interval of 100km above and below each gridpoint) of the reference field; horizontal smoothing (see Horizontal Smoothing in Fig. 1a), which is a spherical harmonic expansion and truncation of the reference field at degree 20; S20RTS smoothing (see S20RTS in Fig. 1a), which is a filtering of the reference field via the resolution operator of seismic model S20RTS (Ritsema et al. 2004; Schuberth et al. 2009). All four models, that is the reference model and the three perturbed models, are allowed to evolve freely without velocity assimilation over a transit time ($\approx$ 150 Myrs), which is the time it takes for material to traverse the mantle depth and is thus a relevant time standard to observe the surface effects of changes in the large scale buoyancy structure of the mantle. Since, as mentioned earlier, velocity assimilation helps alleviate the butterfly effect, thus leading to robust trajectories, we repeat the simulations of the perturbed models and assimilate the surface velocity field of the reference model.

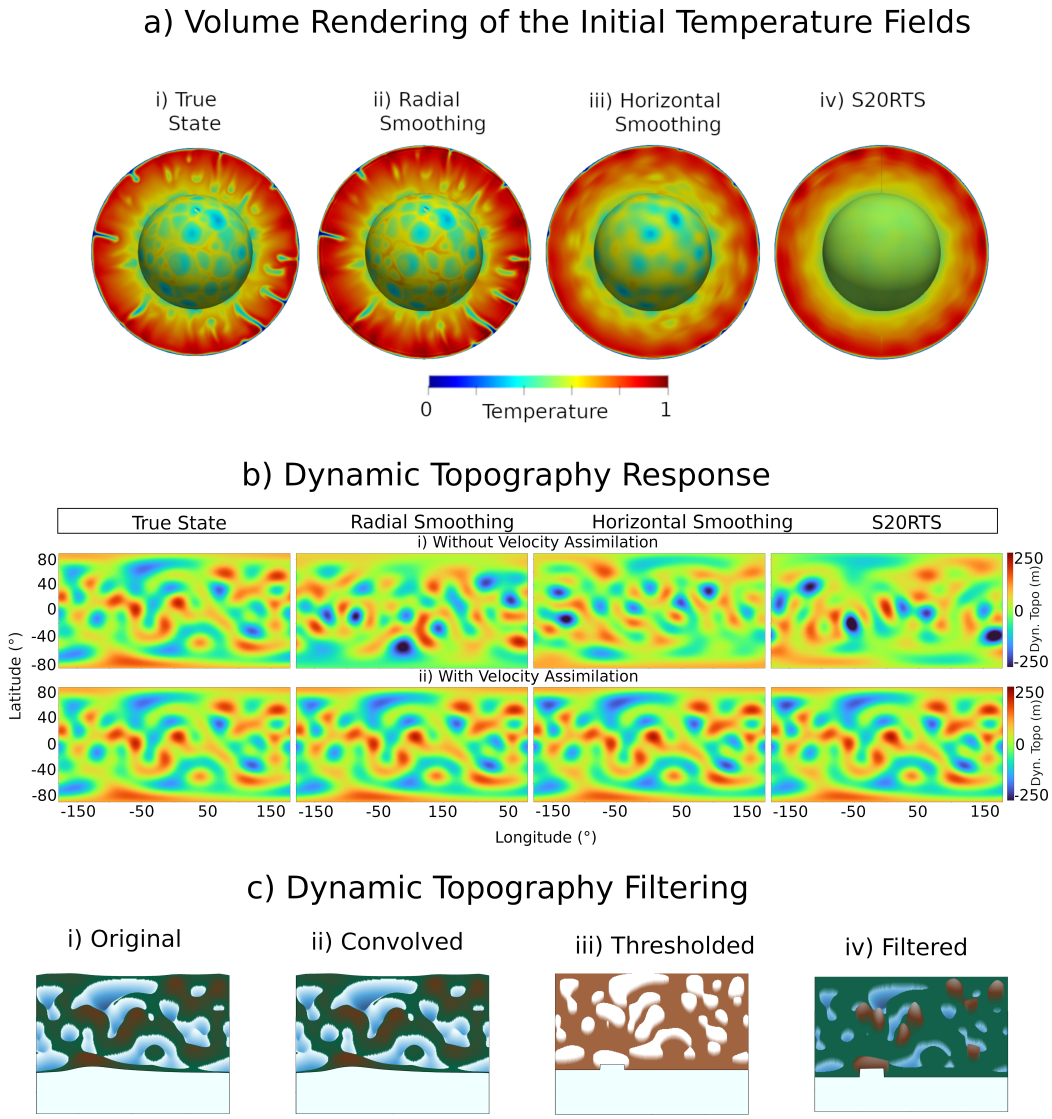

Figure 1: a) Initial temperature field (blue=cold, red=hot) for a purely internally heated isoviscous mantle convection model (True State) together with perturbed states (Radial Smoothing, Horizontal Smoothing and S20RTS), see text. b) Dynamic topography response of the mantle models in (a) after one transit time, without/with assimilation of the horizontal component of the velocity field of the true state. c) Object identification workflow shown as an example for the true state dynamic topography field in (b). The field is first convolved (ii) with a disk of radius 20 gridpoints, then a threshold (iii) is set to remove weak regions after which the filtered field (iv) is obtained. Note that the convolution-thresholding procedure filters out weak uplift and subsidence areas while preserving significant dynamic topography. See Section 4 for details.

4 Methodology

We present an object-based method for comparing any number of dynamic topography fields. Following the twin experiment approach (Lorenz, 1965), we refer to the true state (see True State in Fig. 1b) as the observation/reference and the the other fields (see Radial Smoothing, Horizontal Smoothing and S20RTS in Fig. 1b) as predictions.

4.1 Object Detection Algorithm

Using the convolution-thresholding approach (Davis et al., 2006a), we identify distinct objects on both prediction and observation fields and extract their statistics using scikit-image (van der Walt et al., 2014). We first separate each field into its uplift and subsidence parts and extract objects in each part as follows: we apply a convolution filter to smooth the field and remove small-scale variations. The smoothing is performed by convolving the field with a disk (see Fig. 1c(ii)). This convolution replaces the data value at every gridpoint with the average of the data values at all other gridpoints contained within a disk centered at that gridpoint. In our case we employ a disk radius of 20 gridpoints for fields on a 1° grid resolution. A smaller radius leads to the identification of smaller objects and vice-versa. Next, we threshold the smoothed field at every gridpoint to allow for the detection of object boundaries and to remove weak uplift/subsidence regions (see Fig. 1c(iii)). The thresholded field results in a mask of 1s and 0s (with 1s at grid points beyond the threshold and 0s otherwise). This mask is then placed on the original field and results in local, isolated, patches of uplift and subsidence objects surrounded by regions of zero values (see Fig. 1c(iv)). Since we place the mask on the original field and not on the smoothed field, we retain the original topography values for later analyses. We then match prediction and observation objects. In order to overcome the double penalty problem (see Section 3), we remove the requirement for perfect overlap of prediction and observation objects. As such, a pair of objects is matched if they share $\geq 25\%$ of grid points and have an area ratio ($area_{min}/area_{max}$) ≥ 0.4. These choices were found, in our case, to produce accurate matches.

4.2 Level 1: Performance Diagram

In constructing a performance diagram (Roebber, 2009), we define a hit, miss and false alarm. An object in the observation that is also present in the prediction is called a hit. An object in the observation that is not in the prediction is called a miss. Objects not in the observation but in the prediction are false alarms. We follow Schaefer (1990) and calculate the critical success index (CSI), probability of detection (POD), false alarm ratio (FAR), success ratio (SR) and bias as measures of prediction skill:

$$CSI = A/(A + B + C) \tag{1}$$

$$POD = A/(A + B) \tag{2}$$

$$FAR = C/(A + C) \tag{3}$$

$$SR = 1 - FAR \tag{4}$$

$$Bias = (A + C)/(A + B) \tag{5}$$

where A, B, C represent total hits, misses and false alarms respectively.

The CSI measures the ability of the prediction to produce objects that match observation objects. The POD is the percentage of objects that are correctly predicted while the FAR is a measure of the failure of the prediction to exclude the no-event/false cases. The bias is the degree of correspondence between the average prediction and the average observation. By exploiting the geometrical relationship between these measures, a performance diagram, connecting all measures, can be plotted. For accurate predictions, CSI, POD, SR and bias all approach 1, so that a perfect prediction lies at the upper right corner of the diagram (see Fig. 2a,b).

4.3 Level 2: SAL Score

In order to compare object statistics without matching object pairs, we apply the Structure, Amplitude and Location (SAL) score (Wernli et al., 2008), originally introduced for the verification of precipitation forecasts. The structure (S) score compares the scaled dynamic topographies (i.e. scaled with respect to the maximum topography within an object) of all objects in the prediction with those in the observation. This score takes on large positive values if large, flat objects are predicted relative to the observation. Negative values of S arise if smaller, strongly peaked objects are predicted relative to the observation. The amplitude (A) score compares the average dynamic topography of the prediction with that of the observation and is a measure of the amplitude deviation of the prediction from the observation. This score takes on positive values if the prediction overestimates total topography while negative values indicate underestimation. The location (L) score is split into two components. The first component measures the distance between the centers of mass of the prediction and observation fields and the second component measures the averaged distance between the center of mass of the entire field and the centers of mass of the individual objects. The final location score is a sum of both scores.

We compute the structure score as follows. For every object, a scaled intensity is defined as

$$I_n = \sum_i T_i/T_n^{max} = T_n/T_n^{max} \tag{6}$$

where T_i is the topography value at gridpoint i within an object, n, and T_n^{max} represents the maximum/minimum topography for uplift/subsidence regions within the object. The scaled intensity is calculated separately for all objects in the observation and prediction after which the weighted mean of all objects' scaled intensity is determined:

$$I(T) = \frac{\sum_{n=1}^{M} T_n I_n}{\sum_{n=1}^{M} T_n} \tag{7}$$

Finally, the S score is defined as

$$S = \frac{I(T_{fcst}) - I(T_{obs})}{0.5[I(T_{fcst}) + I(T_{obs})]} \in [-2, 2] \tag{8}$$

The amplitude score is calculated as the normalized topography difference between the observation and prediction averaged over the entire field, F:

$$A = \frac{D(T_{fcst}) - D(T_{obs})}{0.5[D(T_{fcst}) + D(T_{obs})]} \in [-2, 2] \tag{9}$$

$F(T)$, the field average of the topography field, T, is defined as:

$$F(T) = \frac{1}{N} \sum_{i \in F} T_i \tag{10}$$

where the T_i are the gridpoint values in the entire field.

The first component of the location score measures the normalized distance between the centers of mass of the prediction and observation:

$$L_1 = \frac{|\mathbf{x}(T_{fcst}) - \mathbf{x}(T_{obs})|}{d} \in [0, 1] \tag{11}$$

where d is the largest distance between any two points in the field and $\mathbf{x}(T)$ is the center of mass of the entire topography field.

The second component considers the averaged distance between the centers of mass of the total topography field and individual objects. For each object we calculate the total topography within it as

$$T_n = \sum_i T_i \tag{12}$$

where the T_i are the gridpoint values in that object.

The weighted averaged distance between the centers of mass of the individual objects, $\mathbf{x}_n$, and the center of mass of the total topography field, $\mathbf{x}$, is then given by

$$r = \frac{\sum_{n=1}^{M} R_n \, |\mathbf{x} - \mathbf{x}_n|}{\sum_{n=1}^{M} R_n} \tag{13}$$

and the second location score is given as

$$L_2 = 2\left[\frac{|r(T_{fcst}) - r(T_{obs})|}{d}\right] \in [0, 1] \tag{14}$$

4.4 Level 3: Procrustes Shape Analysis

To compare matched object pairs, we apply a Procrustes analysis (Micheas et al. 2007; Lack et al. 2010). For every matched pair, we attempt to fit, as close as possible, the geometry of the boundary of the prediction object to that of the observation. The object boundaries are extracted using a marching squares algorithm (Maple, 2003). Given matrices O and P which represent the latitude-longitude coordinates of the object boundaries of any matched pair of observation and prediction objects respectively, the Procrustes method finds an orthogonal transformation matrix Ω that closely maps P to O by minimizing a Frobenius norm as follows:

$$\begin{aligned}
\arg\min_{\Omega}(||O-\Omega P||_F) &= \arg\min_{\Omega}(||O-\Omega P||_F^2) && (15)\\
&= \arg\min_{\Omega}(tr((O-\Omega P)^T(O-\Omega P))) && (16)\\
&= \arg\min_{\Omega}(tr(O^TO+P^T\Omega^T\Omega P-2O^T\Omega P)) && (17)\\
&= \arg\min_{\Omega}(tr(O^TO)+tr(P^TP)-2tr(O^T\Omega P)) && (18)\\
&= \arg\max_{\Omega}(tr(O^T\Omega P)) && (19)\\
&= \arg\max_{\Omega}(tr(PO^T\Omega)) && (20)\\
&= \arg\max_{\Omega}(tr((U\Sigma V^T)\Omega)) && (21)\\
&= \arg\max_{\Omega}(tr(\Sigma(V^T\Omega U))) && (22)\\
&= VU^T && (23)
\end{aligned}$$

subject to $\Omega^T\Omega = I$, where I is the identity matrix, U and V are the left and right singular vectors respectively and Σ is the singular value matrix after a singular value decomposition of PO^T.

Apart from the transformed matrix ΩP, the procedure also outputs the sum of squared errors (SSE) between matrices O and ΩP normalized between 0 (best score) and 1 (worst score). We also compute the difference in average topography for each matched object pair and normalize this value between 0 (best score) and 1 (worst score). This normalized difference is denoted as θ. The preliminary score per matched object pair is given as

$$S_{prel} = SSE + \theta \tag{24}$$

such that for a perfect match, $S_{prel} = 0$ and for an imperfect match, $S_{prel} = 2$. For N matched object pairs, the average preliminary score is given by

$$S_{prel_{ave}} = \frac{\sum_{i=1}^{N} S_{prel_i}}{N} \tag{25}$$

The final score combines $S_{prel_{ave}}$ with the CSI defined in Section 4.2:

$$S_{total} = S_{prel_{ave}} + (1 - CSI) \tag{26}$$

The inclusion of the CSI helps to penalize predictions that produce few object matches with the observation even if these matches are highly accurate. In the case where there are no matches between the prediction and observation objects, CSI = 0 and $S_{prel_{ave}}$ is simply a sum of the worst SSE and θ scores. The final score then becomes

$$S_{total} = 1 + 1 + 1 = 3 \tag{27}$$

5 Results

5.1 Performance Diagram

The Performance Diagrams for uplift and subsidence areas are shown in Figs. 2a/b. For uplift regions (Fig. 2a) the models have the following scores without/with velocity assimilation: radial smoothing has POD = 0/1, SR = 0/1, CSI = 0/1. Horizontal smoothing has POD = 0.18/1, SR = 0.22/1 and CSI = 0.1/1. S20RTS has POD = 0/1, SR = 0/1 and CSI = 0/1. For subsidence regions (Fig. 2b), radial, horizontal and S20RTS smoothing all have POD = 0/1, SR = 0/0.8 and CSI = 0/0.8.

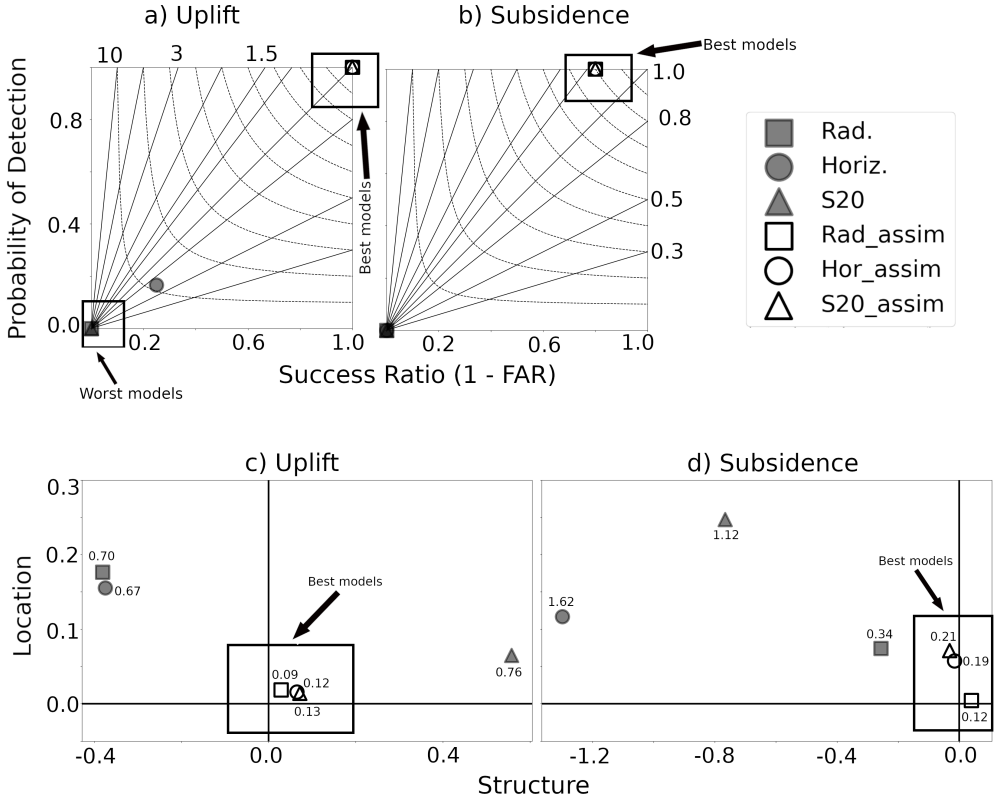

Figure 2: Performance Diagram and SAL scores (see Sections 4.2 and 4.3 respectively) between identified objects in the true state dynamic topography field and the perturbed cases (see Section 3.1 for detailed description of the various cases). Top panel (a)/(b): Performance Diagram for uplift/subsidence areas of dynamic topography. Vertical/horizontal axis denotes probability of detection/success ratio. Dotted contours represent Critical Success Index and outwardly extending solid lines represent bias scores. In both (a) and (b), figure markers plot on top of each other. Note that models with/without velocity assimilation lie close to the upper right/lower left corner, indicating good/poor similarity to the true state. Also note that the subsidence scores are slightly lower than the uplift scores. Bottom panel (c)/(d): Structure, Amplitude and Location (SAL) scores for the uplift/subsidence areas of dynamic topography. L/S scores are on the y/x axis. The amplitude (A) score is displayed adjacent to each marker on the plot. SAL scores close to 0 imply high similarity to the true state. Note that SAL scores are generally closer/farther to/from 0 for models with/without velocity assimilation. Also note that the subsidence scores are slightly higher than the uplift scores

5.2 SAL Score

Figs. 2c/d show the SAL scores for uplift and subsidence regions. In the uplift regions (Fig. 2c) the scores are as follows without/with velocity assimilation: radial smoothing has S = -0.38/0.03, A = -0.14/0.04 and L = 0.18/0.02. Horizontal smoothing has S = -0.38/0.07, A = -0.14/0.04 and L = 0.16/0.016. S20RTS has S = 0.56/0.07, A = -0.14/0.05 and L = 0.06/0.01. For the subsidence regions (Fig. 2d), the scores are as follows without/with velocity assimilation: radial smoothing has S = -0.26/0.04, A = 0.01/0.07 and L = 0.07/0.004. Horizontal smoothing has S = -1.30/-0.01, A = -0.20/0.11 and L = 0.12/0.06. S20RTS has S = -0.77/-0.03, A = -0.11/0.11 and L = 0.25/0.07. To consolidate the SAL score into a single number, we sum the absolute values of S, A and L and obtain a combined SAL score. Fig. 3a shows the combined SAL score for uplift and subsidence areas across all models. For cases without/with velocity assimilation , we have the following scores for uplift areas: radial smoothing (0.70/0.09), horizontal smoothing (0.67/0.12), S20RTS (0.76/0.13). For the subsidence regions, the scores without/with velocity assimilation are: radial smoothing (0.34/0.12), horizontal smoothing (1.62/0.19), S20RTS (1.12/0.21).

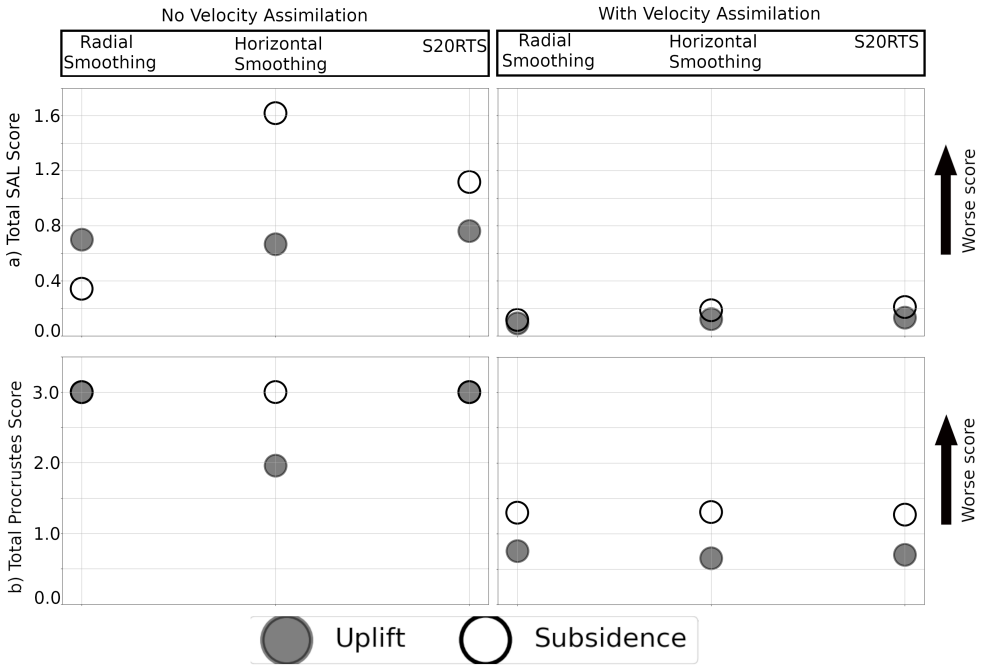

Figure 3: Total Structure, Amplitude and Location (SAL) (top panel) and Procrustes scores (bottom panel) for uplift (filled circle) and subsidence (unfilled circle) areas of dynamic topography with and without velocity assimilation, see text. Scores are calculated between the true state dynamic topography field and perturbed cases respectively (see Section 3.1 for detailed description of the various cases). Also see Sections 4.3 and 4.4 for details on SAL and Procrustes scores respectively. Note that the total SAL and Procrustes scores for uplift and subsidence regions are lower/higher with/without the assimilation of the horizontal component of the surface velocity field of the true state implying good/poor similarity to the true state.

5.3 Procrustes Score

The Procrustes skill score for all models is shown in Fig. 3b. The scores are as follows without/with velocity assimilation: radial smoothing has an uplift score of 3/0.76 and a subsidence score of 3/1.30. Horizontal smoothing has an uplift score of 1.96/0.66 and a subsidence score of 3/1.31 while S20RTS has an uplift score of 3/0.70 and a subsidence score of 3/1.27.

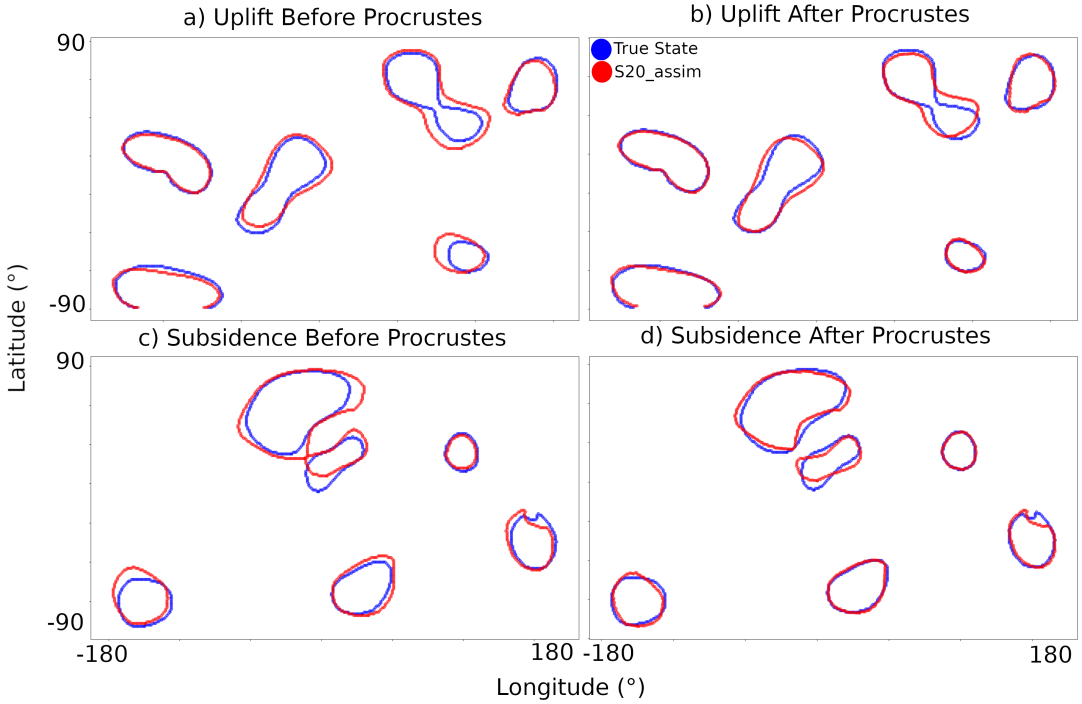

Figure 4: Procrustes shape fitting of the boundaries of matched objects in the reference dynamic topography field (see True State in Fig. 1b) shown in blue and the tomographically-filtered S20RTS field with velocity assimilation (see S20RTS in lower row of Fig. 1b) shown in red. Plots are shown separately for uplift and subsidence regions. (a)/(c) Uplift/subsidence boundaries before Procrustes fitting. (b)/(d) Uplift/subsidence boundaries after Procrustes fitting. Note that the boundaries of the S20RTS objects are displaced from those in the reference field before Procrustes fitting. After fitting, however, object boundaries align.

6 Discussion and Conclusion

In assessing mantle flow trajectories, it is imperative to use dynamic topography predictions as a proxy. This is because mantle flow, as expressed in terms of time-dependent fields, cannot be directly observed but must be inferred via its surface effects. Using an object-based approach, we here verify earlier results (Colli et al. 2015; Vynnytska and Bunge 2015; Bocher et al. 2016, 2018) on the efficacy of velocity assimilation. Our assessment of mantle flow trajectories via their dynamic topography predictions shows that models with velocity assimilation outperform those without (see Figs. 2a,b, Figs. 2c, d, 3a and Fig. 3b). The object-based approach allows us to probe the properties of identified dynamic topography objects. For instance, Figs. 2a,b show that models with velocity assimilation predict dynamic topography objects that match those in the reference twin. Furthermore, they show the difference be-

tween uplift and subsidence areas of dynamic topography. One sees in both figures that uplift areas are better predicted (as evidenced by all models lying on the upper right corner) than subsidence areas (as seen by the models lying slightly to the left of the upper right corner). This is superior to traditional assessment approaches such as correlation, which hide a great deal of model information behind a single number. The ability of our approach to separate the dynamic topography field into its uplift and subsidence regions makes it appropriate for comparisons with geological observations. Subsidence areas of dynamic topography are well constrained via past shorelines (Smith et al., 2004) while uplift areas are coming into focus via hiatus mapping (Friedrich et al. 2018; Vibe et al. 2018; Carena et al. 2019).

In extracting objects from the dynamic topography field, our convolution radius of 2000km was chosen to represent the size of hiatus surfaces on a continental scale (Hayek et al., 2020, 2021). We also chose to match objects between fields if they shared at least 25% of gridpoints. This was a subjective choice which, in our case, produced realistic matches between fields. However, other objective criteria (e.g. Davis et al. 2006a,b) could be applied in future work.

Apart from the approaches introduced here, another verification method, known as optical flow (Keil and Craig, 2007, 2009), has been developed in meteorology to compare precipitation patterns and this can be considered for dynamic topography. Additionally, shape comparison approaches such as optimal mass transport (Monge 1781; Villani 2003, 2008) can be applied to compare the boundaries of uplift and subsidence areas on dynamic topography maps. The latter has been newly applied in seismology to compare synthetic seismograms against observed data (Sambridge et al., 2022). It is clear that these object-oriented/optical flow methods are well-suited to link the growing body of geological observations to geodynamic models.

7 Open Research

The data used in this study were generated via numerical simulations by the authors as described in Section 3.1. We have used Paraview (Ahrens et al., 2005), Matplotlib (Hunter, 2007) and PyGMT (Uieda et al., 2022) for visualizations.

8 Acknowledgments

A. Taiwo thanks the Deutscher Akademischer Austausch Dienst (DAAD) for funding.

9 Collaborator Contribution

1. H.-P. Bunge supervised the research and corrected the manuscript
2. G. Craig supervised and provided guidance on the meteorological tools applied

References

Ahrens, J., Geveci, B., and Law, C. (2005). 36 - paraview: An end-user tool for large-data visualization. In Hansen, C. D. and Johnson, C. R., editors, *Visualization Handbook*, page 717–731. Butterworth-Heinemann, Burlington.

Anthes, R. A. (1983). Regional Models of the Atmosphere in Middle Latitudes. *Monthly Weather Review*, (6):1306–1335.

Baldwin, M. E. and Kain, J. S. (2006). Sensitivity of several performance measures to displacement error, bias, and event frequency. *Weather and forecasting*, 21(4):636–648.

Bello, L., Coltice, N., Tackley, P. J., Dietmar Müller, R., and Cannon, J. (2015). Assessing the role of slab rheology in coupled plate-mantle convection models. *Earth and Planetary Science Letters*, 430:191–201.

Bocher, M., Coltice, N., Fournier, A., and Tackley, P. (2016). A sequential data assimilation approach for the joint reconstruction of mantle convection and surface tectonics. *Geophysical Journal International*, 204:200–214.

Bocher, M., Fournier, A., and Coltice, N. (2018). Ensemble Kalman filter for the reconstruction of the Earth's mantle circulation. *Nonlinear Processes in Geophysics*, (1):99–123.

Braun, J. (2010). The many surface expressions of mantle dynamics. *Nature Geoscience*, 3(12):825–833.

Bunge, H. P. and Glasmacher, U. A. (2018). Models and observations of vertical motion (MoveOn) associated with rifting to passive margins: Preface. *Gondwana Research*, 53:1–8. Rifting to Passive Margins.

Bunge, H.-P., Hagelberg, C. R., and Travis, B. J. (2003). Mantle circulation models with variational data assimilation: inferring past mantle flow and structure from plate motion histories and seismic tomography. *Geophysical Journal International*, 152(2):280–301.

Bunge, H.-P. and Richards, M. A. (1996). The origin of large scale structure in mantle convection: Effects of plate motions and viscosity stratification. *Geophysical Research Letters*, 23(21):2987–2990.

Bunge, H.-P., Richards, M. A., and Baumgardner, J. R. (2002). Mantle-circulation models with sequential data assimilation: Inferring present-day mantle structure from plate-motion histories. *Philosophical Transactions: Mathematical, Physical and Engineering Sciences*, 360(1800):2545–2567.

Carena, S., Bunge, H.-P., and Friedrich, A. M. (2019). Analysis of geological hiatus surfaces across Africa in the Cenozoic and implications for the timescales of convectively-maintained topography. *Canadian Journal of Earth Sciences*, 56(12):1333–1346.

Casati, B., Wilson, L., Stephenson, D., Nurmi, P., Ghelli, A., Pocernich, M., Damrath, U., Ebert, E., Brown, B., and Mason, S. (2008). Forecast verification: current status and future directions. *Meteorological Applications: A journal of forecasting, practical applications, training techniques and modelling*, 15(1):3–18.

Case, J. L., Manobianco, J., Lane, J. E., Immer, C. D., and Merceret, F. J. (2004). An objective technique for verifying sea breezes in high-resolution numerical weather prediction models.

Colli, L., Bunge, H.-P., and Schuberth, B. S. A. (2015). On retrodictions of global mantle flow with assimilated surface velocities. *Geophys. Res. Lett.*, 42.

Colli, L., Ghelichkhan, S., Bunge, H.-P., and Oeser, J. (2018). Retrodictions of Mid Paleogene mantle flow and dynamic topography in the Atlantic region from compressible high resolution adjoint mantle convection models: Sensitivity to deep mantle viscosity and tomographic input model. In *EGU General Assembly Conference Abstracts*, EGU General Assembly Conference Abstracts, page 1985.

Davies, D. R., Valentine, A. P., Kramer, S. C., Rawlinson, N., Hoggard, M. J., Eakin, C. M., and Wilson, C. R. (2019). Earth's multi-scale topographic response to global mantle flow. *Nature Geoscience*, 12.

Davis, C., Brown, B., and Bullock, R. (2006a). Object-Based Verification of Precipitation Forecasts. Part I: Methodology and Application to Mesoscale Rain Areas. *Monthly Weather Review*, 134(7):1772.

Davis, C., Brown, B., and Bullock, R. (2006b). Object-Based Verification of Precipitation Forecasts. Part II: Application to Convective Rain Systems. *Monthly Weather Review*, 134(7):1785.

Davis, C. A., Brown, B. G., Bullock, R., and Halley-Gotway, J. (2009). The Method for Object-Based Diagnostic Evaluation (MODE) Applied to Numerical Forecasts from the 2005 NSSL/SPC Spring Program. *Weather and Forecasting*, 24(5):1252.

Fowle, M. A. and Roebber, P. J. (2003). Short-range (0–48 h) numerical prediction of convective occurrence, mode, and location.

French, S. W. and Romanowicz, B. A. (2014). Whole-mantle radially anisotropic shear velocity struc-

ture from spectral-element waveform tomography. *Geophysical Journal International*, 199(3):1303–1327.

Friedrich, A. M., Bunge, H.-P., Rieger, S. M., Colli, L., Ghelichkhan, S., and Nerlich, R. (2018). Stratigraphic framework for the plume mode of mantle convection and the analysis of interregional unconformities on geological maps. *Gondwana Research*, pages 159–188. Rifting to Passive Margins.

Gilleland, E., Ahijevych, D., Brown, B. G., Casati, B., and Ebert, E. E. (2009). Intercomparison of spatial forecast verification methods. *Weather and forecasting*, 24(5):1416–1430.

Hager, B. H., Clayton, R. W., Richards, M. A., Comer, R. P., and Dziewonski, A. M. (1985). Lower mantle heterogeneity, dynamic topography and the geoid. *Nature*, 313.

Hayek, J. N., Vilacís, B., Bunge, H.-P., Friedrich, A. M., Carena, S., and Vibe, Y. (2021). Correction: Continent-scale hiatus maps for the atlantic realm and australia since the upper jurassic and links to mantle flow-induced dynamic topography. *Proc. R. Soc. A*, 477(2251):20210437.

Hayek, N., Vilacis, B., Bunge, H.-P., Friedrich, A., Carena, S., and Vibe, Y. (2020). Continent-scale Hiatus Maps for the Atlantic Realm and Australia since the Upper Jurassic and links to mantle flow induced dynamic topography. *Proc. R. Soc. A*.

Hoggard, M. J., White, N., and Al-Attar, D. (2016). Global dynamic topography observations reveal limited influence of large-scale mantle flow. *Nature Geoscience*, 9.

Holdt, M. C., White, N. J., Stephenson, S. N., and Conway-Jones, B. W. (2022). Densely sampled global dynamic topographic observations and their significance. *Journal of Geophysical Research: Solid Earth*, 127(7):e2022JB024391. e2022JB024391 2022JB024391.

Horbach, A., Bunge, H.-P., and Oeser, J. (2014). The adjoint method in geodynamics: derivation from a general operator formulation and application to the initial condition problem in a high resolution mantle circulation model. *GEM - International Journal on Geomathematics*, 5(2):163–194.

Hunter, J. D. (2007). Matplotlib: A 2d graphics environment. *Computing in Science & Engineering*, 9(3):90–95.

Ismail-Zadeh, A., Schubert, G., Tsepelev, I., and Korotkii, A. (2004). Inverse problem of thermal convection: numerical approach and application to mantle plume restoration. *Physics of the Earth and Planetary Interiors*, 145(1):99–114.

Jolliffe, I. T. and Stephenson, D. B. (2012). *Forecast verification: a practitioner's guide in atmospheric science*. John Wiley & Sons.

Keil, C. and Craig, G. (2007). A displacement-based error measure applied in a regional ensemble forecasting system. *Monthly Weather Review*, 135:3248–3259.

Keil, C. and Craig, G. (2009). A displacement and amplitude score employing an optical flow technique. *Weather and Forecasting*, 24:1297–1308.

Lack, S. A., Limpert, G. L., and Fox, N. I. (2010). An object-oriented multiscale verification scheme. *Weather and Forecasting*, 25(1):79–92.

Lorenz, E. N. (1965). A study of the predictability of a 28-variable atmospheric model. *Tellus*, 17(3):321–333.

Maple, C. (2003). Geometric design and space planning using the marching squares and marching cube algorithms. In *2003 International Conference on Geometric Modeling and Graphics, 2003. Proceedings*, pages 90–95.

Mass, C. F., Ovens, D., Westrick, K., and Colle, B. A. (2002). Does Increasing Horizontal Resolution Produce More Skillful Forecasts?. *Bulletin of the American Meteorological Society*, 83(3):407–430.

McNamara, A. K. and Zhong, S. (2005). Degree-one mantle convection: Dependence on internal heating and temperature-dependent rheology. *Geophysical Research Letters*, 32(1).

Micheas, A., Fox, N. I., Lack, S. A., and Wikle, C. K. (2007). Cell identification and verification of qpf ensembles using shape analysis techniques. 344:105–116.

Monge, G. (1781). Mémoire sur la théorie des déblais et des remblais. *Histoire de l'Académie Royale des Sciences de Paris*.

Müller, R. D., Seton, M., Zahirovic, S., Williams, S. E., Matthews, K. J., Wright, N. M., Shephard, G. E., Maloney, K. T., Barnett-Moore, N., Hosseinpour, M., Bower, D. J., and Cannon, J. (2016).

Ocean Basin Evolution and Global-Scale Plate Reorganization Events Since Pangea Breakup. *Annual Review of Earth and Planetary Sciences*, 44(1):107–138.

Price, M. G. and Davies, J. H. (2017). Profiling the robustness, efficiency and limits of the forward-adjoint method for 3-D mantle convection modelling. *Geophysical Journal International*, 212(2):1450–1462.

Richards, F. D., Hoggard, M. J., White, N., and Ghelichkhan, S. (2020). Quantifying the relationship between short-wavelength dynamic topography and thermomechanical structure of the upper mantle using calibrated parameterization of anelasticity. *Journal of Geophysical Research: Solid Earth*, 125(9):e2019JB019062. e2019JB019062 10.1029/2019JB019062.

Ritsema, J., A. Deuss, H. v. H., and Woodhouse, J. (2011). S40RTS: a degree-40 shear-velocity model for the mantle from new Rayleigh wave dispersion, teleseismic traveltime and normal-mode splitting function measurements. *Geophysical Journal International*, 184:1223–1236.

Ritsema, J., van Heijst, H. J., and Woodhouse, J. H. (2004). Global transition zone tomography. *Journal of Geophysical Research: Solid Earth*, 109(B2).

Roberts, G. G. and White, N. (2010). Estimating uplift rate histories from river profiles using African examples. *Journal of Geophysical Research: Solid Earth*, 115(B2).

Roebber, P. J. (2009). Visualizing Multiple Measures of Forecast Quality. *Weather and Forecasting*, (2):601–608.

Sambridge, M., Jackson, A., and Valentine, A. P. (2022). Geophysical inversion and optimal transport. *Geophysical Journal International*. ggac151.

Schaefer, J. T. (1990). The critical success index as an indicator of warning skill. *Weather and Forecasting*, 5(4):570–575.

Schuberth, B. S. A., Bunge, H.-P., Steinle-Neumann, G., Moder, C., and Oeser, J. (2009). Thermal versus elastic heterogeneity in high-resolution mantle circulation models with pyrolite composition: High plume excess temperatures in the lowermost mantle. *Geochemistry, Geophysics, Geosystems*, 10(1).

Şengör, A. M. C. (2001). Elevation as indicator of mantle-plume activity. In *Mantle plumes: their identification through time*. Geological Society of America.

Simmons, N., Forte, A., and Grand, S. (2007). Thermochemical structure and dynamics of the african superplume. *Geophys. Res. Lett*, 34(2).

Smith, A. G., Smith, D. G., and Funnell, B. M. (2004). *Atlas of Mesozoic and Cenozoic Coastlines*.

Smith, B. B. and Mullen, S. L. (1993). An evaluation of sea level cyclone forecasts produced by nmc's nested-grid model and global spectral model.

Stewart, C. A. and Turcotte, D. L. (1989). The route to chaos in thermal convection at infinite Prandtl number: 1. Some trajectories and bifurcations. *Journal of Geophysical Research: Solid Earth*, 94(B10):13707–13717.

Trampert, J. and Spetzler, J. (2006). FAST TRACK PAPER: Surface wave tomography: finite-frequency effects lost in the null space. *Geophysical Journal International - GEOPHYS J INT*, 164:394–400.

Uieda, L., Tian, D., Leong, W. J., Jones, M., Schlitzer, W., Grund, M., Toney, L., Fröhlich, Y., Yao, J., Magen, Y., Materna, K., Belem, A., Newton, T., Anant, A., Ziebarth, M., Quinn, J., and Wessel, P. (2022). PyGMT: A Python interface for the Generic Mapping Tools.

van der Walt, S., Schönberger, J. L., Nunez-Iglesias, J., Boulogne, F., Warner, J. D., Yager, N., Gouillart, E., Yu, T., and the scikit-image contributors (2014). scikit-image: image processing in Python. *PeerJ*, 2:e453.

Vibe, Y., Friedrich, A., Bunge, H.-P., and Clark, S. (2018). Correlations of oceanic spreading rates and hiatus surface area in the North Atlantic realm. *Lithosphere*, 10(5):677–684.

Villani, C. (2003). *Topics in optimal transportation*. Graduate studies in mathematics ; v. 58. American Mathematical Society, Providence, R.I.

Villani, C. (2008). Optimal transport, old and new. notes for the 2005 saint-flour summer school. *Grundlehren der mathematischen Wissenschaften [Fundamental Principles of Mathematical Sci-*

ences]. Springer.

Vynnytska, L. and Bunge, H. (2015). Restoring past mantle convection structure through fluid dynamic inverse theory: regularisation through surface velocity boundary conditions. *Int. J. Geomath.*, 6.

Wernli, H., Paulat, M., Hagen, M., and Frei, C. (2008). Sal—a novel quality measure for the verification of quantitative precipitation forecasts. *Monthly Weather Review*, 136(11):4470–4487.

Wilks, D. S. (2011). *Statistical methods in the atmospheric sciences*, volume 100. Academic press.

Chapter 4

Assessing Dynamic Topography Histories of Geodynamic Models using Object-based Image Processing Tools: Verification through Synthetic Adjoint Predictions of Southern African Uplift

This chapter was entirely written by A. Taiwo. It builds off of the previous chapter and applies a number of global gridpoint and regional object-based metrics to assess adjoint-based dynamic topography predictions. Here I compare global and regional metrics against each other and argue that regional metrics are better suited for dynamic topography studies.

Assessing Dynamic Topography Histories of Geodynamic Models using Object-based Image Processing Tools: Verification through Synthetic Adjoint Predictions of Southern African Uplift

A. Taiwo[1]

[1] Department of Earth and Environmental Sciences, University of Munich, *80333* Munich, Germany

1 ABSTRACT

In comparing model-predicted dynamic topography to the real Earth, two approaches can be employed. The first, a global analysis, assesses an entire dynamic topography field at once. This approach is useful because it summarises global information contained on thousands of gridpoints into a few numerical values. On the other hand, such an approach suffers not only from the *double penalty problem* — a prediction which closely matches an observation in all other respects except in location is penalized twice; once as a miss and once as a false alarm — but also from the fact that global coverage of dynamic topography is non-uniform. Some areas of dynamic topography are better mapped than others. As such, any model assessment using these methods may suffer from inaccurate results. The second approach involves a regional analysis on so-called *limited-area domains* via object-based image processing tools. This approach has the ability to separate a global dynamic topography map into its different uplift and subsidence regions. By so doing, it allows to focus on regions of interest or regions with good dynamic topography information. In this paper, we explore a number of global and regional metrics for assessing dynamic topography. To this end, we introduce an object-based image processing method and test it on four synthetic adjoint predictions of the southern African uplift. We show that while global analysis provides first-order information on model performance, the ability of the object-based regional analysis approach to focus on specific regions of interest offers an advantage in terms of the final quality of model information obtained. Such object-based methods are already applied in meteorological studies and we introduce them for the first time in the context of dynamic topography.

2 INTRODUCTION

Computational advances have now made it possible to create parallelized, highly scalable and high resolution models of mantle convection (e.g Zhong et al. 2015; Kronbichler et al. 2012; Burstedde et al. 2013; Heister et al. 2017; Bauer et al. 2020). Through the use of mantle

circulation models, referred to as MCMs (Ricard et al. 1993; Bunge et al. 2002; McNamara and Zhong 2005; Bower et al. 2013; Flament et al. 2014) and the adjoint method (Bunge et al. 2003; Ismail-Zadeh et al. 2004; Horbach et al. 2014; Ghelichkhan and Bunge 2016; Price and Davies 2017), geodynamicists can now construct forward and inverse trajectories respectively of mantle flow. MCMs simulate mantle flow forward in time by assuming a random past state of the mantle and assimilating plate motion and subduction histories. The adjoint method, on the other hand, starts off with a best guess of the present-day state of the mantle as obtained from seismic tomography (Simmons et al. 2007; Ritsema et al. 2011; French and Romanowicz 2014) and reconstructs its past state whilst also assimilating information on plate motion history. The ability of the adjoint method to combine volume and surface information offer it an advantage over MCMs. This advantage is clearly seen when mantle flow trajectories are linked to their surface manifestations, such as dynamic topography (Pekeris 1935; Hager et al. 1985). In the case of MCMs, dynamic topography is reasonably well predicted for subsidence regions since these models, by definition, assimilate subduction histories. For uplift regions, however, MCMs are generally unable to produce correct patterns because they have incorrect information on the locations of plumes within the mantle volume (Müller et al., 2018). The adjoint method, on the other hand, is able to better predict uplift and subsidence patterns of dynamic topography due to its ability to combine surface and volume information. The availability of powerful tools like the adjoint method necessitate the testing of constructed mantle flow trajectories against real Earth dynamic topography.

Africa is an exceptional continent to explore the interaction between continental topography and mantle convection. The continent is characterized by a distinct Basin and Swell topography which has long been suggested to result from convective processes in the underlying mantle (e.g. Burke and Gunnell, 2008). Africa's hypsometry (i.e., its land elevation relative to sea level) is also highly anomalous, with about 1/2 of the continent standing at elevations of greater than 500 m. Moreover, the African plate has moved slowly North-eastward within a hot spot frame of reference since the early Oligocene (33-23 million years ago (Ma)) (Burke, 1996). This implies that the analysis of the vertical motions of Africa is not complicated by horizontal plate motions or subduction (Lithgow-Bertelloni and Silver, 1998). Drawing on a host of observations, including soil weathering, fission-track studies, volcanic activity and offshore sediment deposition, Burke and Gunnell (2008) concluded that the southern Africa topography is comparatively young, suggesting that much of the present-day relief developed during the Cenozoic ($\approx$ 60 Ma) in response to subcontinental mantle convection processes. Despite the evidence for this young topography over southern Africa, there are other arguments, based on thermochronology, that argue for a Cretaceous (145 Ma) age of southern Africa topography (Gallagher and Brown 1999; Tinker et al. 2008).

Given the advances in the construction of mantle flow trajectories, it is paramount to link mantle models to dynamic topography. Once a model prediction of dynamic topography has been made, there are several ways in which one can compare the extent to which the prediction matches the actual observed dynamic topography. Qualitative comparisons, which visually identify areas of (dis-)agreement on multiple dynamic topography maps (e.g. Colli et al. 2018; Flament et al. 2013) represent a quick, first-order method. On the other hand, quantitative analyses of dynamic topography, such as root-mean-square (rms) errors/amplitudes (Flament et al., 2013) and spectral decompositions (Davies et al., 2019) offer a numerical measure of model performance. These quantitative metrics, however, suffer from the double penalty

problem (e.g. Anthes 1983; Mass et al. 2002). By double penalty, it is meant that a prediction which closely matches an observation in all other respects except in location is penalized twice; first at the gridpoints in the prediction that do not overlap the observation, and at those gridpoints in the observation that do not overlap the prediction. To overcome this problem, it is imperative to apply object-based verification methods which not only account for location differences but also provide more robust information regarding model performance.

These object-based verifications have already been applied in meteorology to evaluate forecasts of extratropical and lee cyclones (Wernli and Schwierz 2006; Smith and Mullen 1993), sea breezes (Case et al., 2004), deep, moist convection (Fowle and Roebber 2003; Done et al. 2004) and precipitation (Davis et al. 2006a,b, 2009; Ebert and McBride 2000). One of the more prominent object-based techniques was introduced by Ebert and McBride (2000) who verified precipitation forecasts via definition of contiguous rain areas (CRAs), which are areas of overlap between forecast and observation. They identified CRAs by superposing forecast onto the observation and computed an rms error for every identified CRA. This rms error was then decomposed according to its various contributions (displacement, pattern and volume of rain) to clearly isolate the various sources of prediction error.

In this paper, we introduce an object-based image processing method for the assessment of dynamic topography and investigate to what extent this approach can be used for regional, small-scale or subcontinental analysis. As mentioned earlier, the timing of the southern Africa uplift is hotly contested. As such we focus our analysis on model-predicted uplift of this region. The model predictions used in this study come from recent adjoint simulations by Ghelichkhan et al. (2021). These simulations use a mesh that discretizes the Earth's mantle with $\approx$ 670 million finite element nodes. This value corresponds to a grid point resolution of 11 km radially, and 14 km tangentially at the surface, decreasing to half that value at the Core-Mantle Boundary (CMB) and allows one to resolve global mantle flow at Earth-like convective vigor. The calculations were performed on 2048 computational cores of the SuperMUC facility at the Leibniz Supercomputing Centre (LRZ) in Munich (Germany) and a local computer cluster dedicated to capacity geophysical modelling (Oeser et al., 2006). Our paper is arranged as follows: Section 3 outlines the methodology of our study. Here we describe the Taylor diagram, power ratio, two-time correlation function, as well as our object identification approach. In Section 4, we present the results of our study. We end our paper with a discussion in Section 5 and draw some conclusions in Section 6.

2.1 Dataset

The dynamic topography maps (Fig. 1) used in this paper are a result of adjoint-based simulations obtained from a combination of two seismic tomography state estimates of the mantle with two viscosity profiles resulting in a total of 4 end-member models. The two tomography state estimates are based on the whole-mantle tomography models LLNL-G3D-JPS (Simmons et al., 2015) and SEMUCB-WM1 (French and Romanowicz, 2014). Both models were supplemented with SL2013sv (Schaeffer and Lebedev, 2013) for depths shallower than 400 km and are referred to in this paper as SL and SS respectively. The viscosity profiles used in this study were derived by inverting for geoid and CMB topography constraints in a manner consistent with the chosen mantle heterogeneity structure obtained from the tomographic models. Both viscosity profiles (*mu1* and *mu2*) start off with values of 1.4×10^{20} Pa s in

the asthenosphere, increasing by an order of magnitude in the lower upper mantle. In the lower 200 km, however, *mu1* has a viscosity of 2×10^{22} Pa s while *mu2* has a viscosity of 2×10^{23}Pa s. The four model end-members are named mu1-SL, mu1-SS, mu2-SL and mu2-SS, reflecting the combination of seismic tomography and viscosity profile. Of all these models, model mu2-SL is entirely unable to produce the southern African uplift (see Fig. 1c).

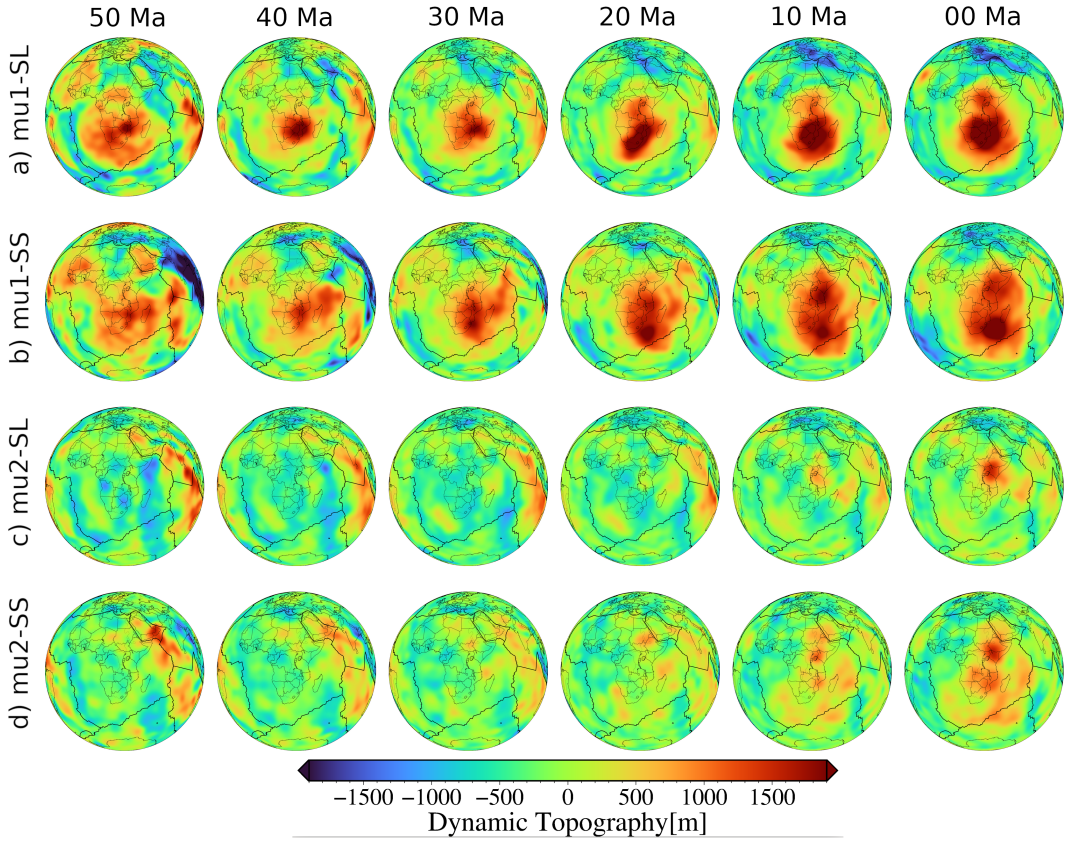

Figure 1: Global dynamic topography maps for four end-member models ((a) mu1-SL; b) mu1-SS; c) mu2-SL; d) mu2-SS, see Section 2.1 for details) shown over a time span of 50 million years (Ma). 00 Ma/50 Ma represents present-day/50 million years ago. Blue/red colors represent subsidence/uplift. The maps are centered to reveal the evolution of the southern African uplift. Note that models mu1-SL and mu1-SS, both with overall lower viscosity, produce strong uplift in southern Africa while models mu2-SL and mu2-SS, both with overall higher viscosity, either do not produce or only produce a weak uplift in southern Africa.

3 METHODS

We follow the twin experiment approach (Lorenz, 1965) and select model mu1-SL as the reference (observation) twin against which other twins are compared. The other models, mu1-SS, mu2-SL and mu2-SS are referred to as perturbed (prediction) twins. We proceed to first compute a number of global gridpoint metrics such as the Taylor diagram, power ratio and two-time correlation function (TTCF). Next we perform a regional scale analysis focusing only on southern Africa. Here, we compute the TTCF for only the southern Africa

uplift after which we apply the object-based method to extract this uplift and then rank the perturbed twins based on their ability to reproduce the uplift as seen in the reference twin.

3.1 Taylor Diagram

The Taylor diagram (Taylor, 2001) is a commonly employed metric in meteorology for comparing multiple predictions of the same observation. It provides a concise way of displaying the degree of correspondence between reference and perturbed fields. The diagram shows the Pearson correlation coefficient (i.e. the covariance between two variables divided by the product of their standard deviations) and rms error between the two fields, along with their respective standard deviations all at once. The benefit of plotting all 3 variables on the same figure is seen in the fact that each metric complements the rest. For example, the correlation coefficient provides information about the pattern of variation between the two fields but doesn't offer any information regarding the amplitude of their variations. This second, important, information can be gleaned from the rms error. Therefore, in combination, the correlation coefficient and the rms error provide information about pattern and amplitude of variations between two fields but do not provide information on how much variation is due to differences in structure and phase. In combination with the standard deviations of the fields, a summary of the important aspects of the differences between the two fields can thus be obtained. These 3 quantities are related by the following error propagation formula:

$$E^2 = \sigma_r^2 + \sigma_p^2 - 2\sigma_r\sigma_p\rho \tag{1}$$

where ρ and E are the correlation coefficient and centered rms difference between the reference and perturbed fields respectively and σ_r and σ_p are their respective standard deviations.

To obtain ρ, σ_r and σ_p, we perform spherical harmonic expansions of the respective fields using SHTOOLS (Wieczorek and Meschede, 2018). After obtaining the spherical harmonic coefficients, we compute the spectral power of each field per spherical harmonic degree ℓ as:

$$\sigma_\ell^2 = \sum_{m=0}^{\ell} (a_{\ell m}^2 + b_{\ell m}^2) \tag{2}$$

where $a_{\ell m}$ and $b_{\ell m}$ are the fully normalized (Stacey, 1992) coefficients of the spherical harmonic expansion at degree ℓ and order m.

The rms amplitude is then given by:

$$\sigma_{rms} = \sqrt{\sum_{\ell=1}^{\ell_{max}} \sigma_\ell^2} \tag{3}$$

Next, we calculate the correlation between reference and perturbed fields for every harmonic degree as:

$$r^\ell = \frac{\sum_{m=0}^{\ell}(a_{\ell m}c_{\ell m} + b_{\ell m}d_{\ell m})}{\sqrt{\sum_{m=0}^{\ell}(a_{\ell m}^2 + b_{\ell m}^2)}\sqrt{\sum_{m=0}^{\ell}(c_{\ell m}^2 + d_{\ell m}^2)}} \tag{4}$$

where $a_{\ell m}$, $b_{\ell m}$ are the coefficients of the spherical harmonic expansion for the reference field and $c_{\ell m}$, $d_{\ell m}$ are the expansions for the perturbed field.

The total correlation up to $\ell_{max} = 40$, ρ, is given by:

$$\rho = \frac{\sum_{\ell=1}^{\ell_{max}} \sum_{m=0}^{\ell} (a_{\ell m} c_{\ell m} + b_{\ell m} d_{\ell m})}{\sigma_{rms}^{\{a_{\ell m}, b_{\ell m}\}} \sigma_{rms}^{\{c_{\ell m}, d_{\ell m}\}}} \tag{5}$$

where $\sigma_{rms}^{\{a_{\ell m}, b_{\ell m}\}}$ and $\sigma_{rms}^{\{c_{\ell m}, d_{\ell m}\}}$ are the rms amplitudes for reference and perturbed models respectively.

By comparing eqn. 1 with the law of cosines, a geometrical relationship between the four quantities (E, σ_r, σ_p and ρ) is formed and thus we obtain the Taylor Diagram, which in our case is plotted by adapting code from Copin (2012).

3.2 Power Ratio

Following Surcel et al. (2015), we compute a ratio of variances to study the scales at which our dynamic topography maps begin to decorrelate. Given $D_i, D_j, (i, j = 1, ..., N)$ dynamic topography maps and assuming their variance is defined, the following holds:

$$Var\left(\sum_{i=1}^{N} D_i\right) = \sum_{i=1}^{N} Var(D_i) + \sum_{i \neq j} Cov(D_i, D_j) \tag{6}$$

where $Var(D_i)$ is the variance for the ith dynamic topography field and $Cov(D_i, D_j)$ are the pairwise covariances.

We perform a spherical harmonic expansion of the dynamic topography maps and for each harmonic degree, we compute a variance Var_λ at the lengthscale corresponding to that harmonic degree.

The power ratio for each lengthscale λ is then defined as:

$$R(\lambda) = \frac{\sum_{i=1}^{N} Var(D_i)_\lambda}{Var\left(\sum_{i=1}^{N} D_i\right)_\lambda} \tag{7}$$

If the fields are fully decorrelated, it follows that their pairwise covariance $Cov(D_i, D_j) = 0$ for all $i \neq j$. We therefore have that

$$R(\lambda) = 1 \tag{8}$$

And for perfectly correlated ensembles, we have:

$$R(\lambda) = 1/N \tag{9}$$

For negatively correlated ensembles, the power ratio exceeds 1 and for anti-correlated ensembles, the power ratio is undefined.

3.3 Two-Time Correlation Function (TTCF)

Apart from comparing model performance instantaneously, it is also possible to compare over time. The two-time correlation function (TTCF) allows the construction of a time correlation matrix between the reference and perturbed dynamic topography fields. Here, we compute global as well as regional TTCFs.

3.3.1 Global TTCF

We first obtain spherical harmonic expansions of all dynamic topography fields at each time using SHTOOLS (Wieczorek and Meschede, 2018). We then compute the correlations between reference and perturbed twins at any two times, t_1 and t_2:

$$R(t_1, t_2) = \frac{\sum_{\ell=1}^{\ell_{max}} \sum_{m=0}^{\ell} (a_{\ell m}^{t_1} c_{\ell m}^{t_2} + b_{\ell m}^{t_1} d_{\ell m}^{t_2})}{\sigma_{rms}^{\{a_{\ell m}^{t_1}, b_{\ell m}^{t_1}\}} \sigma_{rms}^{\{c_{\ell m}^{t_2}, d_{\ell m}^{t_2}\}}} \tag{10}$$

where

l, m, $l_{max} = 40$ are the harmonic degree, harmonic order and maximum harmonic degree,

$a_{\ell m}^{t_1}$, $b_{\ell m}^{t_1}$ are the fully normalized (Stacey, 1992) coefficients of the spherical harmonic expansion of the reference dynamic topography field at time, t_1

$c_{\ell m}^{t_2}$, $d_{\ell m}^{t_2}$ are the fully normalized coefficients of the spherical harmonic expansion of the perturbed dynamic topography field at time, t_2

$\sigma_{rms}^{\{a_{\ell m}^{t_1}, b_{\ell m}^{t_1}\}}$ is the rms amplitude of the reference field at time, t_1

$\sigma_{rms}^{\{c_{\ell m}^{t_2}, d_{\ell m}^{t_2}\}}$ is the rms amplitude of the perturbed field at time, t_2

3.3.2 Regional TTCF

In order to focus the analysis on southern Africa, we compute regional TTCFs with the aid of the discrete cosine transform (DCT) (Ahmed et al. 1974; Denis et al. 2002) which is an alternative to spherical harmonics when one performs an analysis not on the entire globe but on a regional scale or on so-called *limited-area domains*. In principle, a Fast Fourier Transform (FFT) could be used in place of the DCT. However, the superiority of the DCT over FFT is that it eliminates problems associated with discontinuities at the boundaries of our limited-area domain. For a 2-D field $f(i, j)$ with N_i by N_j grid points, the DCT is defined (Denis et al., 2002) as:

$$\begin{aligned} F(m,n) = \beta(m)\beta(n)\Sigma_{i=0}^{i=N_i-1}\Sigma_{j=0}^{j=N_j-1} f(i,j) \\ \times cos\left[\pi m \frac{(i+1/2)}{N_i}\right] cos\left[\pi n \frac{(j+1/2)}{N_j}\right] \end{aligned} \tag{11}$$

where

$$\beta(m) = \begin{cases} \sqrt{\frac{1}{N_i}}, & m = 0 \\ \sqrt{\frac{2}{N_i}}, & m = 1, 2, ..., N_i - 1 \end{cases} \tag{12}$$

$$\beta(n) = \begin{cases} \sqrt{\frac{1}{N_j}}, & n = 0 \\ \sqrt{\frac{2}{N_j}}, & n = 1, 2, ..., N_j - 1 \end{cases} \tag{13}$$

and $F(m, n)$ is the spectral coefficient corresponding to the (m, n) adimensional wavenumbers. Note that $F(m, n)$ is also an array of N_i by N_j real spectral coefficients.

The total rms apmplitude is obtained as:

$$\sigma_{rms} = \sqrt{\Sigma_{n=0}^{N_i-1}\Sigma_{m=0}^{N_j-1}\frac{F(m,n)^2}{N_i N_j}} \qquad (m, n) \neq (0, 0) \tag{14}$$

Finally, the correlation between a reference and perturbed twin at any two times, t_1 and t_2 is given as:

$$R(t_1, t_2) = \frac{\Sigma_{n=0}^{N_i-1}\Sigma_{m=0}^{N_j-1} F_{ref}^{t_1}(m, n) \times F_{pert}^{t_2}(m, n)}{\sigma_{rms}^{ref^{t_1}} \times \sigma_{rms}^{pert^{t_2}} \times N_i \times N_j} \qquad (m, n) \neq (0, 0) \tag{15}$$

where σ_{rms}^{ref} and σ_{rms}^{pert} are the rms amplitudes of the reference and perturbed twins respectively.

Observe that in the computation of σ_{rms} as well as R, we do not consider $F(0, 0)$ as this component is related to the domain average.

To serve as a basis of comparison for other TTCF computations, we first compute the TTCF of the reference field with itself. For the global TTCF, this implies that $a_{\ell m}^t = c_{\ell m}^t$ and $b_{\ell m}^t = d_{\ell m}^t$ for any one time, t. For the regional TTCF, this means that $F_{ref}^t = F_{fcst}^t = F$ for any one time t. For two identical fields at time $t_1 = t_2 = t$, the TTCF achieves a maximum value of 1 along its diagonal and this value decreases away from the diagonal implying lower correlations with increasing time lag.

3.4 Object Detection Algorithm

We present the object detection algorithm with which we isolate the southern Africa uplift. This approach can equally be applied to other fields (e.g. hiatus maps, precipitation, radar reflectivity) that can be represented on a latitude-longitude grid. Using the convolution-thresholding approach (Davis et al., 2006a,b, 2009), we isolate this uplift on each dynamic topography field at 00 Ma (present-day) and extract its statistics via image-processing tools from the Python package, scikit-image (van der Walt et al., 2014). To this end, we separate the field into its uplift and subsidence parts and extract the southern Africa uplift as follows:

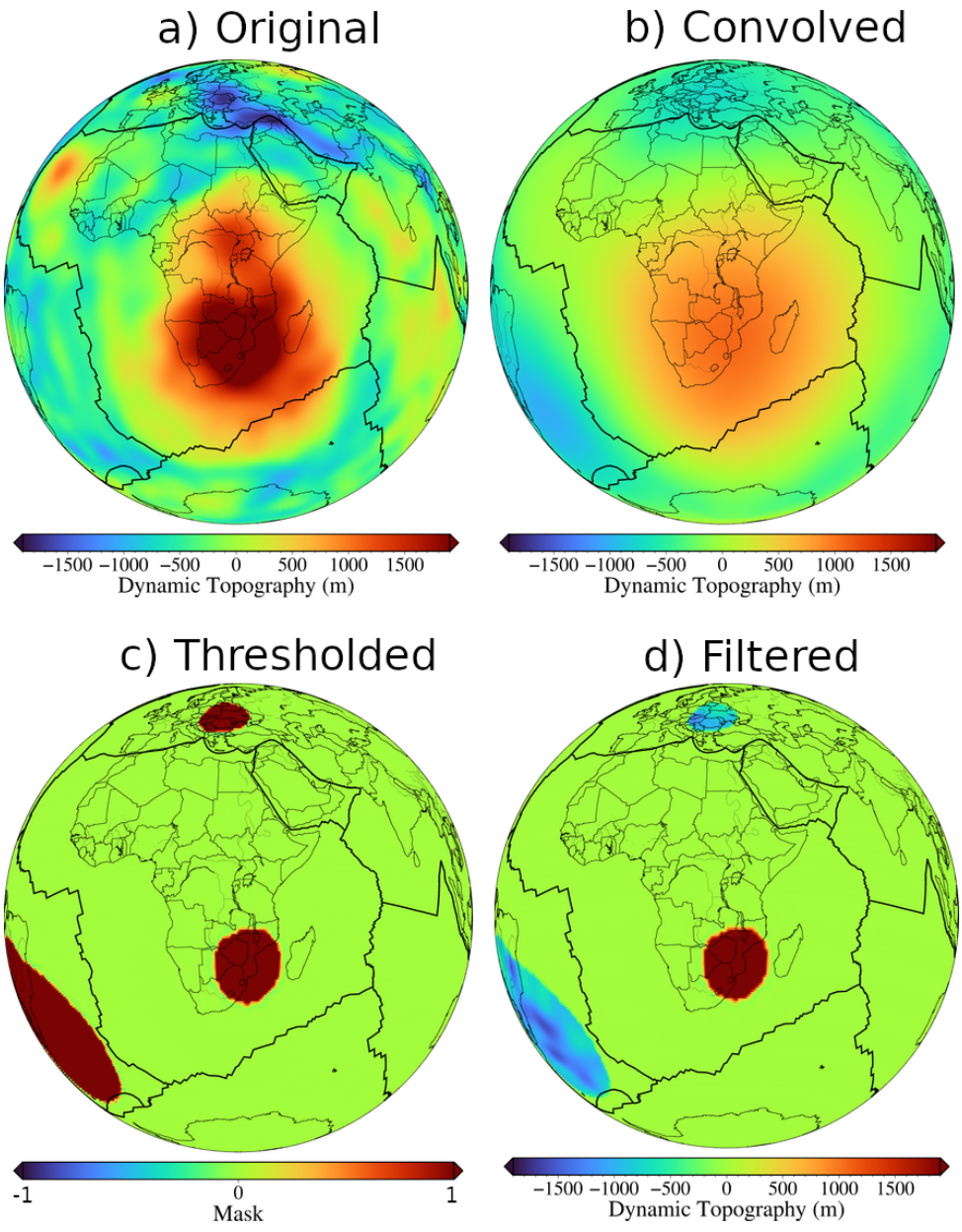

Figure 2: Object identification workflow shown in 3-D but only for model mu1-SL at 00 Ma (see Fig. 1 for details). The field is first convolved (Fig. 2b) with a disk to smooth out small-scale variations. A threshold (Fig. 2c) is then set such that regions with dynamic topography below the threshold are set to zero while those above the threshold are preserved (see filtered field in Fig. 2d). Note how the convolution-thresholding procedure filters out weak uplift and subsidence areas while preserving significant dynamic topography. See Section 3.4 for details.

we first apply a convolution filter to smooth the field and remove small-scale variations (see Fig. 2b). The smoothing is performed by convolving the field with a disk. This convolution replaces the data value at every gridpoint with the average of the data values at all other gridpoints contained within a disk centered at that gridpoint. The choice of disk radius impacts the size of identified objects. A smaller radius leads to the identification of smaller objects and vice-versa. In our case we employed a radius of 25 gridpoints for data on a 1° grid resolution. Next, we threshold the smoothed field at every gridpoint to allow for the detection of object boundaries and to remove weak uplift/subsidence regions (see Fig. 2c). For this we applied a threshold of 800 m. The thresholded field results in a mask of 1s and 0s (with 1s at grid points beyond the threshold and 0s otherwise). This mask is then placed on the original field and results in an isolated patch representing the uplift (see Fig. 2d). It is this uplift patch that is referred to as an object. Since we place the mask on the original field and not on the smoothed field, we retain the original topography values for later analyses.

3.5 Procrustes Shape Analysis with Time Penalty

The perturbed dynamic topography differs from the reference dynamic topography not only in space but in time. In order to account for this, we introduce a score that compares the models in terms of spatial accuracy as well as time. As a first step, we apply a Procrustes shape analysis to compare the southern Africa uplift objects based on their geometry, location and average topography. In this regard, we attempt to fit, as close as possible, the geometry of the boundary of the perturbed southern Africa object to that of its match in the reference. The object boundaries are extracted using a marching squares algorithm (Maple, 2003). To this end, both reference and perturbed fields are transformed to gray-scale images (where the gridpoint values of every object are 1 and those of empty areas are 0) and the algorithm searches for constant-valued contours at the interface between the 1s and 0s. Given matrices O and P which represent the latitude-longitude coordinates of the object boundaries of any matched pair of reference and perturbed objects respectively, the Procrustes method finds an orthogonal transformation matrix Ω that closely maps P to O by minimizing a Frobenius norm as follows:

$$\begin{aligned}
\arg\min_{\Omega}(||O-\Omega P||_F) &= \arg\min_{\Omega}(||O-\Omega P||_F^2) && (16)\\
&= \arg\min_{\Omega}(tr((O-\Omega P)^T(O-\Omega P))) && (17)\\
&= \arg\min_{\Omega}(tr(O^TO+P^T\Omega^T\Omega P-2O^T\Omega P)) && (18)\\
&= \arg\min_{\Omega}(tr(O^TO)+tr(P^TP)-2tr(O^T\Omega P)) && (19)\\
&= \arg\max_{\Omega}(tr(O^T\Omega P)) && (20)\\
&= \arg\max_{\Omega}(tr(PO^T\Omega)) && (21)\\
&= \arg\max_{\Omega}(tr((U\Sigma V^T)\Omega)) && (22)\\
&= \arg\max_{\Omega}(tr(\Sigma(V^T\Omega U))) && (23)\\
&= VU^T && (24)
\end{aligned}$$

Table 1: Boundary values of the skill score. Best possible score is 0 and this occurs in the event of perfect match with perfect timing. Worst possible score is 4 which occurs in the event of imperfect match and imperfect timing.

	Perfect Timing	Imperfect Timing
Perfect Match	$0 + 0 = 0$	$0 + 2 = 2$
Imperfect Match	$2 + 0 = 2$	$2 + 2 = 4$

subject to $\Omega^T\Omega = I$, where I is the identity matrix, U and V are the left and right singular vectors respectively and Σ is the singular value matrix after a singular value decomposition of PO^T.

Apart from the transformed matrix ΩP, the procedure also outputs the sum of squared errors (SSE) between matrices O and ΩP normalized between 0 (best score) and 1 (worst score). We compute the difference in average topography between the reference and perturbed object and normalize this value between 0 (best score) and 1 (worst score). This normalized difference is denoted as θ and is computed as:

$$\theta = \frac{|D_{pert} - D_{ref}|}{D_{pert} + D_{ref}} \in [0, 1] \tag{25}$$

where D_{pert} and D_{ref} are the average dynamic topography values for the southern African uplift in the perturbed and reference twin respectively.

The preliminary score is then given by:

$$S_{prel} = SSE + \theta \tag{26}$$

such that for a perfect match, $S_{prel} = 0$ and for an imperfect match, $S_{prel} = 2$.

Next we define the time penalty as the normalized difference between the times at which the southern Africa uplift first appears in reference and perturbed twins and scale by a factor of 2 to ensure that this penalty is comparable to the preliminary score:

$$T = \frac{2|t_{ref} - t_{pert}|}{t_{ref} - 0} \in [0, 2] \tag{27}$$

where t_{pert} and t_{ref} are the times at which the southern Africa uplift first appears in perturbed and reference twins respectively. Observe that the denominator of eqn. 27 is the maximum possible time difference between the onset of the uplift in reference and perturbed twins.

The final score combines S_{prel} with T as follows:

$$S_{total} = S_{prel} + T \tag{28}$$

so that the lowest (best) score is 2 and the highest (worst) score is 4.

We can also calculate the area (in km^2) enclosed by the uplift as follows. Consider that an object or region on the Earth surface is enclosed by the boundary made up of λ_0, λ_1, ..., λ_N

longitude points and ϕ_0, ϕ_1, ..., ϕ_N corresponding latitude points, the area of the irregular polygon bounded by these coordinates is given by Chamberlain and Duquette (2007) as:

$$Area = \frac{-R^2}{2}\Sigma_{i=0}^{N-1}(\lambda_{i+1} - \lambda_{i-1}).sin\phi_i \tag{29}$$

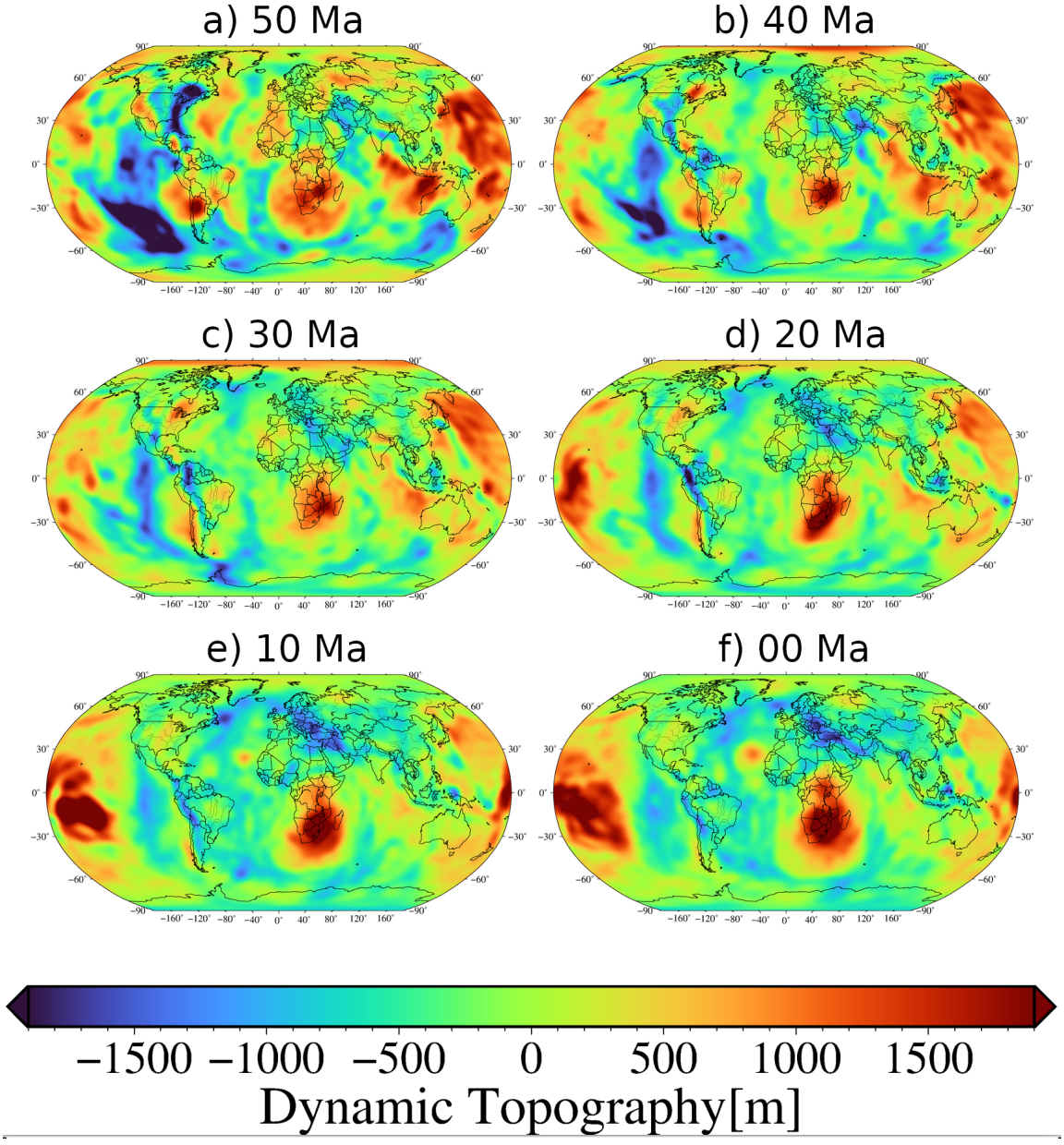

Figure 3: Global dynamic topography maps for model mu1-SL (see Section 2.1 for details) displayed on a Robinson projection from 50 million years ago (50 Ma) to present-day (00 Ma). Blue/red represent subsidence/uplift. The essence of displaying this figure is to emphasize that the results of the Taylor diagram, power ratio and global two-time correlation function (see Section 3 for details on the three methods) were obtained from a global analysis of the dynamic topograhy maps.

4 RESULTS

As mentioned in Section 3, we show the Taylor diagram, power ratio and global TTCF for the entire dynamic topography field as shown in Fig. 3. We also show a regional TTCF for a limited-area domain covering only southern Africa as seen in Fig. 6. The difference between Figs. 1 and 3 is that the former shows the entire globe at once while the latter shows only a hemisphere centered on Africa.

4.1 Taylor Diagram

Fig. 4 shows the Taylor diagrams for all models at various times, with model mu1-SL as the reference. At 50 Ma, mu1-SS has a correlation with the reference of 0.31 and an rms error of 820 m. Model mu2-SL has a correlation of 0.6 with the reference and an rms error of 590 m while mu2-SS has a correlation of 0.31 with the reference and an rms error around 700 m. At 40 Ma, mu1-SS has a correlation of 0.38 with the reference and an rms error of 620 m while mu2-SL has a correlation of 0.58 and an rms error of 490 m. Model mu2-SS has a correlation of 0.38 and an rms error of 590 m. At 30 Ma, mu1-SS has a correlation of 0.4 and an rms error of 500 m and mu2-SL has a correlation of 0.55 and an rms error of 460 m. Model mu2-SS has a correlation of 0.5 and an rms error of 465 m. At 20 Ma, mu1-SS has a correlation of 0.5 and an rms error of 465 m while mu2-SL has a correlation of 0.57 and an rms error of 445 m. Model mu2-SS has a correlation of 0.6 and an rms error of 420m. By 10 Ma, mu1-SS has a correlation of 0.65 and an rms error of 510m while mu2-SL has a correlation of 0.6 and an rms error of 520m. Model mu2-SS has a correlation of 0.68 and an rms error of 455m. At 00 Ma, mu1-SS has a correlation of 0.75 and an rms error of 450 m while mu2-SL has a correlation of 0.62 and an rms error of 450 m. Model mu2-SS has a correlation of 0.7 and an rms error of 445 m.

4.2 Power Ratio

Fig. 5 shows the power ratio, that is the ensemble correlation, for all time periods. At 50 Ma (red line in Figs. 5g,h,i), the models show very low correlation at spherical harmonic degree 4 where the power ratio is around 0.8. This poor correlation is maintained until degree 27 when the power ratio gets very close to the 0.25 line. However, again at degree 40, the models become anti-correlated as evidenced by the power ratio exceeding a value of 1. A similar trend can be seen at 40 Ma (blue line in Figs. 5g,h,i), although the models correlate better than at 50 Ma. By separating the power ratio to its uplift and subsidence components, we see that at both 40 Ma and 50 Ma, the decreasing correlation is generally due to areas of subsidence. Overall in this time period, the subsidence areas show a higher power ratio (poorer correlation) than the uplift areas. At 20 Ma and 30 Ma (Figs. 5d,e,f), the models correlate strongly across all spherical harmonic degrees and the power ratio hovers around 0.5. However at degree 37, there is a sharp increase in the subsidence power ratio at 30 Ma (red line in Fig. 5f) implying that the subsidence areas of dynamic topography across all models become anti-correlated at this degree. At 0 Ma and 10 Ma (Figs. 5a,b,c), the models have a power ratio hovering around 0.5 except at degree 31, where the 0 Ma power ratio exceeds 0.6. This increased power ratio is a result of the poor correlations in the uplift areas of dynamic topography across the models at that spherical harmonic degree, as can be seen from Fig. 5b). Overall, across all times and degrees, the models are highly correlated and in cases where uplift regions are less correlated, this effect is counterbalanced by stronger

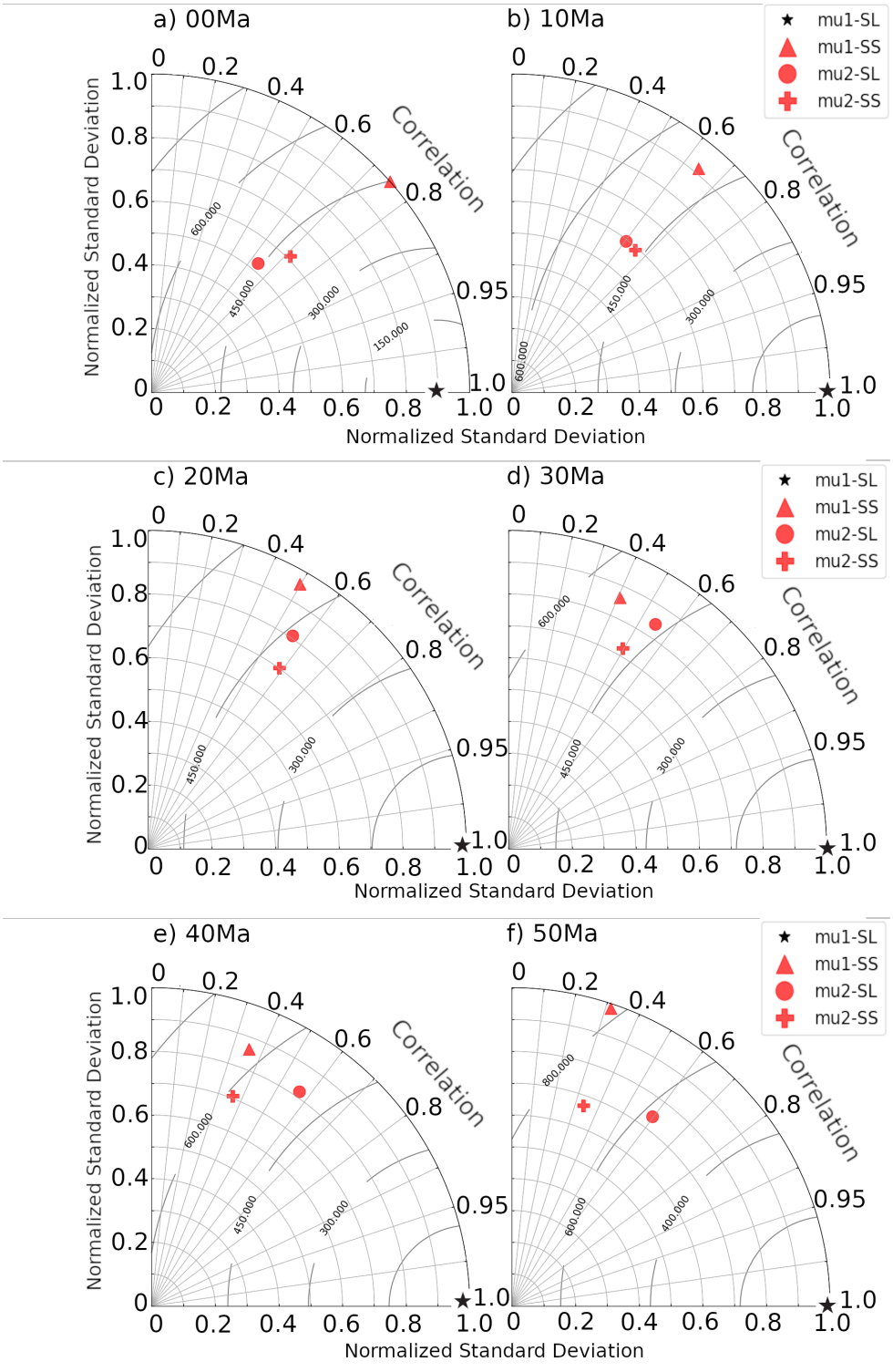

Figure 4: Taylor Diagram showing rms errors and Pearson correlations between model mu1-SL and models mu1-SS, mu2-SL and mu2-SS (see Section 2.1 for details) from present-day (00 Ma) to 50 million years ago (50 Ma). It also shows the normalized (with respect to the largest standard deviation of that case) standard deviations for each field at a particular time. Model mu1-SL (reference twin) is shown as the black star. The rms errors (in metres, m) are represented by contours. Correlation lines are drawn in increments of 0.1 except after 0.9 where the last 3 values are 0.95. 0.99 and 1.0. Note that the correlations/rms errors increase/decrease the closer one gets to present-day.

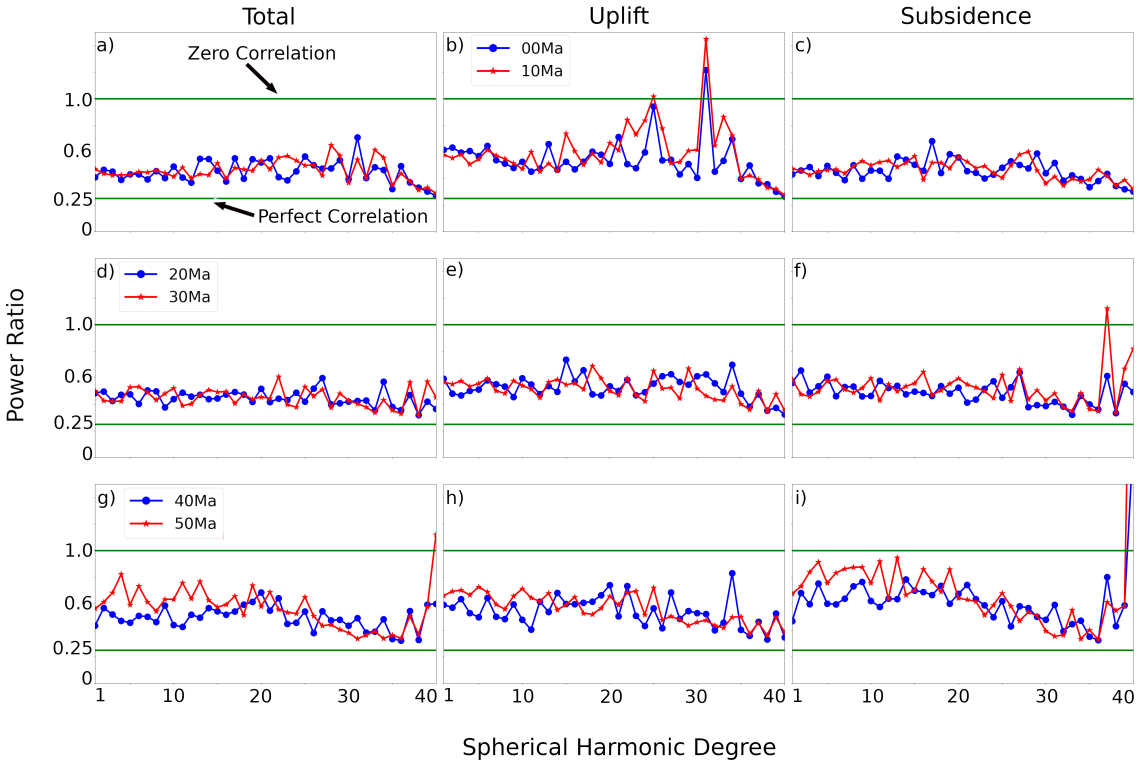

Figure 5: Power Ratio for the model ensemble comprising mu1-SL, mu1-SS, mu2-Sl and mu2-SS shown for total fields (1st column of figure), uplift regions (second column of figure) and subsidence regions (third column of figure) across different times from present day (00 Ma) to 50 million years ago (50 Ma). The vertical axis shows the power ratio, which is a ratio of variances that points to the lengthscales (or spherical harmonic degrees) at which an ensemble of dynamic topography maps begin to decorrelate. The horizontal green lines at 0.25/1 denote perfect/zero correlation. The horizontal axis shows the spherical harmonic degree. Note that the power ratio is highest (i.e. least correlation) at 40 Ma and 50 Ma and progressively decreases until present-day.

correlations in subsidence areas and vice-versa.

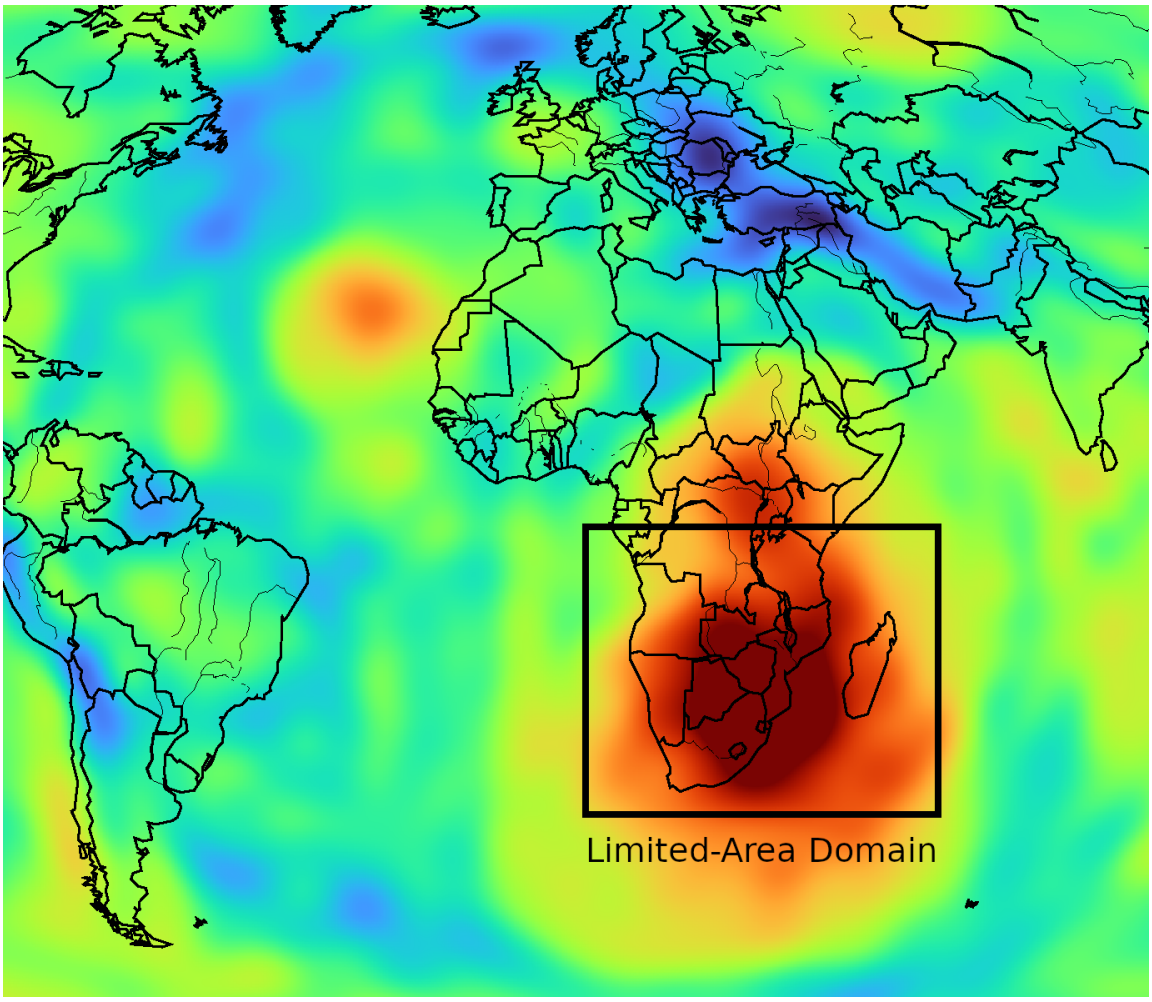

Figure 6: Limited-area domain map of model mu1-SL (see Section 2.1 for details) at present-day (00 Ma) showing the analysis region used in the calculation of the regional two-time correlation function (TTCF) (see Section 3.3.2). In this case, the entire globe is ignored and the TTCF computes two-time correlations only for the area covered by the southern African uplift.

4.3 Global and Regional TTCF

Fig. 7 shows the TTCF across models globally (Fig. 7i) and specifically for the southern African uplift (Fig. 7ii). As seen from Fig. 7a, the TTCF of the reference model with itself shows a symmetrical pattern with the highest correlation occurring along the diagonal and gradually decreasing outwards. Here, the correlation length, which is a measure of the time duration for which the model is perfectly correlated with itself, is around 10 million years (Myrs). We superpose the contour lines of the reference model (mu1-SL) onto the other TTCF plots to aid comparison. Looking globally, we observe from Fig. 7i(b,c,d), that the best correlation between the reference and the other models occurs at 0Ma. Model mu1-SS (Fig. 7i(b)) shows the poorest correlation with the reference as evidenced by the fact that

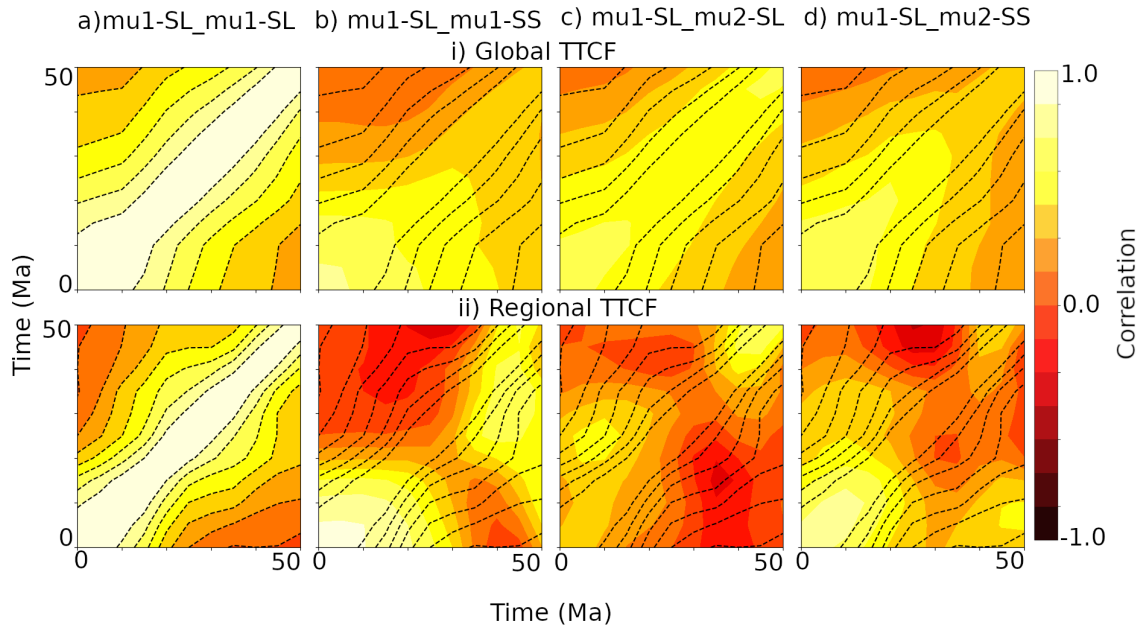

Figure 7: Two-time correlation functions (TTCF) for global (see Fig. 1 for all models at all times) and limited-area domain (see Fig. 6 for an example of model mu1-SL at present-day (00 Ma)). The TTCF is a time correlation matrix that shows the correlation between any two time slices of a dynamic topography map. Dotted black lines show the correlation contours for model mu1-SL (first column) superposed on all other plots to aid comparison. Contours decrease in increments of 0.2 away from the axis of symmetry. i) Global TTCF across models mu1-SL, mu1-SS, mu2-SL and mu2-SS. ii) Regional TTCF for the same models.

the zero correlation contour is closer to the diagonal than in the other figures. Model mu2-SL (Fig. 7i(c)) shows the best TTCF and in this case, the contour lines of the true state have the best fit compared to the other models. Model mu2-SS (Fig. 7i(d)) also performs better than model mu1-SS but the contour lines of the reference model do not fit it as well as model mu2-SL. Focusing on the regional TTCF of Fig. 7ii, we see that model mu1-SS has the best correlations at present-day (lower left corner in Fig. 7ii(b)) and at 50 Ma (upper right corner of Fig. 7ii(b)). Amongst all perturbed models (Fig. 7ii(b,c,d)), this model has the best correlations along the diagonal. Model mu2-SL (Fig. 7ii(c)) is poorly correlated with the reference except at 50 Ma, where there is a slight positive correlation. Finally, model mu2-SS (Fig. 7ii(d)) shows slight positive correlation between 0 Ma and 10 Ma and this is due to the fact that this model only begins to produce the southern Africa uplift in this time window.

4.4 Procrustes Analysis

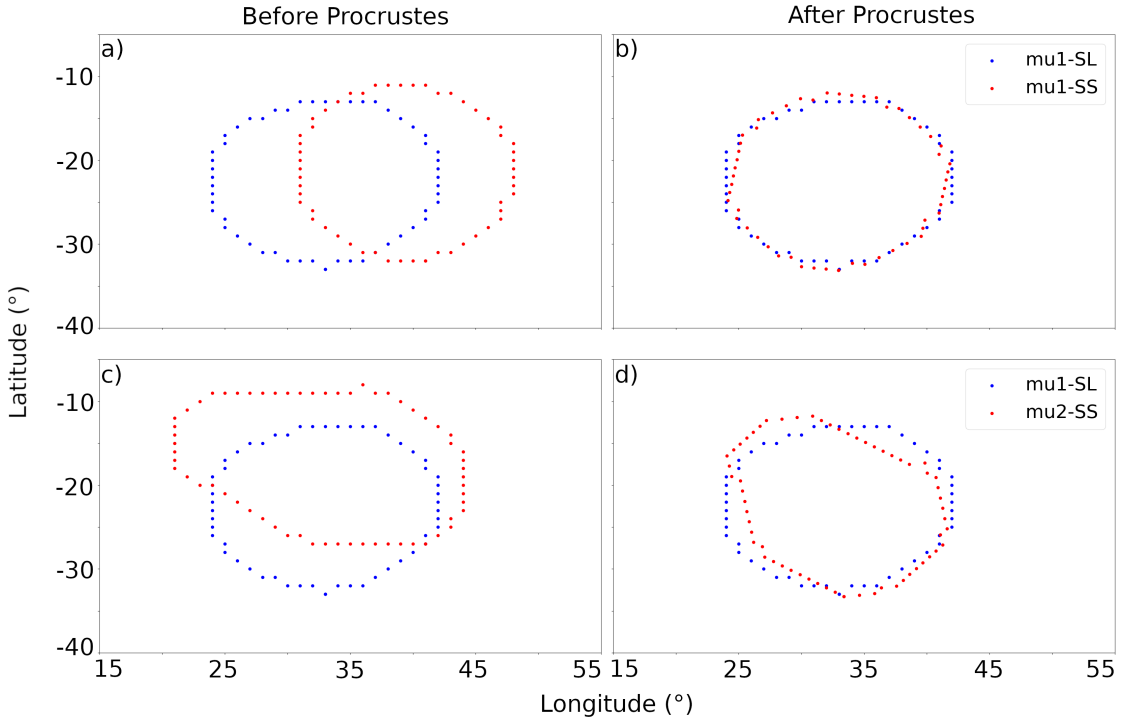

Figure 8: Illustration of the Procrustes shape fitting of the boundaries of the southern African uplift where in models mu1-SS and mu2-SS are fit to model mu1-SL (see Section 2.1 for details). Panels a)/c) show the boundaries of models mu1-SS/mu2-SS before Procrustes fitting. Panels b)/d) show the boundaries of models mu1-SS/mu2-SS after Procrustes fitting. Observe how the boundaries of mu1-SS and mu2-SS are displaced from that of mu1-SL before Procrustes fitting. After fitting, however, object boundaries align. Note the absence of model mu2-SL. As noted in Section 2.1, this model is unable to produce the southern African uplift. As such, no boundary comparison can be made.

Fig. 8 shows the boundaries of the southern Africa uplift region for models mu1-SL, mu1-SS and mu2-SS before and after the application of the Procrustes algorithm. Since the southern Africa uplift is absent in model mu2-SL, we do not apply the object detection algorithm to this model. As before, model mu1-SL is the reference model. We see that in model mu1-SL, the

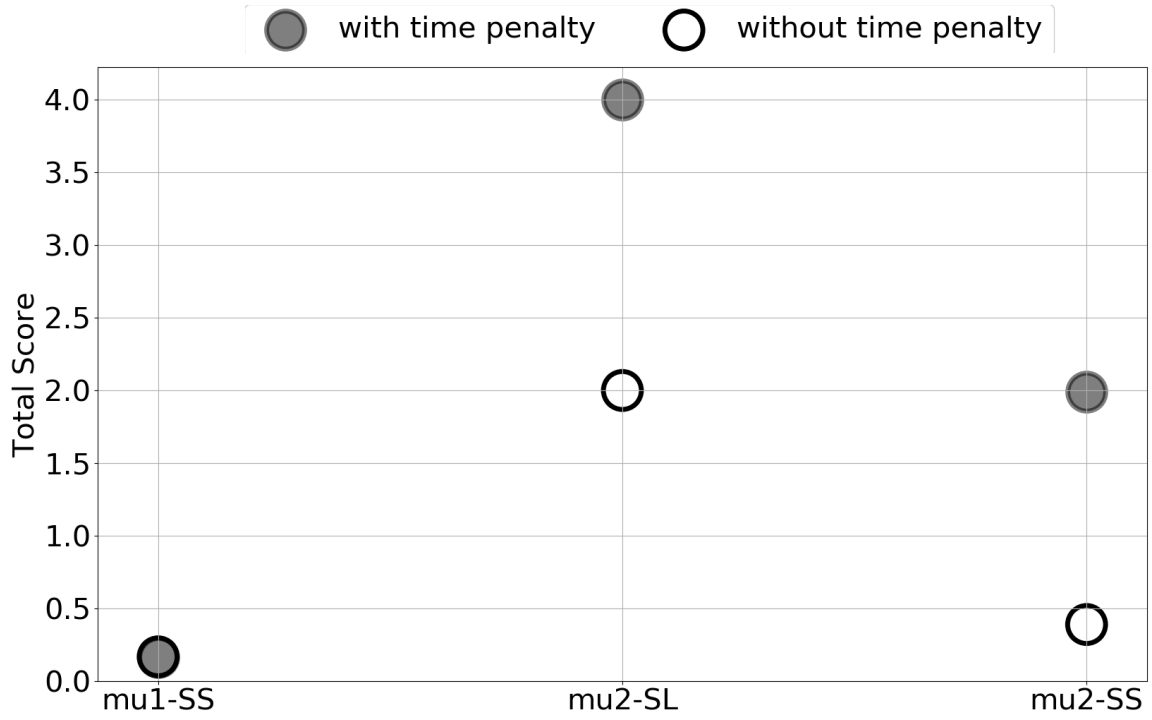

Figure 9: Total Procrustes score for the southern African uplift with and without the time penalty, shown for models mu1-SS, mu2-SL and mu2-SS. The time penalty is introduced to penalise models that have a different appearance time for the southern African uplift compared to model mu1-SL. Open/filled circles represent scores without/with time penalty. Higher/lower scores represent worse/better performance in comparison to model mu1-SL. Note that model mu2-SL has the worst scores with/without time penalty because this model is entirely unable to produce the southern African uplift.

southern Africa uplift is centered at 22°N,32°E. Before the Procrustes analysis, model mu1-SS (Fig. 8a) is centered at 21°N,39°E while model mu2-SS has its centroid at 17°N,33°E (Fig. 8c). After applying the Procrustes procedure (see Section 3.5), again with model mu1-SL as the reference, we observe that models mu1-SS and mu2-SS are shifted, scaled and rotated until they best align with model mu1-SL at which point their centroids coincide with that of mu1-SL as seen in Figs. 8b and d respectively. Fig. 9, shows the results of scoring models mu1-SS, mu2-SL and mu2-SS with respect to mu1-SL (reference). The figure shows the final scores with and without application of the time penalty. Model mu1-SS has the best score of 0.17 without the time penalty. With time penalty, the score remains unchanged. This is because this model produces the southern Africa uplift at the same time as the reference mu1-SL model. Without time penalty, model mu2-SL has a score of 2 due to the absence of the southern Africa uplift in this model. With time penalty, the final score for this model is 4. For model mu2-SS, the score without time penalty is 0.39 but with time penalty, the final score is 2.

5 DISCUSSION

Our constantly improving understanding of the amplitude, scale and temporal evolution of Earth's dynamic topography (Braun 2010; Hoggard et al. 2016; Bunge and Glasmacher 2018; Davies et al. 2019; Valentine and Davies 2020; Hoggard et al. 2017; Holdt et al. 2022; Friedrich et al. 2018; Vibe et al. 2018; Carena et al. 2019; Hayek et al. 2020, 2021) necessitate a comparison of mantle flow trajectories against dynamic topography histories. To this end, two key approaches can be employed. The first approach involves the usage of global gridpoint metrics such as rms errors and spatial/spectral/time correlations. However, the double penalty problem as well as the abstract nature of such metrics imply that much model information is lost during their computation and interpretation. By combining any two of these gridpoint metrics, more sophisticated model information can be obtained. The Taylor diagram (Taylor, 2001), power ratio (Surcel et al., 2015) and TTCF represent combinations of much simpler metrics. For instance, by displaying rms errors, correlations and standard deviations simultaneously, the Taylor diagram provides phase, scale and amplitude information at once. The power ratio is also a measure of model correlation. Its advantage over Pearson correlation (Freedman et al., 2007) or spectral correlation is that unlike the latter where only a pair of models can be correlated at once, the power ratio allows for the correlation of an ensemble of models and provides information about the lengthscales over which the ensemble (de-)correlates. The TTCF is a measure of temporal correlation. However, unlike typical approaches that correlate models at any two times, the TTCF computes a correlation of models between all times and displays the result in a single plot. It is clear that metrics such as these represent a significant step in the search for robust and succinct methods of assessing model accuracy. Despite the advantages of these metrics, they still do not overcome the double penalty problem and thus penalize reasonably good models based on location differences. This is crucial because the dynamic topography of Earth is better known at some locations than at others. For example, the disappearance of the *Western Interior Seaway* at the end of the Cretaceous (145-66 Ma) has been well mapped and linked to surface depressions induced by mantle downwellings in this region (Burgess et al., 1997). However, other areas, particularly in the oceans, remain poorly known. The gridpoint metrics we have applied in this paper cannot distinguish between well-known and poorly known areas on a dynamic topography map. Such metrics simply score models based on comparisons at every gridpoint

so that for poorly known areas of dynamic topography, a model continuously accumulates penalties. Additionally, the results of these global gridpoint metrics are influenced, in principle, by information across the entire globe. An example can be seen in the results of the Taylor diagram (Fig. 4). Here, model mu2-SL, which does not produce the southern African uplift, shows a similar correlation value with the other models (mu1-SS and mu2-SS) and this model even has the highest correlations to the reference case at 40 Ma (Fig. 4e) and 50 Ma (Fig. 4f). This is an initially surprising result. However, the ambiguity is resolved when one realises that the Taylor diagram is computed globally. As such, gridpoints far away from southern Africa contribute positively to the correlation score for this model. In essence, the results of these global gridpoint metrics are at best not easily interpretable and at worst, inaccurate. A way to overcome this problem is to compute these gridpoint metrics for regions of the Earth where reliable dynamic topography information exists. As an example, one could ignore the oceans, where dynamic topography information is sparse and perform a sub-continental/continental analysis as we showed with the regional TTCF (Fig. 7ii). The power ratio can also be computed on a continental or sub-continental scale via the application of Fourier transforms (Errico, 1985) or discrete cosine transforms (Ahmed et al. 1974; Denis et al. 2002) on limited-area domains. However, for ensembles comprising only a small number of models, the power ratio becomes noisy, especially on limited-area domains (Surcel et al., 2015). Overall, despite the persistence of the butterfly effect, such local/regional scale usage of these gridpoint metrics still provide better model assessment than their usage on a global scale.

Meteorologists have long understood the challenges involved with gridpoint metrics and this has led to the introduction of object-based verification methods (Wernli and Schwierz 2006; Smith and Mullen 1993; Case et al. 2004; Fowle and Roebber 2003; Done et al. 2004; Davis et al. 2006a,b, 2009; Ebert and McBride 2000). These methods are able to overcome the double penalty problem whilst also allowing for regional/sub-continental analysis. In this paper, we built upon their innovative work and adapted the object-based methods to dynamic topography. Using southern Africa as a case study, we demonstrated the ability of the object-based method to identify small regions on global maps, extract their properties and assess the similarities between a reference and perturbed twin. With the object-based method, one can compare regions based on the area they occupy (Chamberlain and Duquette, 2007), the total topography contained within them, their orientation and their average center of mass. We also went one step further and introduced a time component to our object-based method. As mentioned earlier (see Section 2), the timing of uplift and subsidence across various locations on Earth is strongly debated and southern Africa is an example (Gallagher and Brown 1999; Tinker et al. 2008). The usage of a time component in these metrics allows for the ranking of models based on our best estimate of the actual timing of an uplift or subsidence. However, as noted here, the knowledge on timing of dynamic topography is non-trivial.

A current limitation of our study lies in our choice of time penalty. We chose the time penalty as the time difference between the appearances of the uplift in the reference and perturbed twins respectively. While this is an analytical convenience, it is a harsh penalty as it does not take into account the existing geological knowledge of dynamic topography timing. Geologists typically consider time intervals and series rather than absolute times. A more geophysically meaningful penalty would classify the appearance of dynamic topography into time series so that if the timing of model-predicted dynamic topography falls within a

series that also contains the observed dynamic topography, such a model is not penalized. Inferences on the temporal evolution of dynamic topography are currently being gathered via studies of river profiles (Roberts and White, 2010), sediment compaction (Japsen, 2018) and provenance (Meinhold 2010; Şengör 2001), landform analysis (Guillocheau et al., 2018) based on planation surfaces (King, 1955), estimates of palaeoaltimetry (Kohn and Dettman, 2018), constraints from thermochronological data (Ehlers and Farley, 2003) or quantifications of sediment budgets at the scale of continental margins (Guillocheau et al. 2012; Said et al. 2015a,b). The availability of robust timing information for dynamic topography represents a key input in the usage of objct-based metrics.

6 CONCLUSION

Geodynamicists are now able to construct robust trajectories of mantle flow and a logical next step is the assessment of the constructed trajectories. By focusing on the surface manifestations of mantle flow, such as dynamic topography, it is possible to compare model-predicted geology with the real Earth observation. In doing so, spatial verification methods can play an important role. In this paper, using twin experiments, we explored two categories of spatial verification namely, gridpoint metrics and object-based metrics. We showed that the former provide first-order information about model performance globally. However, outside of purely synthetic experiments, our knowledge of dynamic topography is not perfect globally and some regions are better understood than others. Thus, such metrics are prone to providing inaccurate model insight. The object-based metrics, by their ability to focus on regions of interest, are able to circumvent this obstacle. We showed in this paper, that such methods can be combined with information on timing to create performance scores that rank models with respect to their similarity to a chosen reference. Meteorologists have long understood the importance of regional/limited-domain analysis and so, it is instructive to look into meteorological verification methods and adapt such tools to the study of dynamic topography.

7 ACKNOWLEDGMENTS

We acknowledge the support and funding provided to A. Taiwo by the Deutscher Akademischer Austausch Dienst (DAAD). Many thanks to Jincheng Ma for the Generic Mapping Tool (GMT) code with which the global dynamic topography maps were plotted. Thanks to George Craig (Meteorological Institute Munich) for his critical review of the results.

8 COLLABORATOR CONTRIBUTION

1. H.-P. Bunge supervised the research and corrected the manuscript
2. S. Ghelichkhan provided the dynamic topography maps used

References

Ahmed, N., Natarajan, T., and Rao, K. (1974). Discrete cosine transform. *IEEE Transactions on Computers*, C-23(1):90–93.

Anthes, R. A. (1983). Regional Models of the Atmosphere in Middle Latitudes. *Monthly Weather Review*, (6):1306–1335.

Bauer, S., Bunge, H.-P., Drzisga, D., Ghelichkhan, S., Huber, M., Kohl, N., Mohr, M., Rüde, U., Thönnes, D., and Wohlmuth, B. (2020). In *Software for Exascale Computing - SPPEXA 2016-2019*, Cham.

Bower, D. J., Gurnis, M., and Seton, M. (2013). Lower mantle structure from paleogeographically constrained dynamic earth models. *Geochemistry, Geophysics, Geosystems*, 14(1):44–63.

Braun, J. (2010). The many surface expressions of mantle dynamics. *Nature Geoscience*, 3(12):825–833.

Bunge, H. P. and Glasmacher, U. A. (2018). Models and observations of vertical motion (MoveOn) associated with rifting to passive margins: Preface. *Gondwana Research*, 53:1–8. Rifting to Passive Margins.

Bunge, H.-P., Hagelberg, C. R., and Travis, B. J. (2003). Mantle circulation models with variational data assimilation: inferring past mantle flow and structure from plate motion histories and seismic tomography. *Geophysical Journal International*, 152(2):280–301.

Bunge, H.-P., Richards, M. A., and Baumgardner, J. R. (2002). Mantle-circulation models with sequential data assimilation: Inferring present-day mantle structure from plate-motion histories. *Philosophical Transactions: Mathematical, Physical and Engineering Sciences*, 360(1800):2545–2567.

Burgess, P. M., Gurnis, M., and Moresi, L. (1997). Formation of sequences in the cratonic interior of North America by interaction between mantle, eustatic, and stratigraphic processes. *GSA Bulletin*, 109(12):1515–1535.

Burke, K. (1996). Africa's distinctive behavior over the past 30 million years.

Burke, K. and Gunnell, Y. (2008). The African Erosion Surface: A Continental-Scale Synthesis of Geomorphology, Tectonics, and Environmental Change over the Past 180 Million Years. In *The African Erosion Surface: A Continental-Scale Synthesis of Geomorphology, Tectonics, and Environmental Change over the Past 180 Million Years*. Geological Society of America.

Burstedde, C., Stadler, G., Alisic, L., Wilcox, L. C., Tan, E., Gurnis, M., and Ghattas, O. (2013). Large-scale adaptive mantle convection simulation. *Geophysical Journal International*, 192(3):889–906.

Carena, S., Bunge, H.-P., and Friedrich, A. M. (2019). Analysis of geological hiatus surfaces across Africa in the Cenozoic and implications for the timescales of convectively-maintained topography. *Canadian Journal of Earth Sciences*, 56(12):1333–1346.

Case, J. L., Manobianco, J., Lane, J. E., Immer, C. D., and Merceret, F. J. (2004). An objective technique for verifying sea breezes in high-resolution numerical weather prediction models.

Chamberlain, R. G. and Duquette, W. H. (2007). Some algorithms for polygons on a sphere.

Colli, L., Ghelichkhan, S., Bunge, H.-P., and Oeser, J. (2018). Retrodictions of Mid Paleogene mantle flow and dynamic topography in the Atlantic region from compressible high resolution adjoint mantle convection models: Sensitivity to deep mantle viscosity and tomographic input model. *Gondwana Research*, pages 252–272. Rifting to Passive Margins.

Copin, Y. (2012). Taylor diagram for python/matplotlib.

Davies, D. R., Valentine, A. P., Kramer, S. C., Rawlinson, N., Hoggard, M. J., Eakin, C. M., and Wilson, C. R. (2019). Earth's multi-scale topographic response to global mantle flow. *Nature Geoscience*, 12.

Davis, C., Brown, B., and Bullock, R. (2006a). Object-Based Verification of Precipitation Forecasts. Part I: Methodology and Application to Mesoscale Rain Areas. *Monthly Weather Review*, 134(7):1772.

Davis, C., Brown, B., and Bullock, R. (2006b). Object-Based Verification of Precipitation Forecasts. Part II: Application to Convective Rain Systems. *Monthly Weather Review*, 134(7):1785.

Davis, C. A., Brown, B. G., Bullock, R., and Halley-Gotway, J. (2009). The Method for Object-Based Diagnostic Evaluation (MODE) Applied to Numerical Forecasts from the 2005 NSSL/SPC Spring Program. *Weather and Forecasting*, 24(5):1252.

Denis, B., Côté, J., and Laprise, R. (2002). Spectral decomposition of two-dimensional atmospheric fields on limited-area domains using the discrete cosine transform (dct). *Monthly Weather Review*, 130(7):1812–1829.

Done, J., Davis, C., and Weisman, M. (2004). The next generation of nwp: Explicit forecasts of convection using weather research and forecast (wrf) model.

Ebert, E. E. and McBride, J. L. (2000). Verification of precipitation in weather systems: determination of systematic errors. *Journal of Hydrology*, 239(1):179–202.

Ehlers, T. A. and Farley, K. A. (2003). Apatite (U–Th)/He thermochronometry: methods and applications to problems in tectonic and surface processes. *Earth and Planetary Science Letters*, 206(1):1–14.

Errico, R. M. (1985). Spectra computed from a limited area grid. *Monthly Weather Review*, 113(9):1554–1562.

Flament, N., Gurnis, M., and Müller, R. D. (2013). A review of observations and models of dynamic topography. *Lithosphere*, 5(2):189–210.

Flament, N., Gurnis, M., Williams, S., Seton, M., Skogseid, J., Heine, C., and Müller, R. D. (2014). Topographic asymmetry of the south atlantic from global models of mantle flow and lithospheric stretching. *Earth and Planetary Science Letters*, 387:107–119.

Fowle, M. A. and Roebber, P. J. (2003). Short-range (0–48 h) numerical prediction of convective occurrence, mode, and location.

Freedman, D., Pisani, R., and Purves, R. (2007). Statistics (international student edition). *Pisani, R. Purves, 4th edn. WW Norton & Company, New York*.

French, S. W. and Romanowicz, B. A. (2014). Whole-mantle radially anisotropic shear velocity structure from spectral-element waveform tomography. *Geophysical Journal International*, 199(3):1303–1327.

Friedrich, A. M., Bunge, H.-P., Rieger, S. M., Colli, L., Ghelichkhan, S., and Nerlich, R. (2018). Stratigraphic framework for the plume mode of mantle convection and the analysis of interregional unconformities on geological maps. *Gondwana Research*, pages 159–188. Rifting to Passive Margins.

Gallagher, K. and Brown, R. (1999). Denudation and uplift at passive margins: the record on the Atlantic Margin of southern Africa. *Philosophical Transactions of the Royal Society of London Series A*, 357(1753):835.

Ghelichkhan, S., Bunge, H., and Oeser, J. (2021). Global mantle flow retrodictions for the early cenozoic using an adjoint method: evolving dynamic topographies, deep mantle structures, flow trajectories and sublithospheric stresses. *Geophysical Journal International*, 226(2):1432–1460.

Ghelichkhan, S. and Bunge, H.-P. (2016). The compressible adjoint equations in geodynamics: derivation and numerical assessment. *International Journal on Geomathematics (GEM)*.

Guillocheau, F., Rouby, D., Robin, C., Helm, C., Rolland, N., Le Carlier de Veslud, C., and Braun, J. (2012). Quantification and causes of the terrigeneous sediment budget at the scale of a continental margin: a new method applied to the Namibia–South Africa margin. *Basin Research*, 24(1):3–30.

Guillocheau, F., Simon, B., Baby, G., Bessin, P., Robin, C., and Dauteuil, O. (2018). Planation surfaces as a record of mantle dynamics: The case example of Africa. *Gondwana Research*, 53:82–98. Rifting to Passive Margins.

Hager, B. H., Clayton, R. W., Richards, M. A., Comer, R. P., and Dziewonski, A. M. (1985). Lower mantle heterogeneity, dynamic topography and the geoid. *Nature*, 313.

Hayek, J. N., Vilacís, B., Bunge, H.-P., Friedrich, A. M., Carena, S., and Vibe, Y. (2021). Correction: Continent-scale hiatus maps for the atlantic realm and australia since the upper jurassic and links to mantle flow-induced dynamic topography. *Proc. R. Soc. A*, 477(2251):20210437.

Hayek, N., Vilacis, B., Bunge, H.-P., Friedrich, A., Carena, S., and Vibe, Y. (2020). Continent-scale Hiatus Maps for the Atlantic Realm and Australia since the Upper Jurassic and links to mantle flow induced dynamic topography. *Proc. R. Soc. A*.

Heister, T., Dannberg, J., Gassmöller, R., and Bangerth, W. (2017). High accuracy mantle convection simulation through modern numerical methods – II: realistic models and problems. *Geophysical Journal International*, 210(2):833–851.

Hoggard, M. J., White, N., and Al-Attar, D. (2016). Global dynamic topography observations reveal limited influence of large-scale mantle flow. *Nature Geoscience*, 9.

Hoggard, M. J., Winterbourne, J., Czarnota, K., and White, N. (2017). Oceanic residual depth measurements, the plate cooling model, and global dynamic topography. *Journal of Geophysical*

Research: Solid Earth, 122(3):2328–2372.

Holdt, M. C., White, N. J., Stephenson, S. N., and Conway-Jones, B. W. (2022). Densely sampled global dynamic topographic observations and their significance. *Journal of Geophysical Research: Solid Earth*, 127(7):e2022JB024391. e2022JB024391 2022JB024391.

Horbach, A., Bunge, H.-P., and Oeser, J. (2014). The adjoint method in geodynamics: derivation from a general operator formulation and application to the initial condition problem in a high resolution mantle circulation model. *GEM - International Journal on Geomathematics*, 5(2):163–194.

Ismail-Zadeh, A., Schubert, G., Tsepelev, I., and Korotkii, A. (2004). Inverse problem of thermal convection: numerical approach and application to mantle plume restoration. *Physics of the Earth and Planetary Interiors*, 145(1):99–114.

Japsen, P. (2018). Sonic velocity of chalk, sandstone and marine shale controlled by effective stress: Velocity-depth anomalies as a proxy for vertical movements. *Gondwana Research*, 53:145–158. Rifting to Passive Margins.

King, L. C. (1955). Pediplanation and Isostasy: An Example from South Africa. *Quarterly Journal of the Geological Society*, 111(1-4):353–359.

Kohn, M. J. and Dettman, D. L. (2018). *5. Paleoaltimetry from Stable Isotope Compositions of Fossils*, pages 119–154. De Gruyter.

Kronbichler, M., Heister, T., and Bangerth, W. (2012). High accuracy mantle convection simulation through modern numerical methods. *Geophysical Journal International*, 191(1):12–29.

Lithgow-Bertelloni, C. and Silver, P. G. (1998). Dynamic topography, plate driving forces and the African superswell. *Nature*, 395:269–272.

Lorenz, E. N. (1965). A study of the predictability of a 28-variable atmospheric model. *Tellus*, 17(3):321–333.

Maple, C. (2003). Geometric design and space planning using the marching squares and marching cube algorithms. In *2003 International Conference on Geometric Modeling and Graphics, 2003. Proceedings*, pages 90–95.

Mass, C. F., Ovens, D., Westrick, K., and Colle, B. A. (2002). DOES INCREASING HORIZONTAL RESOLUTION PRODUCE MORE SKILLFUL FORECASTS?: The Results of Two Years of Real-Time Numerical Weather Prediction over the Pacific Northwest. *Bulletin of the American Meteorological Society*, 83(3):407–430.

McNamara, A. K. and Zhong, S. (2005). Degree-one mantle convection: Dependence on internal heating and temperature-dependent rheology. *Geophysical Research Letters*, 32(1).

Meinhold, G. (2010). Rutile and its applications in earth sciences. *Earth-Science Reviews*, 102(1):1–28.

Müller, R., Hassan, R., Gurnis, M., Flament, N., and Williams, S. (2018). Dynamic topography of passive continental margins and their hinterlands since the cretaceous. *Gondwana Research*, 53:225–251. Rifting to Passive Margins.

Oeser, J., Bunge, H.-P., and Mohr, M. (2006). Cluster Design in the Earth Sciences Tethys. In Gerndt, M. and Kranzlmüller, D., editors, *High Performance Computing and Communications*, pages 31–40, Berlin, Heidelberg. Springer Berlin Heidelberg.

Pekeris, C. L. (1935). Thermal Convection in the Interior of the Earth. *Geophysical Supplements to the Monthly Notices of the Royal Astronomical Society*, 3:343–367.

Price, M. G. and Davies, J. H. (2017). Profiling the robustness, efficiency and limits of the forward-adjoint method for 3-D mantle convection modelling. *Geophysical Journal International*, 212(2):1450–1462.

Ricard, Y., Richards, M., Lithgow-Bertelloni, C., and Le Stunff, Y. (1993). A geodynamic model of mantle density heterogeneity. *Journal of Geophysical Research: Solid Earth*, 98(B12):21895–21909.

Ritsema, J., A. Deuss, H. v. H., and Woodhouse, J. (2011). S40RTS: a degree-40 shear-velocity model for the mantle from new Rayleigh wave dispersion, teleseismic traveltime and normal-mode splitting function measurements. *Geophysical Journal International*, 184:1223–1236.

Roberts, G. G. and White, N. (2010). Estimating uplift rate histories from river profiles using African examples. *Journal of Geophysical Research: Solid Earth*, 115(B2).

Said, A., Moder, C., Clark, S., and Abdelmalak, M. M. (2015a). Sedimentary budgets of the Tanzania coastal basin and implications for uplift history of the East African rift system. *Journal of African Earth Sciences*, 111:288–295.

Said, A., Moder, C., Clark, S., and Ghorbal, B. (2015b). Cretaceous–Cenozoic sedimentary budgets of the Southern Mozambique Basin: Implications for uplift history of the South African Plateau. *Journal of African Earth Sciences*, 109:1–10.

Schaeffer, A. J. and Lebedev, S. (2013). Global shear speed structure of the upper mantle and transition zone. *Geophysical Journal International*, 194(1):417–449.

Şengör, A. M. C. (2001). Elevation as indicator of mantle-plume activity. In *Mantle plumes: their identification through time*. Geological Society of America.

Simmons, N., Forte, A., and Grand, S. (2007). Thermochemical structure and dynamics of the african superplume. *Geophys. Res. Lett*, 34(2).

Simmons, N. A., Myers, S. C., Johannesson, G., Matzel, E., and Grand, S. P. (2015). Evidence for long-lived subduction of an ancient tectonic plate beneath the southern indian ocean. *Geophysical Research Letters*, 42(21):9270–9278.

Smith, B. B. and Mullen, S. L. (1993). An evaluation of sea level cyclone forecasts produced by nmc's nested-grid model and global spectral model.

Stacey, F. D. (1992). *Physics of the Earth.*

Surcel, M., Zawadzki, I., and Yau, M. K. (2015). A Study on the Scale Dependence of the Predictability of Precipitation Patterns. *Journal of the Atmospheric Sciences*, 72(1):216–235.

Taylor, K. E. (2001). Summarizing multiple aspects of model performance in a single diagram. *Journal of Geophysical Research: Atmospheres*, 106(D7):7183–7192.

Tinker, J., de Wit, M., and Brown, R. (2008). Mesozoic exhumation of the southern cape, south africa, quantified using apatite fission track thermochronology. *Tectonophysics*, 455(1):77–93.

Valentine, A. P. and Davies, D. R. (2020). Global Models From Sparse Data: A Robust Estimate of Earth's Residual Topography Spectrum. *Geochemistry, Geophysics, Geosystems*, 21(8):e2020GC009240. e2020GC009240 10.1029/2020GC009240.

van der Walt, S., Schönberger, J. L., Nunez-Iglesias, J., Boulogne, F., Warner, J. D., Yager, N., Gouillart, E., Yu, T., and the scikit-image contributors (2014). scikit-image: image processing in Python. *PeerJ*, 2:e453.

Vibe, Y., Friedrich, A., Bunge, H.-P., and Clark, S. (2018). Correlations of oceanic spreading rates and hiatus surface area in the North Atlantic realm. *Lithosphere*, 10(5):677–684.

Wernli, H. and Schwierz, C. (2006). Surface Cyclones in the ERA-40 Dataset (1958 2001). Part I: Novel Identification Method and Global Climatology. *Journal of Atmospheric Sciences*, 63(10):2486–2507.

Wieczorek, M. A. and Meschede, M. (2018). SHTools: Tools for Working with Spherical Harmonics. *Geochemistry, Geophysics, Geosystems*, 19(8):2574–2592.

Zhong, S., Yuen, D., Moresi, L., and Knepley, M. (2015). *Numerical Methods for Mantle Convection*, volume 7, pages 197–222. Elsevier Inc.

Chapter 5

Outlook

It is now clear that by assimilating estimates pertaining to the surface velocity field into a mantle model, robust, reliable and accurate trajectories of mantle flow can be constructed, despite the butterfly effect. On the other hand, it has long been thought difficult to observe mantle convection, because the flow is concealed by the overlying plates. However, two key surface manifestations of mantle convection are becoming better known. One is the horizontal surface velocity field, which is represented in the form of past plate motion models. The other is the dynamic topography field, which is a representation of convectively-maintained radial stresses in the mantle. Over the last years, global past plate motion models have been constructed for a time period of 100-200 million years. These models have now reached a high level of sophistication. At the same time, innovative techniques like hiatus mapping are bringing dynamic topography variations into focus. Through such techniques, the dynamic topography field of Earth has now been mapped for a time period of 100 million years. The fact that the horizontal and vertical surface velocity field of the Earth surface is now known over this timeframe implies that a threshold has been crossed. It means that key observational constraints exist for the mantle convection system over a time period of about one transit time. Translated into meteorology, this timescale corresponds to a few days of weather evolution, referred to in meteorology as transport times, as mentioned in the introduction of this thesis. Given these developments in observational geodynamics, we are fast approaching the plateau that meteorology comfortably sits on. The latter is a discipline that combines sophisticated models with abundant data. In this regard, geodynamicists can learn from meteorologists, how best to exploit these observational constraints in the context of computational models of the Earth. Meteorologists have also developed innovative methods for comparing model output with observations. Such methods include spectral comparisons on global and regional scales, gridpoint analysis such as the Taylor diagram and power ratio and object-based methods. The latter compare specific regions of model output against their counterparts in the observations. By focusing on local regions, this allows one to assess model performance in a highly succinct manner, without interference from other scales. In my thesis, I have shown that the horizontal velocity field, i.e. past plate motion models, must be used as an input to assure robust mantle flow trajectories. But my thesis suggests that key regions should be identified in the global

dynamic topography field to test model trajectories of past mantle flow. Potential target regions could include the late Mesozoic southern African uplift, as shown in this thesis, the late Cretaceous disappearance of the Western Interior Seaway, early Cenozoic uplift of western Australia and the Miocene subsidence of southeast Asia. For these regions, the model assessment methods that I have developed would be particularly useful.

Danksagung

While finishing up this thesis, I cast my mind back to 2015 when I moved to Munich as a student in the geophysics masters program at LMU Munich. Since that time, the amount of personal and professional growth that I have undergone is unbelievable. I want to express deep gratitude to my supervisor, Prof. Dr. Hans-Peter Bunge. Peter's creativity and work ethic are a source of inspiration for me. After I took the masters course on Solid Earth Physics, Peter encouraged me to pursue research in Geodynamics and I must say that I do not regret this decision. Also, his support during a very tough phase of my PhD contributed to my being able to produce this work. I would also like to offer thanks to my co-supervisor, Prof. Dr. George Craig at the Meteorological Institute of LMU Munich. My first contact with George was in January 2020 when I was exploring ways with which to compare my twin experiments. I sent George a rather haphazard, unstructured e-mail and despite his busy schedule, he read through this very rough e-mail and made time to meet with me. What started as a brief discussion with George ended up over one year later in my development and application of object-based metrics to dynamic topography. Finally, I would like to thank Prof. Dr. Stuart Gilder, who has served as an unofficial mentor to me since I arrived in 2015. Stuart is always happy to chat at length with me and offer me advice along the corridors of the Geophysics department. Before moving on from this point, I must mention that my coming to Germany in 2015 was facilitated and made easy due to the support of Elisabeth and Sebastian Weckel as well as Wolfgang Machur. The Weckels picked me, a complete stranger, up from the airport and housed me in their son's apartment for one month. Wolfgang was kind enough to pay my rent for this time period. Even after this time, Wolfgang and the Weckels always kept in touch and supported me. Sadly, Sebastian passed away at the beginning of 2021. My completion of this PhD work is also to honour his memory.

Even though a PhD is based on independent research, I am grateful to have had supportive colleagues throughout my journey. Dr. Lorenzo Colli has been influential in my achievements right from my masters degree until now. I would go to his office severally to ask for advice on Geodynamics and life in general and he was always ready to offer his help. Even during this PhD, he has always been one WhatsApp message away. Dr. Ingo Stotz also deserves thanks at this point. Ingo offered me much encouragement during a phase in my PhD where I made only little progress. His reassurance that this phase was normal in virtually any PhD helped me renew my confidence and made me forge ahead.

Jincheng Ma, my office mate has also been very kind. I have lost count of how many times I've asked Cheng to help me assess the quality of my figures. His input and help with the Generic Mapping Tools software led to the creation of some high-quality figures for this thesis. Beyond this, I very much enjoy chatting and interacting with Cheng. I would also like to thank the other members of the Geodynamics group including Dr. Bernhard Schuberth, who contributed a great deal to my first paper and also praised me all the times I did good science. Thanks to Isabelle, Roman, Berta, Nicolas, Josef, Dr. Yi-Wei Chen, Dr. Marcus Mohr, Dr. Jens Oeser and the other members of the Geodynamics group. Thanks to Dr. Mandana Parsi, my friend since the masters degree, for her continual willingness to help with questions regarding submission of my thesis and our long talks about the challenges of being a foreigner in Germany. Finally, I would like to thank the Deutscher Akademischer Austausch Dienst (DAAD) for funding my PhD over a period of 5 years.

One needs balance in order to lead a good life. Outside the university, my contacts at the Mariposa Boxing Club, especially Dr. Tim Yilmaz and Kai Melder have been very supportive. Tim has always encouraged me to stay focused on my PhD while also taking out time to box. Both Tim and Kai ensured that I participated in the Allgemeine Deutsche Hochschule Boxen Trophy 2019, which I won. Mark Darrington has also been a regular sparring partner and I do not take our sparring sessions at the Isar for granted. Mr. Pricky has always encouraged me to keep fit and protect my mental health. In the last one year, I have had the pleasure of sharing a flat with wonderful flatmates who make it easy to come back home after work. To Aline, Valerie, David and Betsy, I say thank you. Also, in the last one year, I have made lots of contacts at the Eiscafe Italia in Roecklplatz and the Nigerian restaurants at Maistrasse and Tumblingerstrasse. Thanks to Ntanta, Ogidiga, Abimbola, Robin, Epa, Don Brown, Bright Fresh, Victor, Abolo, Ifeoluwa, Achala, Americanah, Omoloba, Mr. Johnson Adams, Abiodun Adeyemi, Remi Biola, Joachim, Malika, Elio, Tomasso, Klaus Jacobi, Klaus Teichert, Roland, Pascal, Loni, Ilse, Aye, Ruppi, Heio, Hazel and others.

Much closer to me are my friends and family from back home. During difficult phases in my personal life, I have had the pleasure of leaning on Abisola Mon-Amie, Aderola (the Ibadan girl), Benedict, Glory, Tinuola Asha, Dr Olatunji Gege, Naa, Elenchi, Benjy, Aliu, Bolutife Ogunsola (Mr Quantdev) amongst others. Finally, I want to thank my siblings and parents. Atinuke has always stood strong by my side and is ready to offer me any form of support that I require. Akorede, despite being only a teenager, has proven to be highly emotionally intelligent. She offers me advice and words of encouragement and even though she may not realise it, her words are a motivation for me. Aunty Halima has been a support for me since I was a young boy and she is still present in my life today. Though she is not a scientist, her presence in my life has led to the completion of this PhD. I also appreciate uncle Jamal, who has supported me since I was a young boy. I cannot forget his kind gesture of buying me my first flight ticket to Germany in 2015. Many thanks to my uncle, Mr. Jide Jose and his wife, Mrs. Kudi Jose. They show me so much love and they played a huge role in my coming to Germany. My mother, Temitayo Taiwo (Mame) and

father, Adedimeji Taiwo (Mr Gold) deserve the biggest thanks of all. Since my childhood, I have observed keenly how they continuously sacrifice their resources to provide me and my siblings with a high-quality education, despite the huge difficulty involved in doing so. Mame and Mr Gold, I cannot thank you enough. My completion of this PhD is in no small part due to your presence and support in my life. It is to you both that I dedicate this work.